Exploring Charge Storage Mechanism in MXene as Supercapacitor Electrode: A First-Principles Approach

Mandira Das

Roll No. : 186121013

under the supervison of

Prof. Subhradip Ghosh

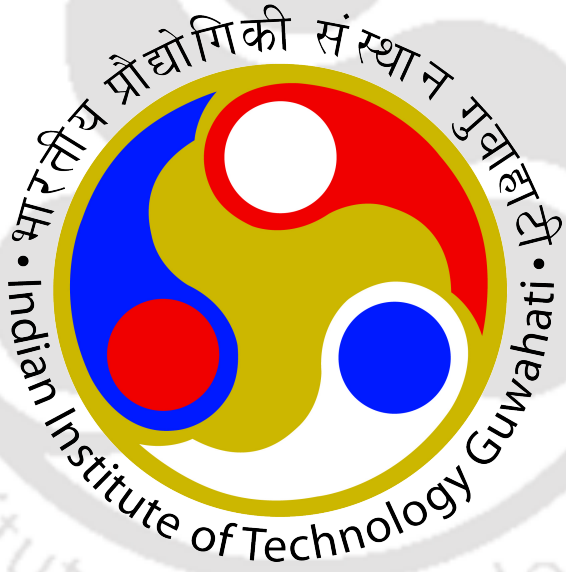

Department of Physics
Indian Institute of Technology Guwahati
Guwahati-781039, Assam, India

November, 2023

Exploring Charge Storage Mechanism in MXene as Supercapacitor Electrode: A First-Principles Approach

A thesis submitted by

Mandira Das

to

Depratment of Physics
Indian Institute of Technology Guwahati
in partial fulfillment of the requirements
for the award of the degree of
Doctor of Philosophy in Physics

Department of Physics
Indian Institute of Technology Guwahati
Guwahati-781039, Assam, India

Statement

The work contained in the thesis entitled **"Exploring Charge Storage Mechanism in MXene as Supercapacitor Electrode: A First-Principles Approach"** has been carried out at the Department of Physics, Indian Institute of Technology Guwahati, India by me under the supervison of Prof. Subhradip Ghosh. The material of this thesis has not been submitted elsewhere for any other degree. Works presented in this thesis are all my own unless referenced to the contrary in the text.

(Mandira Das)
Department of Physics
Indian Institute of Technology Guwahati
Guwahati-781039, Assam, India

Date:

Disclaimer

The bibliography included in this thesis is, by no means complete but contains the ones which are consulted thoroughly by me. I apologize for inadvertently missing out some of the research papers, review articles and other scientific documents pertaining to the focus of this thesis which should also have been cited. For illustration purpose some of the figures in this thesis are taken from other sources and properly cited.

Certificate

It is certified that the work contained in the thesis entitled **"Exploring Charge Storage Mechanism in MXene as Supercapacitor Electrode: A First-Principles Approach"** by Mandira Das, a Ph.D. student of the Department of Physics, Indian Institute of Technology Guwahati is carried out under my supervision and has not been submitted elsewhere for the award of any other degree.

(Prof. Subhradip Ghosh)
Department of Physics
Indian Institute of Technology Guwahati
Guwahati-781039, Assam, India

Date:

Dedicated to my parents

Acknowledgements

I thank my supervisor, Prof. Subhradip Ghosh, for his guidance during my Ph.D. tenure. His continuous support helped me keep my motivation during the tough times I have faced during my Ph.D. I am thankful to him for keeping faith in me and allowing me to work in a field that is new to him.
I want to thank Prof. Biplab Sanyal, one of my collaborators from Uppsala University, for mentoring me. I am grateful to him for hosting my visit to Uppsala University. I thank Prof. Pravat Kumar Giri and Dr. Uday Narayan Maiti from IIT Guwahati for choosing me as one of their theoretical collaborators. A special thanks to Dr. Uday Narayan Maiti for his advice from the experimental point of view, which helped me prepare my thesis flow.
I want to acknowledge my doctoral committee members - Dr. Uday Narayan Maiti, Prof. Girish Setlur, and Prof. Mohd. Qureshi for their valuable advice during my annual assessment. I thank our former HoD Prof. Subhradip Ghosh and present HoD Prof. Perumal Alagarsamy. I especially thank Basab-da for his assistance with any cluster-related issues. I am thankful to Param Ishan, IIT Guwahati, for the supercomputer facility. I thank the Department of Physics IIT Guwahati, India, for allowing me to utilize the Newton cluster, funded under the FIST program by DST, India. I acknowledge SERB, India for hosting my conference visit to Germany.
I thank Dr. Saugata Bhattacharya from Vidyasagar College for motivating me to choose a career in Physics. I express my respect to Prof. Jayanta Kumar Bhattacharjee for mentoring me during my M.Sc. days.
I sincerely thank the seniors, Biswanath Da, Souvik Da, Ashis Da, and Sheuly. A warm thanks to Sayandeep Da for his advice from time to time. My best wishes to my juniors Himangshu, Himanshu, Madhumita, Swati, and Arvind for their future, and thanks for creating some memorable moments. My special thanks to Murari for collaborating with me on one of my thesis papers.
I especially acknowledge Google for answering all my queries.
My best wishes and thanks to the whole 2018 Ph.D. Physics batch of IIT guwahati. I am lucky to have friends like Angana, Debu, Raju, Monu, Prantik, Sudeshna, and Bhargabi at IIT Guwahati. I thank Riajul, Rajesh Da, Swarup, Surojit, Sayan Da, Subhajit Da, and Shilpi for creating a friendly environment for me.
Finally, I would like to express my gratitude and respect to my parents for their unconditional love and support.
Ultimately, I cheered up myself for the continuous hard work I put through my Ph.D. days.

Abstract

The exfoliation of layered transition metal carbides/nitrides, **MXenes** ($M_{n+1}X_n$), from its 3D precursor MAX is a remarkable event in the history of 2D materials. MXenes caught attention due to their applications in versatile fields, such as electromagnetic shielding, energy storage, H_2 storage, energy conversion, sensors, and memristors, to name a few. Ti_3C_2, the first discovered MXene, caught everyone′s attention due to its excellent charge storage capacity as a supercapacitor electrode. It has been the most explored MXene in this 2D subfamily. 70% of the MXene research is on this compound only. Baring Ti_3C_2, various other transition metal-based MXenes have been synthesized to date. This 2D subfamily exhibits diversity in structure and composition. MXene is enormously famous due to its performance as an energy storage device. The high electrical conductivity, hydrophilicity, surface redox activity, and mechanical stiffness make it a potential alternative to Graphene as an electrode in energy storage devices like batteries and supercapacitors. Experimental evidence suggests that diversity in structure, composition, and surface passivations affect the supercapacitive property of MXenes. However, there are a few scattered attempts to explore these aspects for varieties of systems to understand the mechanisms of charge storage in MXene-based supercapacitors. This thesis provides a systematic study on understanding structural and compositional effects on the electrochemical performances of MXene-based supercapacitors.
Our investigations start with exploring the capacities of M_2C and M_3C_2 MXenes as supercapacitor electrodes. We consciously choose various 3d and 4d transition metals as M elements. We show the significance of quantum capacitance on energy storage performance. We also explain the effect of surface passivation on MXene capacitances. Further, we provide a comparative study of substitution and doping in enhancing the storage capacity of MXenes. An explanation of the influence of doping sites on the redox capacitance of Ti_3C_2 is given. Next, we attempt the route of surface engineering to improve the energy storage capacities of MXenes. To this end, we construct Jnus $MM'C$ MXene and study their electrochemical performances. In the course of this study, we find that much superior capacities are obtained if one of the components of Janus is a magnetic element. We extend the study by considering solid solutions of one of these systems and investigating the effect of chemical and magnetic disorders on its supercapacitive performance.
In a nutshell, this thesis systematically explores the structure-property relationships about electrochemical performances of various MXenes that can yield substantial insights into the physics and chemistry of this family of 2D compounds.

Contents

List of Figures

Chapter 1

Introduction

1.1 Energy Storage Devices and the rise of Supercapacitors

Energy consumption continues to rise with technological advancement, changes in mobility, and globalization. Sophisticated power grids have been developed to ensure the smooth transference of energy on the requirement. The current energy consumption has come at the price of the diminution of fossil fuels and the upsurge of Greenhouse gases in the environment. The depletion of fossil fuels and the Greenhouse effect has become a global threat to humankind. Researchers from all over the world are working hard to face such significant challenges against any odds. Solar energy, wind energy, tidal energy, etc., are some renewable energy sources that are environment friendly. Naturally, significant attention is diverted in tapping such sources. Devices are the necessary components for effective usages of the huge energy reserve that the nature offers.
Energy devices can be categorized as energy conversion devices and energy storage devices. Energy conversion devices collect and convert the energy in the environment into easy-to-use electrical energy. Solar panels, photovoltaic cells, tribo/piezoelectric nanogenerators, thermoelectric devices, water-induced power generators, etc., are energy conversion devices that convert solar, mechanical, thermal, and potential energy into electricity. The nature-dependent energy sources have the characteristics of discontinuity, liability, and uncontrollability. The power generator based on renewable energy sources produces small, unstable, and discontinuous energy supplies. The energy storage device is an essential solution to this problem, storing the harvested energy and supplying the same upon demand. Energy conversion and storage devices are solutions to the problem of sustainable energy supply from renewable sources. Energy storage device mainly includes secondary ion batteries and supercapacitors. The basic construction of the battery and supercapacitor is the same but varies in working principle as well as in performance parameters like energy density, power density, life cycle, and stability.

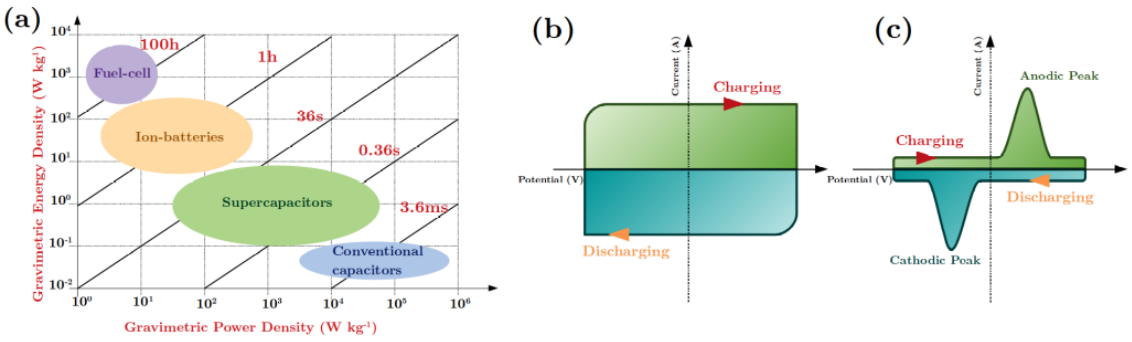

Figure 1.1: (a) A Ragone plot, showing the energy and power density of energy storage devices. Schematic current-potential(I-V) curves of (b) a Supercapacitor, and (c) a Battery are shown.

Figure 1.1(a) is a Ragone plot (energy density vs. power density plot) of various energy storage devices. The Ragone plot establishes supercapacitor as a bridge between conventional capacitors and batteries. A supercapacitor has higher energy density than a capacitor and higher power density than a battery. The fundamental difference between a supercapacitor and a battery is the

charging mechanism. Figure 1.1(b) shows the I-V characteristic curve of supercapacitors. It offers a constant current-potential relationship during charging/discharging. However, a battery shows redox peaks (anodic and cathodic peaks) in the I-V curve during operation, as shown in Figure 1.1(c). The charging/discharging mechanism happens at the surface of the electrode for a supercapacitor, whereas, for a battery, an intercalation of ions occurs at the electrode. Supercapacitors and batteries have some specific field of application. The battery is suitable where one needs constant energy output for a long time., like a mobile phone, inverter, etc. However, supercapacitor plays a key role when colossal energy output is required in a shorter time, such as electric car, port system, elevator, etc.
Research and commercialization on supercapacitors started in the 1970s and 1980s in the United States, Japan, Russia, Switzerland, South Korea, etc. United States′ Maxwell, Japan′s NEC, Panasonic, Tokin, and Russian Econd are some leading companies to occupy the global market. According to Bosch′s Research report (2007-2022), the global supercapacitor market has reached a value of 16×10^{10} US dollars in 2015, and it could exceed 92.3×10^{9} US dollars by 2020. These statistics speak about this storage device′s rising popularity in technology market. Supercapacitors have evolved from energy storage devices to large-scale power sources with unique advantages. Helmholtz′s proposed idea of double-layer capacitance in 1857 provides the basis of this storage device. Bcker first proposed the idea of a smaller capacitor as an energy storage device with a specific energy density close to batteries in 1957. The commercialization of supercapacitors started in 1968 when Standard Oil Company Sohio first proposed a patent for making double-layer using carbon materials with a high specific area. In 1979, Japan′s NEC first produced a supercapacitor as the starting system of electric vehicles. The industrialization of supercapacitors started in the 1980s with NEC, Panasonic, and Mitsubishi products. In the 1990s, Econd and ELIT joined the race of supercapacitor commercialization. In the next section, storage mechanism in a supercapacitor is briefly described.

1.1.1 Storage mechanism in a Supercapacitor

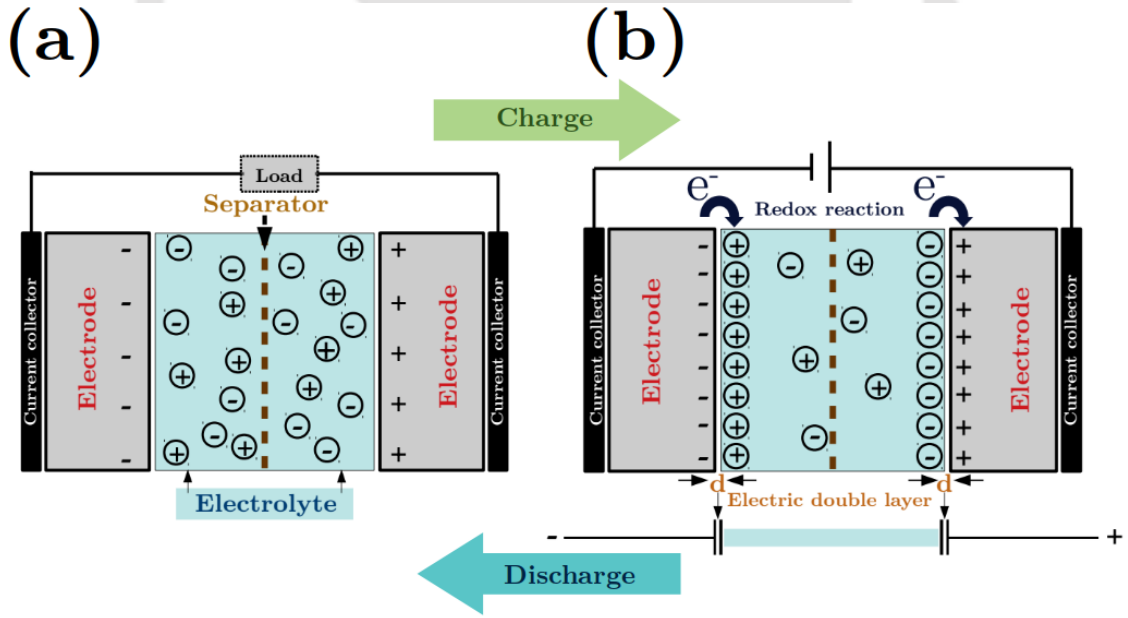

Figure 1.2: Different componenets of supercapacitor. (a)the discharged and (b) the charged condition.

A supercapacitor is an efficient electrochemical energy storage device. It uses polarised electrolytes to store energy. Figure 1.2 shows the schematic of a supercapacitor. It consists of two electrodes, an electrolyte sandwiched between them, and a separator to avoid short circuits. Two types of charging mechanisms occur at the electrode/electrolyte surface of the supercapacitor. On application of an external voltage, the anions and cations of the electrolyte move towards the positive and negative electrodes, respectively, as shown in Figure 1.2(a). The electrolyte ions accumulate over the electrode surface due to electrostatic force between opposite charges and form

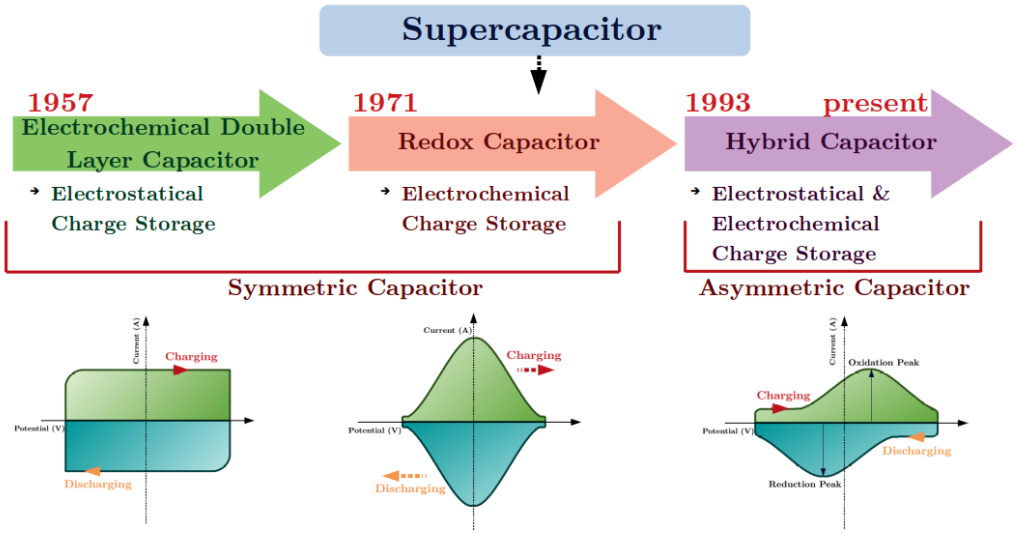

Figure 1.3: Types of Supercapacitor, along with the timeline of it's development. The schematics of current-voltage(I-V) characteristics are shown.

a layer of ions. The charged electrodes and the accumulated ions act like two charged plates of a conventional capacitor; the electrolyte acting like the dielectric. This charging mechanism is known as the Electrochemical Double Layer (EDL) mechanism. The storage capacity of the EDL mechanism depends on the distance ('d', as shown in Figure 1.2(b)), area of the electrode, 'A' and the dielectric constant of the electrolyte. Two conventional capacitor-like double layers form at the two electrode surfaces of the supercapacitor device (the circuit like structure of Figure 1.2(b)), and they combine in series to give the total capacitance of the device. Apart from this, when the electrode material contains redox-active elements, charge transfer occurs across the double layer between electrode and electrolyte ions (Figure 1.2(b)). This charging mechanism is known as the Redox mechanism. The supercapacitor discharges on connecting it with a load, and the ions detach from the electrode surface (Figure 1.2(a)). Supercapacitors are classified into three categories depending on the charging mechanism, (Figure 1.3): (a)Electrochemical Doule Layer Capacitor (EDLC), (b) Redox Capacitor, (c)Hybrid Capacitor. The charging mechanism of a supercapacitor depends on the electrode materials used in the device. In EDLC, the electrostatic force between the opposite charges is responsible for the charging/discharging, whereas reversible faradaic redox reaction is responsible for Redox Capacitor. The hybrid capacitor shows both the EDL and Redox mechanism. A schematic of I-V characteristics for all the capacitors is shown in Figure 1.3. The I-V curve is rectangular for EDLC. The Gaussian-like I-V curve is the signature of the oxidation and reduction reaction at the electrode/electrolyte interface of the redox capacitor. The hybrid capacitor shows a rectangular current-voltage relationship throughout the voltage range and oxidation/reduction peaks at particular voltages. The storage capacity of a supercapacitor depends majorly on the electrode materials and the type of electrolytes. In the next section we provide information on this.

1.2 Electrode Materials

The electrode material of a supercapacitor has a significant role in determining the charge storage performance. The electrode materials must have some key features, such as high electrical conductivity, high specific surface area, thermal stability, chemical stability, corrosion resistance, economical, and most importantly, environment friendly. Besides this, the morphology of the electrode materials is also essential. The pore size, pore size distribution, pore shape, and availability of redox-active sites to the electrolyte affect the electrochemical performance of the device. The pore size of an electrode material inversely affects the capacitance but directly affects the power density of the material. The selection of electrode material becomes specific to the applications.

In 1975, Bcker used carbon-based material as an electrode for supercapacitors[1]. High conductivity, thermal stability, chemical stability in various electrolytes, and symmetric galvanostatic charge-discharge profile make carbon materials a promising electrodes for supercapacitors. Later, activated carbons(AC)[2], carbon nanotubes (CNT)[3], carbon fibers[4], carbon aerogels[5] emerge as potential electrodes for supercapacitors. Metal oxide-based electrode materials are also developed in the meantime as they provide redox active sites, which enhances the storage capacity as well as the power density of the device. RuO_2[6], NiO[7], MnO_2[6], are some examples of such materials.
The storage capacity of supercapacitors achieved a new high with the discovery of the first two-dimensional material, graphene, in 2004[8]. It is established experimentally and mathematically that a material with a higher specific area can provide higher energy density. The high specific area of two-dimensional material offers an extensive platform for electrolyte transport and enhances the storage capacity. Graphene has some unique structural and electronic features, namely:

- The large surface provides a comprehensive platform for electrolyte transport.
- High electrical conductivity offers low diffusion resistance, enhancing power and energy density.
- Superior tensile strength.

Graphene provides all the features to be used in flexible, high-performance supercapacitors. The processing of graphene thin film limits due to restacking of the graphene sheets resulting from π-π interaction and Van-Der Waal forces. This reduces the surface areas and limits electrolyte ions' diffusion through the graphene layers. Researchers attempted to overcome this bottleneck by adding spacers, template-assisted growth, and crumpling of the graphene sheet[9]. Researchers have developed graphene composites, heterostructure of graphene with other materials, graphene oxides, reduced graphene oxides, and foreign element doping to get an excellent combination of energy and power density. Two-dimensional transition metals dichalcogenides(TMDs) and h-BN are also on the list of promising electrodes for supercapacitors.
Graphene was the famous energy storage electrode until the discovery of Ti_3C_2 in 2011[10]. The successful exfoliation of Ti_3C_2 from layered 3D precursor Ti_3AlC_2 set a new benchmark in energy storage research. Ti_3C_2 belongs to the two-dimensional family known as **MXene**. MXene with chemical formula $M_{n+1}X_n$ (M: transition element; X: C or N) is represented as $M_{n+1}X_nT_x$, where T denotes functional groups (-F, -O, -OH) that passivate the MXene surfaces during the synthesis process. After discovery, $Ti_3C_2T_x$ have been widely explored as energy storage material to date. Gogotsi and co-workers demonstrated electrochemical intercalation of several cations(Na^+, K^+, Mg^{2+}, NH_4^+, Al^{3+}) through Ti_3C_2 with a high capacitance of 300 Fcm^{-3}[11]. Unlike Graphene, $Ti_3C_2T_x$ shows a pseudocapacitive storage mechanism depending upon the electrolytes used. The terminal -O groups provide the platform of bonding/debonding to the hydronium ion of H_2SO_4 during the charging/discharging, enhancing the redox counterpart[12]. In the next section, we discuss MXene elaborately, focusing on its electrochemical energy storage performance.

1.3 MXene

MXene is a two-dimensional derivative of the 3D precursor MAX phase. MAX phases are a class of hexagonal ternary carbide or nitride (X) of a transition metal (M) and group 13-15 elements (A)[13]. It has a general formula $M_{n+1}AX_n$ (space group $P6_3/mmc$), where n=1, 2 and 3. Figure 1.4 shows the hexagonal unit cell of 211, 312, 413 MAX phases. The unit cell consists of M_6X octahedra, interleaved with the layers of A element. The difference between the three structures, as seen from Figure 1.4, is in the number of M layers separating the A layers. The MX layers are twinned to each other and separated by the A layers, which act as a mirror plane. They show the combined characteristics of metals and ceramics[14]. For example, they conduct heat and electricity like metals and are elastically stiff, strong, brittle, and heat tolerant like ceramics. MAX phases are termed 'thermodynamically stable nanolaminates'[13] to distinguish them from artificial nanolaminates. A 'nano laminate' is a material with a laminated-layered structure in which the thickness of the individual layers is in the nanometer range. The more stringent description of 'thermodynamically stable nanolaminates' refers to the MAX phases as 'inherently nano laminate' (*i.e.*, nanolaminate by nature, not by artificial design). They are called 'layered ternary

ceramics,'[13] as they contain exactly three elements and have a layered structure.

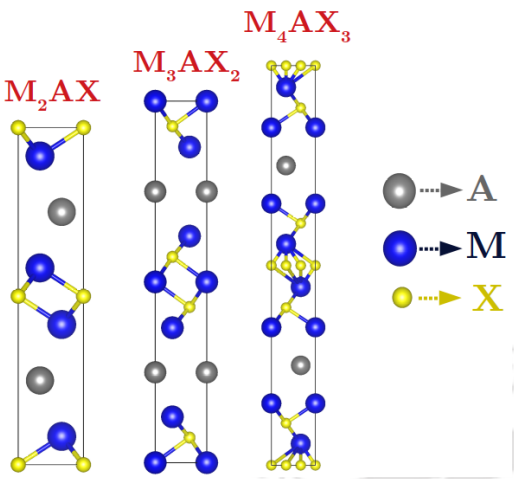

Figure 1.4: Unit cells of $M_{n+1}AX_n$, n=1,2,3. Grey, Blue and Yellow balls represent the A, M and X atoms, respectively.

The $M_{n+1}X_n$ layers are chemically stable compared to the 'A' layers, which are relatively weakly bounded and most reactive specie. Researchers have tried many experimental techniques to remove the 'A' element from the MAX phase without deforming the MX layers. For example, on heating Ti_3SiC_2 in a C-rich atmosphere, the Si atoms escape, leaving behind TiC_x as the end product[15]. When the same experiment is carried out by placing Ti_3SiC_2 in molten cryolite[16] or molten Al[17], $TiC_{0.67}$ forms in a partially ordered cubic phase. In 2011, Yury Gogotsi and co-workers reported a chemical route to etch out the 'A' layer without deforming the 'MX' layers[10]. The exfoliated 'MX' layers are called **'MXene'**. The nomenclature **'MXene'** comes from metal (**M**) and carbon and/or nitrogen (**X**) along with **ene** from the family of 2D materials like graphene, silicene, germanene, etc. The following subsections discuss MXenes substantially, which includes the synthesis process, members of the MXene family, and its various applications.

1.3.1 Synthesis

In 2011, Yury Gogotsi and his team first reported the successful synthesis of Ti_3C_2 MXene from its 3D MAX precursor Ti_3AlC_2[10]. The synthesis of MXene is a two-step process; first is the chemical etching of the 'Al' layer, and the second is the exfoliation of MX layers. Figure 1.5 shows the schematic of the synthesis process. According to the experiment, the 'Al' layers are etched out from the Ti_3AlC_2 by treating it with Hydrofluoric Acid (HF); this process is called etching (step-1 of Figure 1.5). During the etching process, some functional groups get attached to the surfaces of the MX layers. The functional groups are -F, -O, -OH. The chemical reactions involved in the process are given in equations (1.1) - (1.3). The equation (1.1) is the essential 'Al' removal step. The surface functionalizations happen through the reactions given in equations (1.2)-(1.3).

$$Ti_3AlC_2 + 3HF = AlF_3 + \frac{3}{2}H_2O + Ti_3C_2 \tag{1.1}$$

$$Ti_3C_2 + 2H_2O = Ti_3C_2(OH)_2 + H_2 \tag{1.2}$$

$$Ti_3C_2 + 2HF = Ti_3C_2F_2 + H_2 \tag{1.3}$$

It is not possible to synthesize pristine MXenes. The MXene surfaces always gets passivated by some functional groups (-F, -O, -OH), which led to synthesis of functionalized MXenes[10]. Several groups have used etchant to remove the 'Al' layers form MAX. One of the established process is *in situ* formation of HF by direct reaction of hydrochloric acid (HCl) with Lithium Fluoride (LiF) solution, to exfoliate MXene from MAX[18]. The different available etching agents are given in the Table 1.1. After selective etching of A elements from MAX phase using etching agents, the

Table 1.1: Different etchants used to exfoliate MXene from MAX

Methods	Etchant	Temperature(°C)	Ref
with HF	HF	27-55	Adv. Mat.,23(37), 4248, 2011
	H_2O_2 + HF	40	Ange. Chemie Int. Edi., 57(19), 5444, 2018
in situ HF	HCl+LiF	35-55	Nature, 516, 7529, 2014
	HCl+ (Na,K or NH_4F)	30-60	Appl. Sur. Sci., 416, 781, 2017
using molten salt	LiF+NaF+KF	550	Nanoscale, 8(22), 11385, 2016
hydrothermal	NaOH	270	Ange. Chemie Int. Edi., 57(21), 6115, 2018
	$NaBF_4$, HCl	180	Ceramics Int., 44(15), 18886, 2018

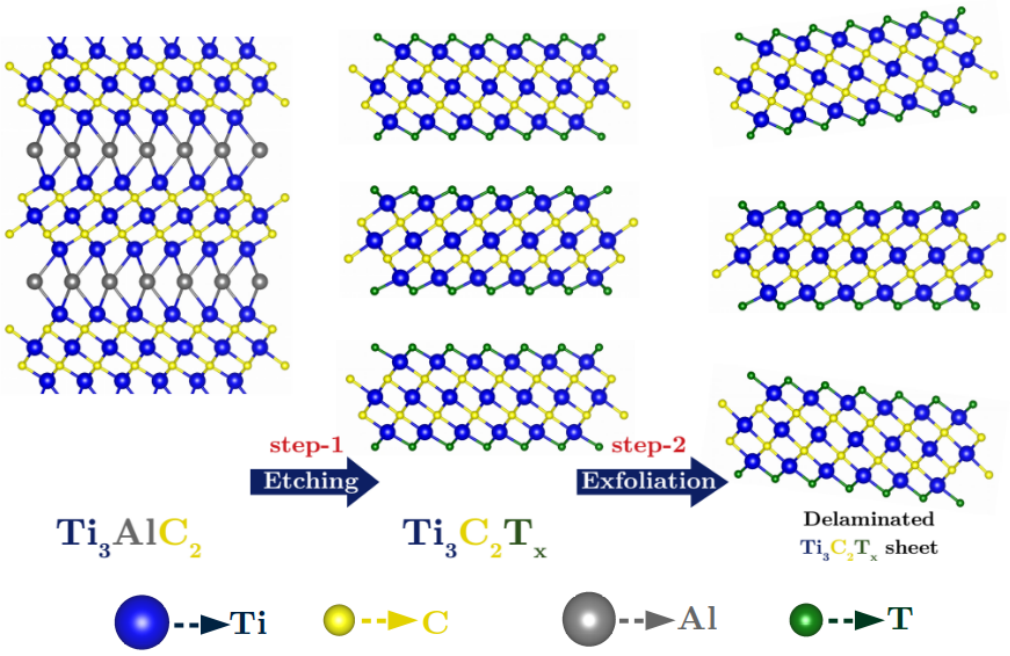

Figure 1.5: The two steps of $Ti_3C_2T_x$ MXene synthesis from 3D precursor Ti_3AlC_2.

relatively strong metallic bonds between M and A in the corresponding MAX phases are replaced by weaker bonds with -OH, -O or -F resulting in multilayered MXenes. To get a single layer MXene it is important to exfoliate it from its multilayered structure (step-2 as shown in Figure 1.5). The method, typically used for exfoliation, is intercalation with large organic molecules, intercalation with cations,shaking and/or sonication. The process of exfoliation depends on the etching agents. For example, Li^+ ion will be used for intercalation if LiF/HCl is used as etching agent[18], faciliating their exfoliation by simple shaking or sonication[19].
The next subsection discusses the synthesized and theoretically predicted MXenes.

1.3.2 Members of MXene family

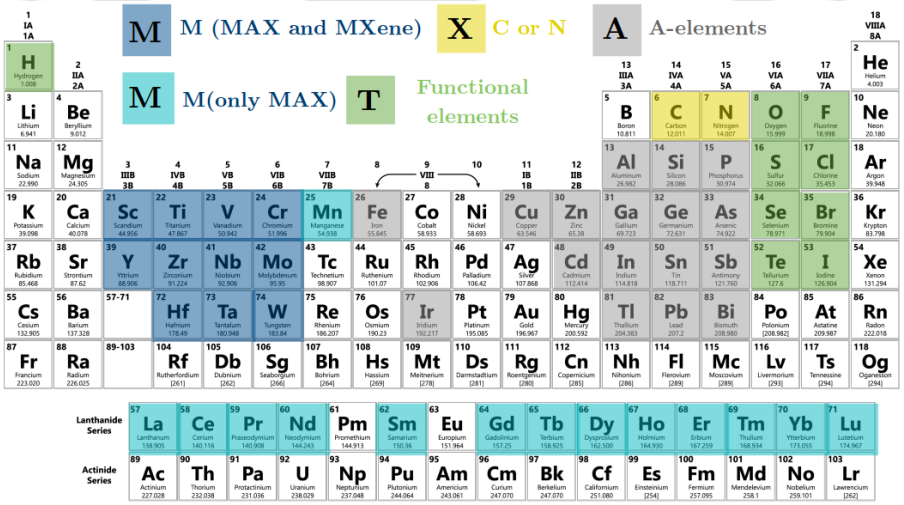

Figure 1.6: Different transition elements(M)(in MAX and MXene), group 13-15 elements(A), X elements, functional elements(T) are shown in the perodic table with different colour codes

MXene synthesis requires successful precursor MAX phase synthesis. Over 150 MAX phase compositions have been synthesized to date[20]. Out of them, 70 synthesized MAX phases have

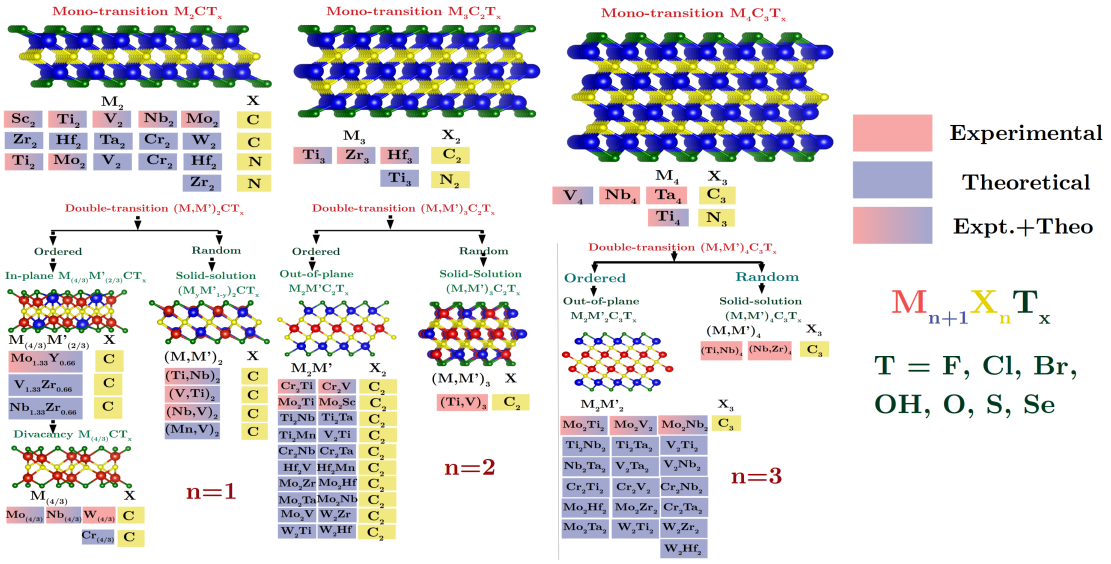

Figure 1.7: Members of MXene family investigated till date are shown. The experimentally and theoretically explored MXenes are shown with specified colour codes.

been reported before 2011[21]. After the synthesis of several MXenes, the search for transition-metal based MAX phases has also increased remarkably. Recently, lanthanide-based MAX phases have also been synthesized successfully. However, lanthanide based MAX phases are yet to be exfoliated to MXene[22]. Figure 1.6 shows different synthesized MAX and MXene elements with specified colour codes. Two MXene phases have been reported to be synthesized from the non-MAX phase. Selective etching of Ga-Ga layers from Mo_2Ga_2C results in synthesis of Mo_2CT_x[23] and removal of Al_3C_3 layers from $Zr_3Al_3C_5$ results in synthesis of $Zr_3C_2T_x$[24].
Figure 1.7 shows the different classes of $M_{n+1}X_n$ with n = 1, 2, 3. In Figure 1.7, pink and blue colours specify the experimentally synthesized and theoretically explored MXenes, respectively[21]. When two different transition metals are combined to synthesize the precursor MAX phase, the double-transition metal MXene is synthesized. The double-transition metal MXenes can be of two types, as shown in Figure 1.7; one is random, and the other is ordered. The ordered double-transition metal MXenes are categorized into in-plane and out-of-plane ordered MXenes. The in-plane ordered double transition metal MXenes exist only in M_2CT_x phase, while out-of-plane ordered one exist in $M_3C_2T_x$ and $M_4C_3T_x$ phases[25]. If two different transition metals M and M′, occupy the same M plane along different orientations in M_2CT_x structure, the give rise to in-plane ordered MXene (i-MXene) with general formula $M_{\frac{4}{3}}M'_{\frac{2}{3}}CT_x$. Further etching removes the M′ from the system and results in ordered divancancy MXene with formula $M_{\frac{4}{3}}CT_x$. When two different transition metals, M and M′, occupy two different M layers in $M_3C_2T_x$, $M_4C_3T_x$, an out-of-plane ordered double transition-metal MXene is formed. The corresponding fomulae are $M_2M'C_2T_x$ and $M_2M'_2C_3T_x$, the M′ are in the central M-layer. In a random solid solution MXene, M and M′ randomly occupy any M sites in the same M planes. These kinds of solid solution provides a full range of mixing of M and M′ and are more applicable in tuning any target property by tuning the compositions. $(Mo,V)_4C_3T_x$ is a solid-solution MXene with limited range of mixing compositions[26]. $Mo_4VC_4T_x$ is an example of ordered M_5C_4 MXene with twining at the central M layer[27]. $(Ti,Ta)_5C_4T_x$ and $(Ti,Nb)_5C_4T_x$ are two M_5C_4 solid-solution MXenes that are came into existance recently[28]. MXene solid solution with four or more transition elements, the high-entropy MXenes has been synthesized MXenes[29]-[30]. Solid solution MXene with mixing in the X site also exists. Recently, $Ti_2(C_yN_{1-y})T_x$, $Ti_3(C_yN_{1-y})_2T_x$ and $Ti_4(C_yN_{1-y})_3T_x$ solid-solutions have been synthesized[31]. Ordered Ti_3CNT_x is an ordered MXene where one X layer is by C atoms and another by N atoms.[32]
The following subsection discusses how the compositional and structural diversity gives rise to many exotic properties of MXenes

1.3.3 Properties of MXenes

Two-dimensional materials show unique and exotic mechanical, electronic, thermal, and optical properties than their bulk counterparts. MXenes are no exceptions to that. Since the discovery of MXene in 2011, a substantial amount of theoretical and experimental research has been going on to explore and/or tune various properties by playing around with the compositions of M or X, surface terminations, doping with foreign elements, to name a few. Here, we provide an overview of the mechanical, electronic, and surface properties of MXenes.

Mechanical Properties

The mechanical properties of MXenes are the first to be studied by first principle calculations[33]. Figure 1.8 shows a comparative c_{11} plot of M_2AC and corresponding pristine MXenes (data are adapted from the Ref [33]). When pulled along the basal plane, the transition metal carbide sheets possess a twice higher c_{11} value than the MAX phase. This same trend is observed in higher order, *i.e*, in MXenes with n=2 and 3 too. Experimental measurements show Young's Modulus of $Ti_3C_2T_x$ is 333±30 GPa[34], close to simulated value of 300 GPa for $Ti_3C_2(OH)_2$ [35] and 386 GPa for $Ti_3C_2O_2$[35]. These values are 60% higher than MoS_2 and graphene oxide. $Nb_4C_3T_x$ has Young's Modulus of 390 GPa[36], much higher than graphene oxide and reduced graphene oxides. MXenes shows a combination of mechanical stiffness, bending rigidity[37], and flexibility, making it suitable for device applications like batteries, sensors, supercapacitors, wearable electronics, etc.

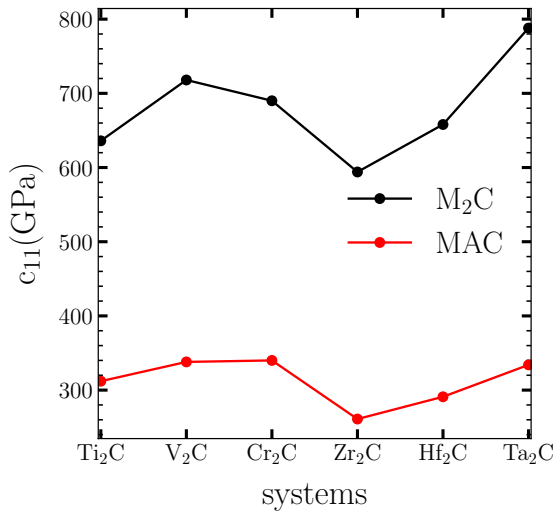

Figure 1.8: comparative c_{11} plot of pristine M_2C MXene and corresponding MAX phases.

Electronic Properties

It is clear from Figure 1.7 that the theoretical study of MXenes is more volumnous as compared to the experimental research. Electronic structure calculations reveal that pristine MXenes show metallic ground states. The physics changes when the surface functionalizations come into the picture. The competition between the 'd' orbitals of transition elements and 'p' orbitals of carbon and functional atoms changes the electronic structures. For example, -O functional Ti_2C is a semiconductor with a band-gap of 1.0 eV in the ground state, while pristine and -F, -OH functional Ti_2C are metallic[38]. The electronic structure again changes when more layers come into picture. Ti_2CO_2 is semiconductor but $Ti_3C_2O_2$ and $Ti_4C_3O_2$ are metallic in nature[39]. With increasing number of Ti planes, d-states start filling out the band-gap of Ti_2CO_2 at the Fermi level and thus restore the metallic behavior. $Mo_2TiC_2T_x$ is the first synthesized out-of-plane ordered double-transition element MXene[40]. Its structure resembles $Ti_3C_2T_x$ with outer Ti layers replaced by Mo layers. Both the MXenes are metallic in nature.

A correlation is observed between the valence electronic configuration and the ground state electronic structure. The iso-electronic transition element-based -O functional MXenes show the same electronic behavior. For example, Ti, Zr, and Hf are the same group elements, and -O functional Ti, Zr, and Hf carbide MXenes are semiconductors in the ground state[41]. (V, Nb, Ta) and (Cr, Mo, W) are group IVB and VB elements, respectively, follow this trend. -O passivated (V, Nb, Ta) MXenes are metallic[42],[43],[44], while (Cr, Mo, W) are topological insulators[45]. Electronic structure calculations show that ordered double transition element MXenes with -O passivation, $M_2M'C_2O_2$ and $M_2M'_2C_3O_2$ (M′ in the central layers)(M= Mo, W; M′ = Ti, Zr, Hf), are topological insulators and topological semi-metals, respectively[46]. $Mo_2M'C_3O_2$ (M′ = Ti, Zr, Hf) show spin Hall effect at room temperature due to the presence of significant topological gaps(0.1-0.2 eV)[47]. Theoretical studies show that by tuning the amount of surface passivation,

location and orientation of functional groups, compositions of transition, and X elements, one can adjust the valence band maxima, conduction band minima, redox potential, and overpotentials to improve target properties.

Surface Properties

Surface properties bear significant importance for MXenes as their surfaces get passivated during synthesis process as discussed in section 1.3.1. The passivated elements and amount of passivation can be controlled by controlling the amount of reactant, reaction conditions, etc. MXene posses a combination of high electrical conductivity ($Ti_3C_2T_x$ shows a conductivity of 24000 Scm^{-1}[48], much higher than Graphene) and high hydrophilicity due to presence of functional groups -F, -O, -OH, etc. The passivated units, -F, -O; make the MXene surface negatively charged. Theoretical studies show that surface passivation affects the work function of the MXenes. For example, the presence of -O groups increases, and -OH groups decrease the work functions compared to the bare MXenes[49]. The surface and conductive properties make MXene a potential candidate for electrochemical energy storage devices. However, there is one disadvantage of MXene due to this surface passivation. They gets oxidized in presence of air because of surface hydrophilicity, leading to their degradation.

$Ti_3C_2T_x$, the first discovered MXene caught the world's attention for its promising energy storage performance. The high conductivity, hydrophilicity, mechanical stiffness, flexibility, and bending rigidity make $Ti_3C_2T_x$ an excellent competitor of graphene in energy storage applications[50],[51]. The presence of surface groups enables the surface redox activity of $Ti_3C_2T_x$, which is advantageous over graphene. Later, the MXene family expanded with the synthesis of new other MXenes. Applications of MXene are not limited to the energy storage field only. The diverse structure, compositions, and surface passivations make it versatile in several application fields. It has been explored in various areas like hydrogen storage[52], catalysis[53], thermoelectrics[54], opto-spintronics[55], optoelectronics[56], wearable electronic devices[57], neuromorphic computing[58], electromagnetic interference shielding[59], and biomedical areas[60]. As we aim to explore various factors affecting the energy storage performance of MXenes, we are keeping our discussion limited to only energy storage applications of MXenes.

1.3.4 Energy Storage Applications of MXenes

MXene has been exfoliated for a new anode material for the Li-ion battery[61]. $Ti_3C_2T_x$ possess five times smaller lithium ion diffusion barrier than TiO_2 anatase and graphite[50]. It shows a gravimetric capacity of 410 $mAhg^{-1}$, higher than that of graphite[50]. Mo_2CT_x shows a capacity of 423 $mAhg^{-1}$, higher than $Ti_3C_2T_x$[62]. MXenes with n=1 structure, for example, Ti_2CT_x[63], Nb_2CT_x[64], V_2CT_x[64] and Sc_2CT_x are more promising than $Ti_3C_2T_x$ or any other higher n MXenes. Theoretical investigation shows that Ti_2CT_x can accomodate 50% more Li-ions than $Ti_3C_2T_x$[63]. One TiC inactive layer in $Ti_3C_2T_x$ prevents Li-ion storage[63]. An experiment reported 1.5 times higher Li-ion uptake is possible in Ti_2CT_x than $Ti_3C_2T_x$[65]. Nb_2CT_x and V_2CT_x exhibit higher Li-ion capacity than Ti_2CT_x[64]. It is theoretically explored that -O surface passivation favors Li-ion adsorption compared to -F and -OH terminations[66],[50]. The theoretical study and experimental verification claim that continuous change in the oxidation state of transition elements is the mechanism behind the enhanced Li-ion storage in MXene[51]. Theory suggests that MXene is useful as an anode for Na, K, Mg, Ca, and Al batteries, too[67],[68]. One major drawback of MXene is it stacks during the charge/discharge process, which results in lower ion diffusion. Ren and co-workers used a composite of carbon nanotube spacer with $Ti_3C_2T_x$ flakes to prevent the stacking and reported four times higher capacity for Li-ion storage than $Ti_3C_2T_x$[69]. Hybridization is another method to improve the performance, MoS_2/Ti_3C_2@C is one of such example[70]. MXene's unique surface passivated structure provides a way of surface engineering. Halogeneting $Ti_3C_2T_x$, *i.e* that is passivating surfaces with halogen group elements or their mixtures, made this MXene a promising cathod material for Zn-ion batteries[71].
Gogotsi and his team first demonstrated electrochemical intercalation of Li^+, Na^+, K^+, Mg^{2+}, NH_4^+ and Al^{3+} from aquous salt solution between the $Ti_3C_2T_x$ layers[72],[73],[74]. Multilayered $Ti_3C_2T_x$ performed better than carbon and activated graphene as a supercapacitor electrode in the presence of a basic(KOH) electrolyte. $Ti_3C_2T_x$ shows a capacitance of 340 F/cm^3 , whereas,

the value is 180 and 200-350 F/cm^3 for carbon and activated graphene, respectively[18],[75],[72]. An enhancement in capacitance value of $Ti_3C_2T_x$ is observed, in presence of an acidic(H_2SO_4) electrolyte. It shows capacitance of 900 F/cm^3 at scan rate of 2 mVs^{-1}[18]. The huge difference in capacitance of $Ti_3C_2T_x$ is observed when exposed to basic and acidic solutions could be explained by the charge storage mechanism. In basic solution, $Ti_3C_2T_x$ shows only EDL mechanism, whereas in acidic solution it exhibits both EDL and redox mechanism. It is established theoretically and experimentally that the significant presence of -O surface functional groups leads to major redox contributions, and -F, -OH leads to EDL contributions[76]. Simon *et.al.* first reported that the change in the oxidation state of Ti in $Ti_3C_2T_x$ during charging/discharging is the reason for the high electrochemical performance of it in acidic electrolyte. Different synthesis techniques of MXene also affect the capacitive performance. $Ti_3C_2T_x$ hydrogel shows a volumetric capacitance of 1500 F/cm^3 at 2 mVs^{-1} scan rate in H_2SO_4 electrolyte[77]. Other MXenes like, V_2CT_x, Mo_2CT_x, Ti_2CT_x have been explored experimentally for supercapacitive performance. V_2CT_x exhibits a high capacitance of 487 F/g at a scan rate of 2mV/s in 1 M H_2SO_4 solution[78]. Mo_2CT_x and ordered di-vacancy MXene $Mo_{1.33}CT_x$ show promising performance. The vacancy proves to be beneficial to $Mo_{1.33}CT_x$, as it shows a capacitance of 700 F/cm^3, 65 % higher than Mo_2CT_x[79],[23]. To enhance the supercapacitive performance of MXene, researchers have constructed composites of MXene, doped with foreign elements, and synthesized solid solutions. $Ti_3C_2T_x$ /HGO(holey graphene oxide) exhibit a volumetirc capacitance of 1445 F/cm^3 at scan rate 2mV/s[80].
MXene/MnO_2 heterostructure shows a capacitance of 611 F/g at 1A/g in 0.2 M KOH solution[81]. MXene/NbN composite delivers a capacitance of 900F/cm^3 at 10mV/s in 1M H_2SO_4[82]. Wang's group studied the effect of Nitrogen-doped $Ti_3C_2T_x$ MXene electrodes for supercapacitors for the first time. N-doped MXenes (N-$Ti_3C_2T_x$) with 1.7-20.7% surface nitrogen concentrations were obtained at temperatures from 200°C to 700°C under ammonia treatment[83]. They found that N-doped MXenes annealed at low temperature (200°C) exhibits a specific capacitance of 192 Fg^{-1} in H_2SO_4 electrolyte, much larger in comparison to that of pristine $Ti_3C_2T_x$ (34 Fg^{-1}). Gogotsi and co-workers studied the capacitive performance of $(Ti_yNb_{1-y})_2CT_x$ and ($V_yNb_{1-y}CT_x$) solid solutions and concludes that their capacitive performance lies between the two end point compounds[84].

The exciting results on their potentials as supercapacitor electrodes opens up the following routes of further investigation: exploration of (a) new MXenes with regard to their charge storage capacities as supercapacitor electrodes, (b) role of doping and substitution in enhancing the capacitances of pristine $M_{n+1}X_n$ MXenes, (c) understanding of the contributions of various charge storage mechanisms behind the storage capacity of a MXene electrode in a supercapacitor assembly.

1.3.5 First-principles Electronic Structure Methods and Simulation of Materials Properties

The above discussions establish that the theoretical exploration of the working mechanism of MXene is crucial in designing a supercapacitor electrode. It is essential to examine the effect of doping, substitution, surface engineering, and disorders in enhancing their electrochemical performance. However, it would be time-consuming and costly if one attempted to do this in a laboratory. Theory and simulation-based techniques provide a way to solve actual materials to get their ground state electronic properties, surface, magnetic, and mechanical properties. Theoretically, one needs to solve the Schrödinger Equation for electrons in a real solid in the presence of the effective potential of other electrons and atomic nuclei. Solving the Schrödinger Equation exactly for a many-body system is not possible. Hence, a theory is required with various approximations to overcome such a problem. The 'Density Functional Theory (DFT)' provides a way of solving the n-electron Schrödinger Equation by projecting the many-body interacting system onto a non-interacting single particle one. The many-body interactions are approximated in a single term. Density Functional Theory is the first-principles method to solve real solids in a parameter-free way. Density Functional Theory has been implemented in several advanced software to handle complex problems accurately in a reasonable time frame. Density Functional Theory has been used in computing the electrochemical performances of materials. These methods help predict the properties of new materials. Therefore, the Density Functional Theory based first-principles methods are the essential tool for the fundamental understanding of the material used during my doctoral research.

1.4 Outline of thesis

Using Density Functional Theory (DFT)[85], the well established first-principles methodology to compute materials properties in a parameter-free framework, in conjunction with thermodynamic model to address electrode-electrolyte interaction[86] in a supercpacitor assembly, in this thesis we have explored the three routes mentioned above. While we started out with computations of capacitance of Ti_3C_2, the most intensely explored MXene, the study was extended to other MXenes that are either synthesised or their precursor MAX phases are synthesised[22]. In the course of our investigations, we have explored the effects of doping, substitution, chemical disorder, magnetic disorder and asymmetric surfaces on the charge storage capacities of MXene electrodes in contact with acidic electrolyte. The chapters in the thesis are arranged the following way:

In **Chapter-I** we start by discussing in detail the importance of supercapacitor as an energy storage device followed by the history of their evolution and their construction and working mechanism. This is followed by a general overview on two-dimensional materials as materials for energy related applications. The chapter concludes with introduction of MXenes and a brief discussion of their potentials discovered till date.

Chapter-II discusses the theoretical methods used in this thesis. The chapter starts with brief description of DFT and the method for calculations of the electronic structure that has been used in this dissertation. This is followed by the models that have been used in conjunction with DFT to simulate the electrode-electrolyte interactions. Two different approaches have been used in this thesis: one a much simpler one where the adsorption of protons from acidic electrolytes on the negative charged MXene electrode surface is considered by "Rigid Band Approximation"[87] that is the adsorption of a proton does not change the band structure substantially but only shifts it rigidly. This formalism, though does not perform an ensemble averaging of the various configurations possible in an interacting electrode-electrolyte assembly, captures the essential physics. The other method, the Joint Density Functional Theory (JDFT) is an *ab iniito* method that combines the quantum mechanical DFT for solid electrodes with a classical DFT for aqueous electrolytes, uses implicit solvation models to address the electrode-electrolyte interactions[88]. Complete statistical minimisation of thermodynamic potentials is done in this method enabling extraction of the contributions of different mechanisms towards charge storage in a quantitative manner. Details of both methods are elucidated in this chapter.

In **Chapter-III**, we perform a systematic investigation of the electrochemical properties of pristine and O-functionalised Ti_2C, V_2C, Nb_2C, Mo_2C, Ti_3C_2, and Nb_3C_2 MXenes[89]. Sll MXenes except Nb_3C_2 are synthesised recently. However, their utilities as supercapcitor electrodes have not yet been assessed. Here we attempt to do that. We systematically explore the variations in the capacitances as we move across MXenes made up of transition metal constituents from $3d$ to $4d$ electrons and provide microscopic insights into the trends observed. We find that all the compounds explored will display excellent charge storage capacity when used as negative electrode, and that there is hardly any difference in the capacitances irrespective of which series of transition metals M is from. In this work, we also propose $Nb_{n+1}C_n$ as a potential new electrode material with capacities at par with other MXenes that are synthesised and/or investigated.

Doping and substitutions are standard procedures to improve upon the physical properties of materials. A couple of experiments on the effects of Nitrogen doping on the electrochemical properties of functionalised Ti_3C_2 MXene electrodes in various aqueous electrolytes have been performed recently; the outcomes have been mixed[83, 90]. In **Chapter-IV**, we have attempted to interpret the results of the experiments through detailed calculations exploring various sites of doping. We find that the redox mechanism is dominant and that the doping at the functional site yields the best values of the capacitance whose origin lies in the structural aspects of the systems[91]. As such our results are in good agreement with one of the experiments. Additionally, we investigate the effects of substitutions at the X and M sites by Nitrogen and Molybdenom, respectively. Our results show that the improvements due to substitutions are not as great as ones observed upon doping. In the light of these results, we discuss in detail the limitations in making a direct comparison between the theory and the experiment in this context.

Recently, double transition metal MXenes with chemical formula $(MM')_{n+1}X_n$ have shown interesting structure-property relationships. At the same time, Janus structures for layered compounds have exhibited exciting properties, the origin of which lies in the asymmetry of the surfaces due to the differences in their constituents[92, 93, 94, 95]. A MXene with Janus structure can be obtained with $n = 1$. In **Chapter-V** we have explored a route to enhance the charge storage capacity of MXene electrodes in acidic electrolyte by construction of Janus MXenes. Although Janus MXenes are yet to be synthesised, we have taken cue from the fact that several solid solution MAX phases with chemical formula MM′C have been realised and investigated three functionalised Janus systems $NbVCT_x$, $MnVCT_x$ and $CrMnCT_x$; T_x stands for functional groups. We find that Janus MXenes have superior charge storage capacities in comparison to their end point counterparts M_2CT_x. Our calculations attribute such behaviour to the co-operative behaviour of EDL and redox mechanisms upon formation of Janus structures. The results of this chapter bears significance in terms of paving new ways to exploit the flexibility in structure and compositions among members of the MXene family to realise superior functional properties.

Although a few MXenes[96] and MAX compounds with magnetic constituents have been synthesised, the role of magnetism in shaping up other functional properties in them has not been explored at all. The study about the effects of chemical disorder on properties of MXenes, particularly with regard to applications in supercapacitors, too, has been a handful. In **Chapter-VI** we examine the effects of both chemical and magnetic disorder on the charge storage capacities of solid solution $V_{2-x}Mn_xCT_x$ MXenes. In this work we find a correlation between the charge transfer and magnetic configurations of the surfaces that significantly affects the redox part of the electrical capacitance. This is a significant result as it enables one to design the MXene surfaces to boost the charge storage capacity. Although the results obtained are for a specific chemical composition, there is a scope for this to be generalisable. The experimentalists can use this feedback to design new supercapacitors with enhanced storage capacities by choosing appropriate temperature and the voltage window.

The concluding **Chapter-VII** discusses the open problems in the field and the possible extensions of the work presented in the thesis.

Chapter 2

Methodology

This chapter describes the theoretical background used in this thesis for materials simulations. After introducing the first-principles approach to simulate material properties, we discuss 'Density Functional Theory (DFT)', the backbone of ab initio calculation of materials properties in complex systems. After a brief discussion of Pseudopotential method in construction of the ab initio calculations used in this thesis we introduce a variant of DFT , the 'Joint Density Functional Theory,' necessary to simulate the electrode-electrolyte interactions in an actual supercapacitor set up. Detailed discussions on structural models of MXenes and the procedures to compute the charge storage capacities due to different sources follow thereafter.

2.1 First-principles Approach

Loius de-Broglie′s imagination of particle and wave as a single entity, "matter wave," in 1924 established the foundation of today′s quantum description of the matter world. The following equations give the mathematical description of the wave-particle duality of matter,

$$p = \frac{h}{\lambda} \tag{2.1}$$

$$E = h\nu \tag{2.2}$$

where p and E are the momentum and energy of the particle and λ, ν are the wavelength and frequency. 'h' is the Planck′s constant and has a value of 6.626×10^{-34} joule-second. According to equations (2.1) and (2.2), the wave nature of the electron is noticeable due to its relatively minimal mass than our everyday objects. The particles like electrons need a description considering their wave nature.
In 1926, Erwin Schrödinger gave the wave equation, known as famous Schrödinger equation. The equation is

$$\hat{H}\Psi(\mathbf{r}_i, \mathbf{r}_I, t) = E\Psi(\mathbf{r}_i, \mathbf{r}_I, t) \tag{2.3}$$

$\hat{H}$, Ψ and E are the Hamiltonian operator, wave function, and system Energy, respectively. r_i and r_I are the coordinates of the electron and nucleus, respectively.
The $\hat{H}$ has the form,

$$\hat{H} = E_i^{kin} + E_I^{kin} + U_{iI} + U_{ij} + U_{IJ} \tag{2.4}$$

where, E_I^{kin} and E_i^{kin} are the kinetic energies of nuclei and electrons, respectively. U_{iI}, U_{ij}, and U_{IJ} are the potential energies due to Coulomb interaction between electron-nucleus, electron-electron and nucleus-nucleus, respectively. The Schrödinger model of electrons and nuclei is complex and can be solved only for hydrogen-like systems. There are some simplifications have been introduced to deal with this problem. The assumptions are following,

- One can eliminate the time variable by restricting the interest to the ground-state energy of electrons. The potential energy of the system is constant in time.
- One can eliminate the time variable by restricting the interest to the ground-state energy of electrons. The potential energy of the system is constant in time. Nuclei are more massive than electrons(1836 times for hydrogen). The electrons respond instantaneously to nuclear motion and always occupy the ground state of that nuclear configuration. The nuclei

are considered 'frozen' from the electron′s view. This approximation is known as **Born-Oppenheimer approximation(1927)**[97].

The above two approximations simplify the Schrödinger equation (2.3). The resulting equation, known as **time-independent electronic wave equation** is given as,

$$\hat{H}\Psi(\mathbf{r}_i) = E\Psi(\mathbf{r}_i) \tag{2.5}$$

The kinetic and potential energy terms related to nuclei are omitted under the Born-Oppenheimer approximation, and $\hat{H}$ operator becomes,

$$\hat{H} = E_i^{kin} + U_{iI} + U_{ij} \tag{2.6}$$

The terms of equation (2.6) are expressed as (in atomic units),

$$E_i^{kin} = -\frac{\hbar^2}{2m}\sum_i^n \nabla_i^2 = -\frac{1}{2}\sum_i^n \nabla_i^2 \tag{2.7}$$

where ∇^2 is the Laplacian operator.

$$U_{iI} = -\sum_I^N \sum_i^n \frac{Z_I}{|\mathbf{r}_{Ii}|} \tag{2.8}$$

where N and n are the number of nuclei and electrons in the system. Z_I are the charges of the nuclei. The interaction of all electrons to all nuclei is taken care of by the double summation.

$$U_{ij} = \frac{1}{2}\sum_{i\neq j}^n \frac{1}{|\mathbf{r}_{ij}|} \tag{2.9}$$

The simple form of Schrödinger equation works for hydrogen and helium atoms. However, solution of a system containing n-electrons interacts where each electron with all other electrons simultaneously is tricky. In the following we discuss the Hartree and the Hartree-Fock(HF) methods to solve interacting n-electron Schrödinger equations.

2.1.1 Hartree Method

In 1928, Hartree attempted to solve the interacting n-electron many-body problem by assuming that each electron is independent and interacts with others in an averaged way[98]. One electron is now experiencing a mean field of other electrons. An n-electron system becomes a set of non-interacting one-electrons where each electron feels the average field due to the rest. The wave equation becomes,

$$\left(-\frac{1}{2}\nabla^2 + U_{ext}(\mathbf{r}) + U_H(\mathbf{r})\right)\Psi(\mathbf{r}) = E\Psi(\mathbf{r}) \tag{2.10}$$

where U_{ext} is the attractive interaction between electrons and nuclei, and U_H is the Hartree potential. The Hartree potential is the classical Coulomb repulsive interaction between each electron and the mean field. The total energy is the sum of n one-electron energies,

$$E = E_1 + E_2 + \cdots + E_n \tag{2.11}$$

The n-electron wave function becomes the product of n one-electron wave functions,

$$\Psi = \Psi_1 \times \Psi_2 \times \cdots \times \Psi_n \tag{2.12}$$

For many electron systems, this method can provide a crude estimation of the ground state. The reason for the failure of this method for many-electron systems are

- It does not consider Pauli′s exclusion principle.
- It does take into account electron-electron interactions of a n-electron system.

2.1.2 Hartree-Fock Method

In 1930, Fock introduced a new solution technique using the mean-field approach by Hartree. Fock modified the Hartree wave function and used variational process[99]. The n-electron wave function is expressed as a linear combination of non-interacting one-electron wave functions in the form of Slater determinant. The wave function of a system with 2 electrons thus becomes,

$$\Psi(\mathbf{r}_1,\mathbf{r}_2)=\frac{1}{\sqrt{2}}\begin{bmatrix}\Psi_1(\mathbf{r}_1) & \Psi_2(\mathbf{r}_1)\\ \Psi_1(\mathbf{r}_2) & \Psi_2(\mathbf{r}_2)\end{bmatrix}=\frac{1}{\sqrt{2}}[\Psi_1(\mathbf{r}_1)\Psi_2(\mathbf{r}_2)-\Psi_2(\mathbf{r}_1)\Psi_1(\mathbf{r}_2)] \tag{2.13}$$

When two rows and columns are exchanged, the determinant changes sign, guaranteeing the anti-symmetry of the electron wave function.

$$\Psi(\mathbf{r}_1,\mathbf{r}_2)=-\Psi(\mathbf{r}_2,\mathbf{r}_1) \tag{2.14}$$

If one considers the spin variable to the wave function the electron wave function becomes,

$$\Psi(\mathbf{r}_1,\mathbf{r}_2,\uparrow,\downarrow)=\frac{1}{\sqrt{2}}\begin{bmatrix}\Psi_1(\mathbf{r}_1,\uparrow) & \Psi_2(\mathbf{r}_1,\downarrow)\\ \Psi_1(\mathbf{r}_2,\uparrow) & \Psi_2(\mathbf{r}_2,\downarrow)\end{bmatrix} \tag{2.15}$$

If two electrons occupy the same spin wave functions, the determinant would be zero; implying that such wave function does not exist. This satisfies the Pauli′s Principle. The Slater determinant can be written for n-electron system as,

$$\Psi(\mathbf{r}_1,\mathbf{r}_2,....,\mathbf{r}_n)=\frac{1}{\sqrt{n!}}\begin{bmatrix}\Psi_1(\mathbf{r}_1) & \Psi_2(\mathbf{r}_1) & \cdots & \Psi_n(\mathbf{r}_1)\\ \Psi_1(\mathbf{r}_2) & \Psi_2(\mathbf{r}_2) & \cdots & \Psi_n(\mathbf{r}_2)\\ \vdots & \vdots & \vdots & \vdots\\ \Psi_1(\mathbf{r}_n) & \Psi_2(\mathbf{r}_n) & \cdots & \Psi_n(\mathbf{r}_n)\end{bmatrix} \tag{2.16}$$

where $\frac{1}{\sqrt{n!}}$ is the normalization factor for n-electron system. After feeding the Slater determinant to the Schrödinger equation(2.6), the energy E of the system expressed as,

$$E=\sum_{i,j}\int\Psi_i^*(\mathbf{r})\left(-\frac{1}{2}\nabla_i^2+U_{ext}(\mathbf{r})+U_{ij}(\mathbf{r})\right)\Psi_i(\mathbf{r})d\mathbf{r} \tag{2.17}$$

The final expression of the total energy becomes,

$$E=E_{kin}+E_{ext}+E_H+E_x \tag{2.18}$$

The last term of equation (2.17) gives rise to E_H and E_x: the Coulomb interaction energy between electron i with j, known as Hartree energy and the exchange energy coming from the antisymmetric nature of wave function in the Slater determinant. The interaction between the electrons with same spin is called exchange effect, whereas the interaction between electrons with different spins is known as the correlation effect.
The analytical solution of the HF method is possible for a simple system like He, which comprises of one proton and two electrons. The HF calculation gives the ground state energy -77.5 eV, close to the experimental value of -78.98 eV. The HF method leads to inaccurate results in many cases as it considers the **exchange** part exactly but neglects the **correlation** effect, altogether.
With the introduction of the Slater determinant for the wave function and the mean-field approximation, the HF method could capture the physics of materials. However, it can only be applied to small systems with atoms of the order of tens. In the next section, we discuss the groundbreaking scheme of Kohn and Sham, known as the **Density Functional Theory**, which provided the idea to solve Schrödinger Equation for solids.

2.2 Density Functional Theory

The foundation of Schrödinger wave equation is based on the very origin of Physics and requires only single input data, the atom numbers, to solve a quantum system. However, in practice, solving for a real material is difficult due to the many-body effect. An n-electron system requires to solve 3n-coupled partial differential Schrödinger equation. There are no computers that can handle such

monumental task. The First-principle methodology took a quantum leap in 1964 with two powerful theorems by Hohenberg and Kohn that put electron density, instead of wave function, at the centre stage[100]. In 1965, Kohn and Sham provided an implementable scheme for solid state systems. These two put together and is famously known as **Density Functional Theory(DFT)**[101].
Hohenberg and Kohn proposed two theorems and proved that electron density is the key quantity. The theorems link the electron density to the external energy, Hamiltonian, and wave function. The theorems are as follows,

- The external potential(U_{ext}) is uniquely determined by the electron density $\rho(\mathbf{r})$, so that the total energy is a unique functional of the density $E[\rho]$.[102]
- The true ground state density(say, ρ_0) minimizes total energy functional $E[\rho]$ and the resulting minimum energy is the ground state energy E_0.[102]

The ground state energy of interacting electrons in an external potential(U_{ext}) is given by energy functional

$$E[\rho] = F[\rho] + \int U_{ext}(\mathbf{r})\rho(\mathbf{r})d\mathbf{r} \tag{2.19}$$

$F[\rho]$ is a universal functional of the electron density $\rho(\mathbf{r})$, and the second term of equation 2.19 is the interaction energy with the external potential. The total energy in the ground state is determined by minimizing $E[\rho]$ using the variational principle.
In 1965, Kohn and Sham proposed the formalism of DFT using Hohenberg and Kohn theorems. The merit of DFT lies in mapping the many-electron problem onto a single-electron problem and leads to a Schrödinger like single electron equation in an effective potential, known as Kohn-Sham equation. The many-electron effects are taken into account in the effective potential. The Kohn-Sham equation is given by,

$$(H_{KS} - \epsilon_i)\phi_i(\mathbf{r}) = 0 \tag{2.20}$$

where, H_{KS}, ϵ_i and ϕ_i are the Kohn-Sham Hamiltonian, single-electron energy eigenvalue and single electron orbital, respectively. The Kohn-Sham Hamiltonian (H_{KS}) is given as,

$$H_{KS} = -\frac{1}{2}\nabla^2 + U_{eff} \tag{2.21}$$

where,

$$U_{eff} = U_{ext}(\mathbf{r}) + U_H(\mathbf{r}) + U_{xc}(\mathbf{r}) \tag{2.22}$$

Here, U_{ext}, U_H and U_{xc} are the external potential on the single electron due to nuclei, the Hartree potential, and the exchange-correlation potential due to electron-electron interaction. V_{xc} is defined as ,

$$V_{xc} = \frac{\delta E_{xc}(\mathbf{r})}{\delta\rho} \tag{2.23}$$

The density of the system is the sum of the individual electron orbital and is given as

$$\rho(\mathbf{r}) = \sum_{i=1}^{n} |\phi_i(\mathbf{r})|^2 \tag{2.24}$$

The total number of electrons is expressed as ,

$$N = \int \rho(\mathbf{r})d\mathbf{r} \tag{2.25}$$

The Kohn-Sham energy functional (E_{KS})(ground state energy) of the electronic system is given by,

$$E_{KS} = T_s[\rho] + \int U_{ext}(\mathbf{r})\rho(\mathbf{r})d\mathbf{r} + E_H[\rho] + E_{xc}[\rho] \tag{2.26}$$

The Kohn-Sham equation(2.20) is solved in a self-consistent way by starting with an initial guess of electron density($\rho(\mathbf{r})$) and $E_{xc}[\rho(\mathbf{r})]$. The self-consistent procedure is shown by a flowchart in Figure 2.1.

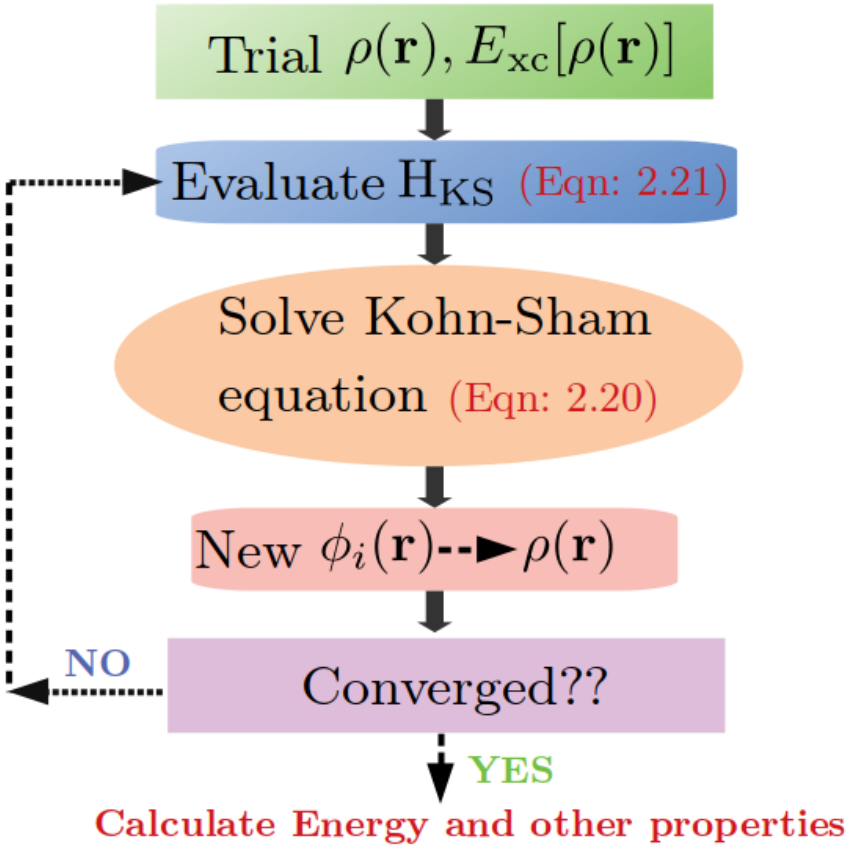

Figure 2.1: The self-consistent procedure to solve Kohn-Sham Equation

The Kohn-Sham theory is exact in principle, but the precise form of E_{xc} is unknown, except for the free (homogeneous) electron gas. Some approximations have been considered for E_{xc}. The simplest approximation for the varying electron densities is assuming the electrons see the overall system in the same way as they see locally. The electron density in a solid is considered a homogeneous electron gas, and this approximation is known as Local Density Approximation (LDA)[101]. The E_{xc} in LDA approximation is given as,

$$E_{xc}^{LDA}[\rho] = \int \rho(\mathbf{r})\epsilon_{xc}^{homo}(\rho(\mathbf{r}))d^3r \tag{2.27}$$

where $\epsilon_{xc}^{homo}(\rho(\mathbf{r}))$ is the exchange-correlation energies per electron with electron density $\rho(\mathbf{r})$ for homogeneous electron gas. This LDA works reasonably where the charge density varies slowly, like covalent systems and simple metals. The surprising success of the LDA is partly due to the cancellation of errors in overestimation exchange energy (E_x) and in underestimating correlation energy(E_c), which implies LDA gives the correct sum rule for the exchange-correlation hole. However, real systems are not homogeneous and have varying density around the electrons. By considering the gradient of electron density($\nabla\rho(\mathbf{r})$) along with electron density ($\rho(\mathbf{r})$) gives more accurate E_{xc} functional. This approximation is known as Generalized Gradient Approximation(GGA)[103]-[104] and the energy functional is written as,

$$E_{xc}^{GGA}[\rho] = \int \rho(\mathbf{r})\epsilon_{xc}^{GGA}(\rho(\mathbf{r}), |\nabla\rho(\mathbf{r})|)d^3r \tag{2.28}$$

There exists many GGA funtionals, out of which, PW91 (Perdew *et.al.* 1992) and PBE [105](Perdew, Burke and Ernzerhof 1996) functionals give accurate results for most of the systems.

2.2.1 Pseudopotential(PP) Method

According to Bloch′s theorem, the wave function of an electron in a band is expanded using a discrete set of plane waves. However, a plane wave basis set is not suitable for electronic wave functions. Many plane waves are required to expand the tightly bound core orbitals. The representation of rapid oscillations of the wave function of the valence electrons in the core region would be cumbersome using a plane wave basis set. The concept of pseudopotentials(PP) has removed the rapid oscillations in the wave functions of the valence electrons in the core region, which results in a smooth valence wave function in the core. A reasonable number of plane waves are required to present the pseudo-wave function . The reduction in the plane-wave basis set makes the method computationally affordable. There exist three common PPs, namely, norm-conserving PPs, ultrasoft PPs (USPPs)[106], and projector-augmented wave (PAW) PPs. PAW is the widely used PP approach, which gives accurate results in most cases.
PAW approach is proposed by Blöchl (1994)[107] and adopted by Kresse and Joubert(1999)[108]. It considers both core and parts of valence wave functions with two separate descriptions. The PAW wave function (Ψ_{PAW}) can be written as,

$$\Psi_{\mathrm{PAW}} = \Psi_{\mathrm{inter}} + \Psi_{\mathrm{core}} + \Psi_{\mathrm{net}} \tag{2.29}$$

The Ψ_{inter} and Ψ_{core} represent the valence and core electrons part. Ψ_{inter} is written with the plane-wave expansion, and Ψ_{core} is projected on a radial grid at the atom center. Ψ_{net}, the overlapping part of valence and core wave function is trimmed off to make the Ψ_{PAW}. This method returns the all-electron charge density of the valence orbitals that other PPs cannot.
Calculations presented in this dissertation are done with **PBE** functional and **PAW** method.

2.3 Joint Density Functional Theory

Quantum Density Functional Theory alone cannot address the physics and chemistry of the solute/solvent interface systems, like electrochemical cells. The thermodynamic phase space sampling complicates the solvent effects in *ab-initio* approaches. Joint Density Functional Theory (JDFT) provides an *ab-initio* theory that gives the electronic density functional description of the solute and classical density-functional description of the solvent and provides an exact description of the solvated system. In the context of this thesis, let′s consider a scenario from electrochemistry, like an electrode/electrolyte (solute/solvent) system. JDFT can accurately address the microscopic behavior of the electrostatic potential near the electrode surface. An *ab-initio* electrochemistry calculation is done by explicitly including the atoms making up the environment and performing thermodynamical averaging over the locations of those atoms. One can express free energy A of an explicit quantum-mechanical system with its nuclei at fixed locations and in thermodynamic equilibrium with a liquid

$$\mathrm{A} = \min_{\rho(\mathrm{r}),\{\mathrm{N}_\alpha(\mathrm{r})\}} \left\{ \mathrm{G}[\rho(\mathrm{r}), \mathrm{N}_\alpha(\mathrm{r}), \mathrm{V}(\mathrm{r})] - \int \mathrm{d}^3\mathrm{r}\mathrm{V}(\mathrm{r})\rho(\mathrm{r}) \right\} \tag{2.30}$$

$\mathrm{G}[\rho(\mathrm{r}),\{\mathrm{N}_\alpha(\mathrm{r})\}, \mathrm{V}(\mathrm{r})]$ is a universal functional of electron density of the explicit system $\rho(\mathrm{r})$, the densities of the nuclei of the various atomic species in the environment $\{\mathrm{N}_\alpha(\mathrm{r})\}$, and the electrostatic potential from the nuclei of the explicit system $\mathrm{V}(\mathrm{r})$. $\mathrm{G}[\rho(\mathrm{r}),\{\mathrm{N}_\alpha(\mathrm{r})\}, \mathrm{V}(\mathrm{r})]$ depends only on the nature of the environment, and its dependence on the explicit system is only through the electrostatic potential of the nuclei included in $\mathrm{V}(\mathrm{r})$ and $\rho(\mathrm{r})$, the electron density of the explicit system. The functional $\mathrm{G}[\rho(\mathrm{r}),\{\mathrm{N}_\alpha(\mathrm{r})\},\mathrm{V}(\mathrm{r})]$ can be separated into three parts,

$$\mathrm{G}[\rho(\mathrm{r}), \{\mathrm{N}_\alpha(\mathrm{r})\}, \mathrm{V}(\mathrm{r})] \equiv \mathrm{A}_{\mathrm{KS}}[\rho(\mathrm{r})] + \Omega_{\mathrm{lq}}[\{\mathrm{N}_\alpha(\mathrm{r})\}] + \Delta\mathrm{A}[\rho(\mathrm{r}), \{\mathrm{N}_\alpha(\mathrm{r})\}, \mathrm{V}(\mathrm{r})] \tag{2.31}$$

$\mathrm{A}_{KS}[\rho(\mathrm{r})]$ and $\Omega_{\mathrm{lq}}[\{\mathrm{N}_\alpha\}]$ are the standard universal Kohn-Sham electron-density functional of the explicit solute system in isolation(including its nuclei and their interaction with its electrons) and the the 'classical' density functional for the liquid solvent environment in isolation, respectively. $\Delta\mathrm{A}[\rho(r), \{\mathrm{N}_\alpha(r)\}, \mathrm{V}(\mathrm{r})]$ depicts the coupling between the solute and solvent. Implicit solvation models approximate the solvation effect and the electrolyte response. The free energy in this approximation is,

$$\tilde{A} = \min_{\rho(r)}(A_{KS}[\rho(r), \{Z_I, R_I\}] + \Delta\tilde{A}[\rho(r), \{Z_I, R_I\}]) \tag{2.32}$$

The effects of the liquid environment appears in the new term,

$$\Delta\tilde{A}[\rho(r), \{Z_I, R_I\}] \equiv \min_{N_\alpha(r)}(\Omega_{lq}[N_\alpha(r)] + \Delta A[\rho(r), N_\alpha(r), \{Z_I, R_I\}]) \tag{2.33}$$

Z_I and R_I are the charges and positions of the surface nuclei. Minimization of equation (2.32) leaves a functional in terms of only the properties of the explicit system and incorporates all the solvent effects implicitly. There are many advanced solvation models for JDFT, which include non-local effects, nonlinear dielectric response, spherically averaged liquid susceptibility ansatz (SaLSA) [109], and charge-asymmetric nonlocally determined local-electric (CANDLE) solvation model [110].

2.4 Structural Models of MXene

MXenes are exfoliated from layered 3D precursor MAX phase by chemical routes[111]. The details of the synthesis processes are given in the section 1.3.1. A single layer of MXene consists of 2n+1 of atomic layers, where one 'C' layer is sandwiched between two 'M' layers. Figure 2.2(a), (b) show the top and side view of MXene monolayer with n value 1(M_2C MXene). The outer transition metal layers are marked M_1 and M_2 in Figure 2.2(a,b).

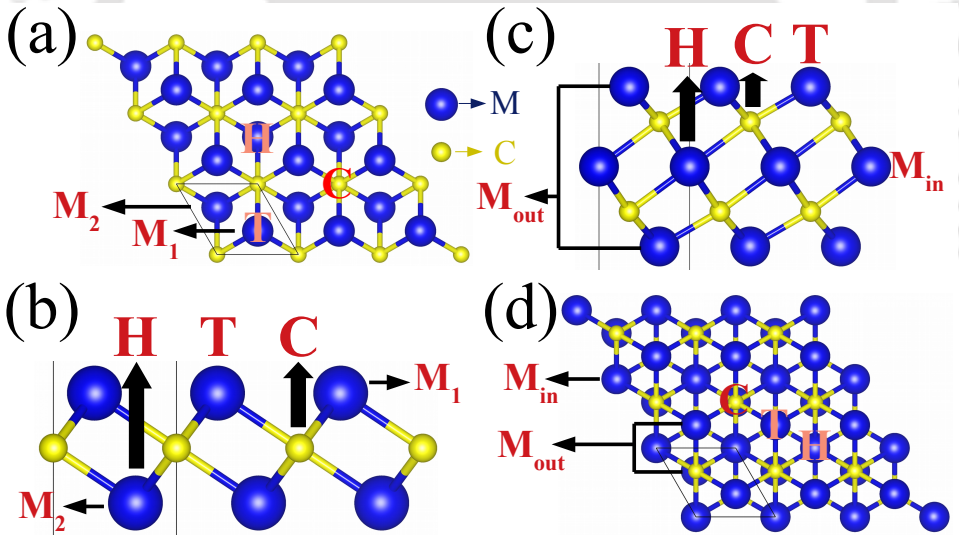

Figure 2.2: (a) Top and (b) side view of M_2C ; (c) side and (d) top view of M_3C_2. Blue and yellow balls show the 'M' and 'C' atoms respectively. MXene unit cell is shown in the figures.

In Figure 2.2(c)(side) and (d)(top), the structure of M_3C_2 MXene is shown. The inner 'M' layer is marked as M_{in} and outer 'M' layers as M_{out}. Since surface passivation by functional groups like -O, -OH, -F is inevitable during synthesis, a structural model of MXene must incorporate the preferred positions of the functional groups on the surface. Accordingly, the structural models of $M_{n+1}C_nT_x$ (T= -O, -OH, -F) are proposed in Ref [112]. For M_2C two hollow sites 'C' and 'H' over the X atom and M atom of the distant surface as shown in Figure 2.2(a,b)[112]. Another possible site is on the top of the M elements, marked as 'T' in Figure 2.2(a,b). For M_3X_2 MXene, functional elements can sit on top of the transition metal site ('T' in Figure 2.2(c,d)). The hollow sites above X atom and inner layer transition element (M_{in}) are also possible passivation sites marked as 'C' and 'H'(Figure 2.2(c,d)). Three possible passivation sites and two surfaces therefore give rise to six different configurations for passivated MXenes.

2.5 Electrochemical properties: Calculation of electrode capacitances

As discussed in the section 1.1.1, Electrochemical Double Layer Capacitance (C_{EDL}) and Redox Capacitance (C_{redox}) are the two primary charging mechanisms in an electrochemical energy storage device. Corresponding electrochemical parameters are the EDL capacitance (C_{EDL}) and Redox capacitance (C_{redox}). The total electrical capacitance is the parallel sum of these two(equation 2.34).

$$C_E = C_{EDL} + C_{redox} \tag{2.34}$$

'Quantum Capacitance' (C_Q), a contribution dependent upon the properties of the electrode material combine with C_E to yield total capacitance C_T(equation 2.35).

$$\frac{1}{C_T} = \frac{1}{C_E} + \frac{1}{C_Q} \tag{2.35}$$

The following subsections discuss the origin of C_Q, C_{EDL}, C_{redox} briefly and the calculation procedures for each one of them.

2.5.1 Quantum Capacitance, C_Q

On application of voltage to the electrode of an electrochemical charge storage device, an electrochemical double layer forms at the electrode/electrolyte interface. The macroscopic electrode potential shifts the Fermi level of the electrode materials from ϵ_f to ϵ'_f as shown in the figures 2.3. The shift in Fermi is related to a drop in electron chemical potential (say, $\Delta\mu_e$). This potential drop reduces the device's capacitance. As the reduction in capacitance arises due to electronic states of the electrode material, it is known as quantum capacitance, C_Q. For a bulk material, adding or removing a few electrons does not shift the Fermi level significantly, as shown in Figure 2.3(a). The Fermi level shift becomes significant if a finite number of states are present near the Fermi level(Figure 2.3(b)). The smaller the Fermi shift, the smaller the electron chemical potential drop($\Delta\mu_e$), the larger will be C_Q contributing less to C_T. The vice-versa is also true. The above discussion concludes that the importance of C_Q depends upon the choice of the electrode material. Let's derive the mathematical expression for C_Q. The total number of electrons in a material

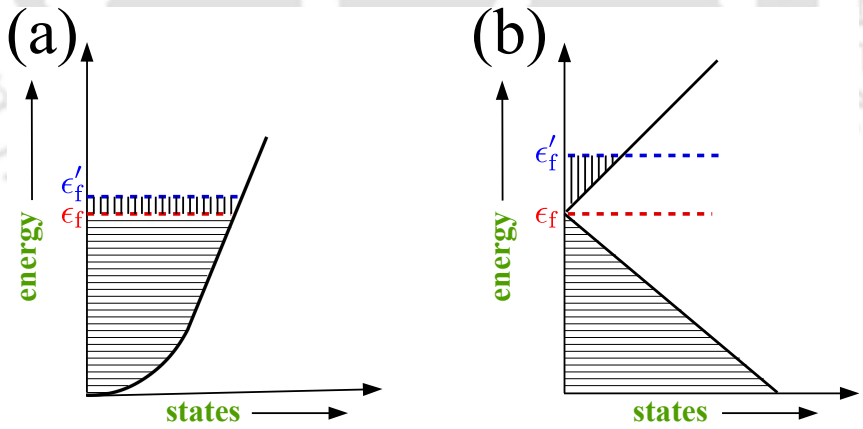

Figure 2.3: Shift in the Fermi level on application of electrode voltage for (a) Bulk electrode and (b) Finite state electrode.

before the application of electrode voltage N_0 is given as,

$$N_0 = \int_{-\infty}^{+\infty} D(\epsilon)f(\epsilon)d\epsilon \tag{2.36}$$

$D(\epsilon)$ and $f(\epsilon)$ are densities of states of the material and the Fermi-Dirac distribution function, respectively. On application of electrode potential, say V(U is the energy corresponding to it) and the total number of electrons are given as,

$$N = \int_{-\infty}^{+\infty} D(\epsilon + U)f(\epsilon)d\epsilon = \int_{-\infty}^{+\infty} D(\epsilon)f(\epsilon - U)d\epsilon \tag{2.37}$$

The change in number of electrons is given by,

$$dN = N_0 - N = \int_{-\infty}^{+\infty} D(\epsilon)[f(\epsilon) - f(\epsilon - U)]d\epsilon \tag{2.38}$$

The charge variation ($d\sigma$) corresponding to the dN is given by,

$$d\sigma = edN \tag{2.39}$$

The differential quantum capacitance (C_Q^{diff}) is the ratio of charge variation ($d\sigma$) to the electrode potential variation(dV),

$$C_Q^{diff} = \frac{d\sigma}{dN} = \frac{e^2 dN}{dV} = e^2 \int_{-\infty}^{+\infty} D(\epsilon)F_T(\epsilon - U)d\epsilon \tag{2.40}$$

where $F_T(\epsilon - U)$ is the thermal broadening function and is given by,

$$F_T(\epsilon - U) = \frac{1}{4k_B T}\text{sech}^2\left(\frac{\epsilon - U}{2k_B T}\right) \tag{2.41}$$

The quantity that gives a clear picture of the material's charge storage capacity is Integrated Quantum Capacitance (C_Q^{int}). It is given by,

$$C_Q^{int} = \frac{1}{eV}\int_0^V C_Q^{diff} dV \tag{2.42}$$

Total stored charge (Q^{int}) is given by,

$$Q^{int} = C_Q^{int} V \tag{2.43}$$

The densities of states ($D(\epsilon)$) are obtained from the self-consistent electronic structure calculations.

2.5.2 Electrical Capacitance, C_E

C_{EDL} and C_{redox} are the two contributors to the total electrical capacitance. C_{redox} can be obtained either from the slope of the integrated densities of states[113] or from the ratio of computed charge transfer (ΔQ) and the corresponding voltage change (ΔV)[114]. However, available literature shows that both approaches consider electrodes as charge neutral entity, thus, missing out on the vital effect of storing and releasing charges during the capacitor operation. In this section, we discuss two approaches adapted in this thesisthat are useful work arounds this issues. The following assumptions are adapted for the calculations: (a)the electrode is negatively charged and (b) the electrolyte is acidic (H_2SO_4), which contains H^+ as a positive ion in the solution. The two approaches, Rigid Band Approximation(RBA) Method[115] and Solvation Method[116] uses Density Functional Theory and the Joint Density Functional Theory, respectively. Following is a brief description of the two methods.

Rigid Band Approximation(RBA) Method

This method uses the model of hydrogen ion adsorption on the charged electrode to simulate the interaction process between negatively charged electrodes and positive hydrogen ions. A 3×3×1 cell of $M_{n+1}C_nO_2$ is considered for this computation. The hydrogen ions prefer to sit over the -O atom energetically. A total of nine -O sites are available to the H^+ ions for the considered cell on each face (top and bottom) of the electrode. The hydrogen ions get adsorbed over the electrode one by one. This method uses the fact that upon adding or releasing electrons, the bandstructure does not undergo any significant change, only shifts rigidly. In other words, a simple shift of the Fermi level accompanies the adsorption. During this process, C_{redox} is calculated by the ratio of charge transfer(ΔQ) to the change in the electrode potential(ΔV) and is given by,

$$C_{redox} = \frac{\Delta Q}{\Delta V} \tag{2.44}$$

ΔV is obtained from the change in work-function (ΔWF) as,

$$\Delta V = \frac{\Delta WF}{e} \tag{2.45}$$

The change in work-function is computated as,

$$\Delta WF = WF_{ads} - (WF_{neu} - \Delta E_f) \tag{2.46}$$

WF_{ads} and WF_{neu} are the work functions of H-adsorbed and neutral electrodes, respectively. ΔE_F is the change in the Fermi-level when hydrogen atoms are introduced. The work function of any system is given by,

$$WF = E_{vac} - E_f \tag{2.47}$$

where E_{vac} and E_f are the electrostatic potential of the vacuum far from the electrode surface and the position of the Fermi-level of the electrode, respectively.

C_{EDL} calculation is rather straight forward,

$$C_{EDL} = \frac{\epsilon_0 \epsilon_r A}{d} \tag{2.48}$$

where ϵ_0, ϵ_r are the vacuum permittivity and dielectric constant of the electrolyte, respectively. 'A' is the electrode area, and 'd' is the width of the Helmholtz layer. For all calculations done in this thesis, ϵ_r is set at 6.0 and 'd' at 2.8 Å, the radius of hydronium ion.

Solvation method

This method considers a non-ideal Faradaic process to compute the electrostatic electrochemical double layer and redox charge transfer across the layer when a potential is applied to the MXene electrode in contact with an aqueous H_2SO_4 electrolyte. The reaction is given as,

$$M_{n+1}C_nO_2^q + 2H^+ \rightarrow M_{n+1}C_nO_{2-2x}(OH)_{2x}^{q'} + 2(1-x)H^+(aq) \tag{2.49}$$

where x is surface hydrogen coverage (between 0 and 1), and q is the net charge on the electrode. The applied electrode potential controls both q and x during the charging process. The free energy G(x, Φ) is computed as,

$$G(x,\Phi) = E(x) + xE_{ZPE} + Q(V(x,\Phi))\Phi + E_{EDL}(V(x,\Phi)) + (1-x)\mu_{H^+} \tag{2.50}$$

E(x) is the total energy of the solvated electrode with H-coverage x in zero surface charge. E_{ZPE} is the zero point energy difference of the electrode between no-H and full-H coverage. The term, $Q\Phi$, is the electrical work to move the charge Q (net charge on electrode) from zero potential (in the bulk electrolyte) to the electrode with the potential Φ. E_{EDL} is the energy of the induced EDL by the electrode charge Q. The last term is the chemical potential of the solvated proton in the electrolyte. V(x, Φ) is the relative potential with respect to PZC (Point of zero charge) at coverage x and electrode potential Φ,

$$V(x,\Phi) = \Phi - \Phi_{PZC}(x) \tag{2.51}$$

Once V(x, Φ) is known , the charge Q(x, Φ) and E_{EDL} can be obtained by,

$$Q(x,\Phi) = \int_{V=0}^{V=\Phi-\Phi_{PZC}} C_{EDL} dV \tag{2.52}$$

$$E_{EDL}(x,\Phi) = \int_{V=0}^{V=\Phi-\Phi_{PZC}} Q(x,\Phi) dV \tag{2.53}$$

The final term μ_{H^+} (proton's chemical potential) is given by,

$$\mu_{H^+} = \frac{1}{2}G[H_2] + e\Phi_{SHE} - 0.059 \times pH \tag{2.54}$$

where $G[H_2]$ is

$$G[H_2] = E[H_2] + ZPE[H_2] + \frac{7}{2}k_BT - TS_{H_2} \tag{2.55}$$

All physical quantities in the equation (2.55) are obtained from standard DFT calculations and standard thermodynamic databases. E(x) and Φ_{PZC} are obtained from the JDFT simulation. After knowing Φ_{PZC}, one can evaluate euqations (2.51)-(2.53). The quantities obtained using equations (2.51) - (2.55) along with E(x) constructs the free energy G(x, Φ) according equation (2.50). Once G(x, Φ) is known, partition function Z(Φ) can be written as,

$$Z(\Phi) = \int_{x=0}^{x=1} \exp(-\beta G(x, \Phi))dx \tag{2.56}$$

The average hydrogen coverage (x_{avg}) and surface charge (Q_{avg}) are then obtained by ensemble averaging.

$$x_{avg}(\Phi) = \frac{\int_{x=0}^{x=1} x\exp(-\beta G(x, \Phi))dx}{Z(\Phi)} \tag{2.57}$$

$$Q_{avg}(\Phi) = \frac{\int_{x=0}^{x=1} Q(x, \Phi)\exp(-\beta G(x, \Phi))dx}{Z(\Phi)} \tag{2.58}$$

The slope of x_{avg} and Q_{avg} vs. Φ give the value of C_{redox} and C_{EDL}, respectively.

Chapter 3

Capacitances of pristine and oxygen functionalized $M_{n+1}C_n$ (M= Ti, V, Nb, Mo) MXene supercapacitor electrodes

3.1 Introduction

Since its discovery in 2011, few MXenes have been investigated to assess their potentials as supercapacitor electrodes. Despite demonstrating their potential as supercapacitor electrodes, more needs to be done to understand the origin of supercapacitance in MXenes at the electronic level. Theoretically, efforts have been spent in understanding the pseudocapacitance in Ti_3C_2 only. Therefore, in this chapter we present a systematic investigation of various contributions to the total capacitances of six MXene compounds Ti_2C, V_2C, Nb_2C, Mo_2C, Ti_3C_2 and Nb_3C_2 using electronic structure based methods.
The reasons behind choosing these six are the following: (1) all the MXene compounds except Nb_3C_2 have been synthesized, and (2) whether the trends in their capacitative behavior can be traced back to the behavior of the d electrons of the transition metal constituents. This is the reason for selecting compounds with transition metal components from among both 3 d and 4 d elements in the periodic table. Although surface passivation is inevitable in the process of exfoliation from MAX to MXene and the surface passivation can significantly affect the material properties, several robust theoretical calculations have been performed on different MXenes, they idealized situations by considering pristine MXenes only. This risks missing out on critical physical effects due to surface passivation. Thus, in this work, we have considered both pristine and oxygen-functionalized systems. To our knowledge, no systematic and comprehensive study addressing the behavior of various components that make up the total capacitances in MXenes is available to date. Our calculations demonstrate that (1) all compounds considered have reasonable minimum values of the capacitances, (2) consideration of C_Q is essential to have a realistic estimate of the total capacitance, and (3) there is no notable trend about the d orbitals of the transition metal M. These results provide the crucial first step towards understanding the energy storage capacities and mechanisms behind them for different MXenes.

3.2 Computational Details

We applied the **'RBA method'**, discussed in section 2.5.2, to compute the charge storage capacities of the considered MXenes. We calculated the electronic structures of the MXenes by the DFT-based Projector Augmented Wave(PAW) method as implemented in the Vienna ab-initio Simulation Package(VASP). We used a kinetic energy cut-off of 500 eV and a Monkhorst-Pack grid of 12 × 12 × 1 k mesh for self-consistent calculations. A larger k-mesh 42 × 42 × 1 was used for the calculation of the electronic structure. A 3 × 3 × 1 supercell of MXene and 4 × 4 × 1 k-mesh

[0]The contents of this chapter are published in 2022 J. Phys. D: Appl .Phys. 55 085502

were used to apply the 'RBA Method'. The energy and force convergence criteria were set at 10^{-6} eV and 10^{-5} eV Å^{-1} for unitcell calculations and 10^{-6} eV and 0.05 eV Å^{-1} for super-cell ones.

3.3 Results and Discusssions

3.3.1 Structural parameters

Table 3.1: Lattice Parameter(a) and bondlength of carbon(C) atom - transition metal(d_{M-C}) and oxygen(O) atom - transition metal(d_{M-O}) in Å for Pristine ($M_{n+1}C_n$) and -O functional MXene ($M_{n+1}C_nO_2$)

System	a and d in Å						
	$M_{n+1}C_n$			$M_{n+1}C_nO_2$			
	a	d_{M_1-C}	d_{M_2-C}	a	d_{M_1-C}	d_{M_2-C}	d_{M-O}
Ti_2C	3.05	2.11	-	3.03	2.17	-	1.96
V_2C	2.92	2.06	-	2.90	2.00	-	1.96
Nb_2C	3.12	2.19	-	3.10	2.16	-	2.09
Mo_2C	2.93	2.11	-	2.87	2.15	-	2.06
Ti_3C_2	3.09	2.06	2.11	3.04	2.19	2.15	1.96
Nb_3C_2	3.12	2.13	2.26	3.14	2.19	2.23	2.09

To model the -O functional MXenes, we considered three possible surface passivation sites for oxygen atoms,(section 2.4). Total energy calculations suggest that the oxygen atoms prefer to occupy the hollow site of the transition metal atom, *i.e*, H site (Figure 2.2(a,b))for all the MXenes except Mo_2C. The hollow site of carbon atoms, *i.e*, C site is an energetically favorable site for oxygen atom in Mo_2CO_2. The optimized -O passivated structures of Ti_2C, V_2C, Nb_2C are shown in the Figure 2.2(a, b) and that of Mo_2C is shown in the Figure 2.2(c,d). In case of M_3C_2 systems, hollow sites corresponding to the inner transition metal layer (M_{in}, Figure 2.2) are energetically favorable ones for -O passivation. Figure 3.1(e,f) shows the top and side view of the M_3CO_2 (M= Ti, Nb) in their ground states. Table 3.1 shows the lattice parameter(a), the bond lengths between transition metals and carbon and oxygens for Pristine and -O functional MXenes. It is evident from Table 3.1 that the lattice parameter is reduced upon -O functionalization for all systems, except Nb_3C_2.

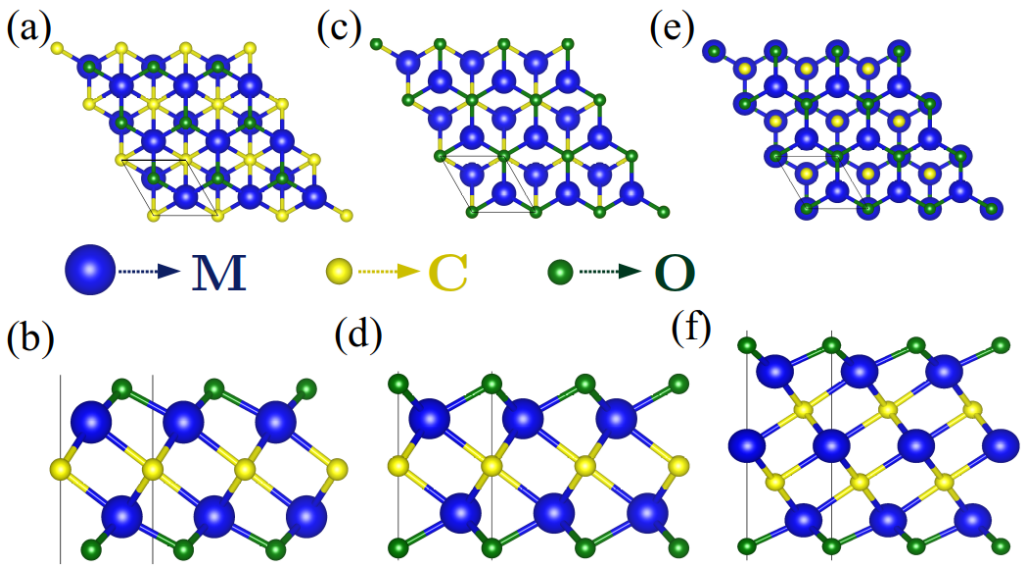

Figure 3.1: Top and side view of M_2CO_2 MXene(a,b) in HH (both -O occupy H sites) model, (c,d) in CC (both -O occupy C sites) model and (e,f) Top and side view of M_3CO_2 in HH (both -O occupy H sites) model.

3.3.2 Quantum Capacitance

Table 3.2: Total Charge Storage(Q^{int}) in C/g at ± 1.0 V for $M_{n+1}C_n$ and $M_{n+1}C_nO_2$ MXenes considered in this work.

System	Q^{int}(C/g)			
	$M_{n+1}C_n$		$M_{n+1}C_nO_2$	
	Voltage		Voltage	
	1 V	−1 V	1 V	1 V
Ti_2C	1713.76	1621.69	822.65	335.96
V_2C	1513.13	1758.58	2098.36	821.56
Nb_2C	985.68	1803.79	518.04	610.39
Mo_2C	1156.94	1677.14	348.61	1143.88
Ti_3C_2	2261.77	1636.57	844.60	575.78
Nb_3C_2	1450.72	1679.05	1514.15	684.81

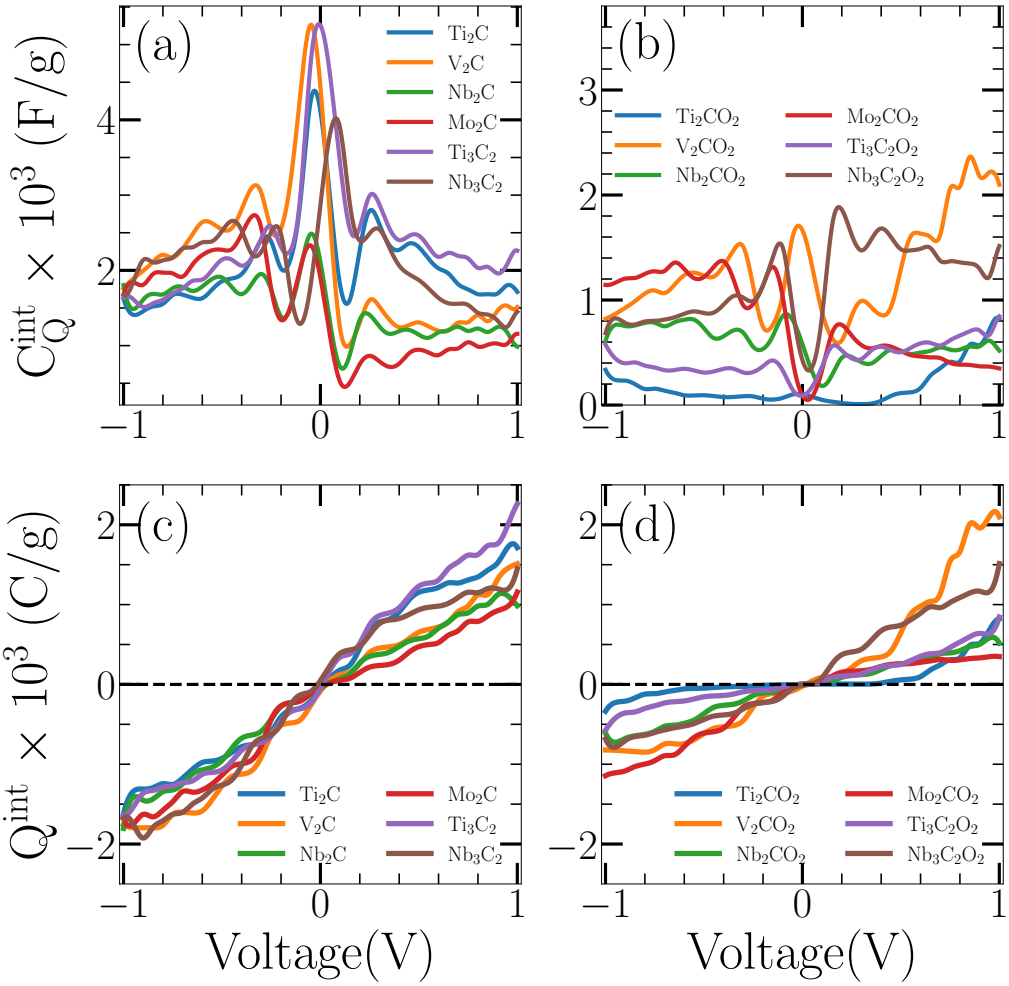

Figure 3.2: Variations in the Integrated Quantum Capacitance C_Q^{int} (in F/g)(top Panel), and total Charge Storage Q^{int} (in C/g)(bottom Panel) with Voltage for $M_{n+1}C_n$ and $M_{n+1}C_nO_2$ MXenes

In Figure 3.2(a),(b) we present the variations of Integrated Quantum Capacitance (C_Q^{int}) as a function of voltage. The range of voltages is selected to be ±1 Volt. The range is chosen to keep in mind that the electrochemical stability window of the electrolyte solvent is about 1.25 V at room temperature [117]. C_Q^{int} for pristine $M_{n+1}C_n$ systems exhibit a uniform behavior. Baring Mo_2C, all other systems have the maximum C_Q^{int} near 0 V at room temperature. As the voltage is

increased, C_Q^{int} decreases in a non-monotonic way with their minima around the maximum values of the voltages. Upon oxygen functionalization, the uniformity in the pattern is destroyed. However, the minimum C_Q^{int} are near 0 V. As a general trend, C_Q^{int} for functionalized MXenes are less by an order of magnitude in comparison with their pristine counterparts. These trends can be explained by the changes in the electronic structures near Fermi levels of the $M_{n+1}C_nO_2$ compounds to the $M_{n+1}C_n$ ones. In all the cases, the *p* states of oxygen lie deeper in the band, thus depleting the *d* states of M atoms near the Fermi levels. As an illustrative example, we show the total and partial densities of states for Ti_2C (Figure 3.3). Here, the impact of functionalizations is the starkest as it opens a semiconducting gap near the Fermi level. As a result, there is a significant overall reduction in C_Q^{int} in the voltage range considered.

In Figure 3.2(c),(d) and Table 3.2, we also depict the total charge stored (Q^{int}) as a function of voltage. As expected, the Q^{int} are maximum at the maximum voltages. Since it depends on the capacitance, by and large, functionalized MXenes can store charge an order of magnitude less than that can be stored by the pristine ones. The trends in Q^{int} vary irrespective of materials and voltage ranges. In pristine compounds, while Ti_2C and Ti_3C_2 can store more charge at positive voltages, the trend is different for others. In oxygen-functionalized compounds, it remains the same for these two. Nb_2CO_2 and Mo_2CO_2 too follow the same trends as found in their pristine counterparts. The trends for V_2CO_2 and $Nb_3C_2O_2$, however, follow a trend different than what was found in their pristine counterparts. After functionalization, V_2C and Nb_3C_2 show significant charge storage for positive voltages while Mo_2C has charge storage larger than the rest at negative voltages. This implies that the former two will perform better as positive electrodes while the Mo_2C has better potential as a negative electrode, even after surface passivation.

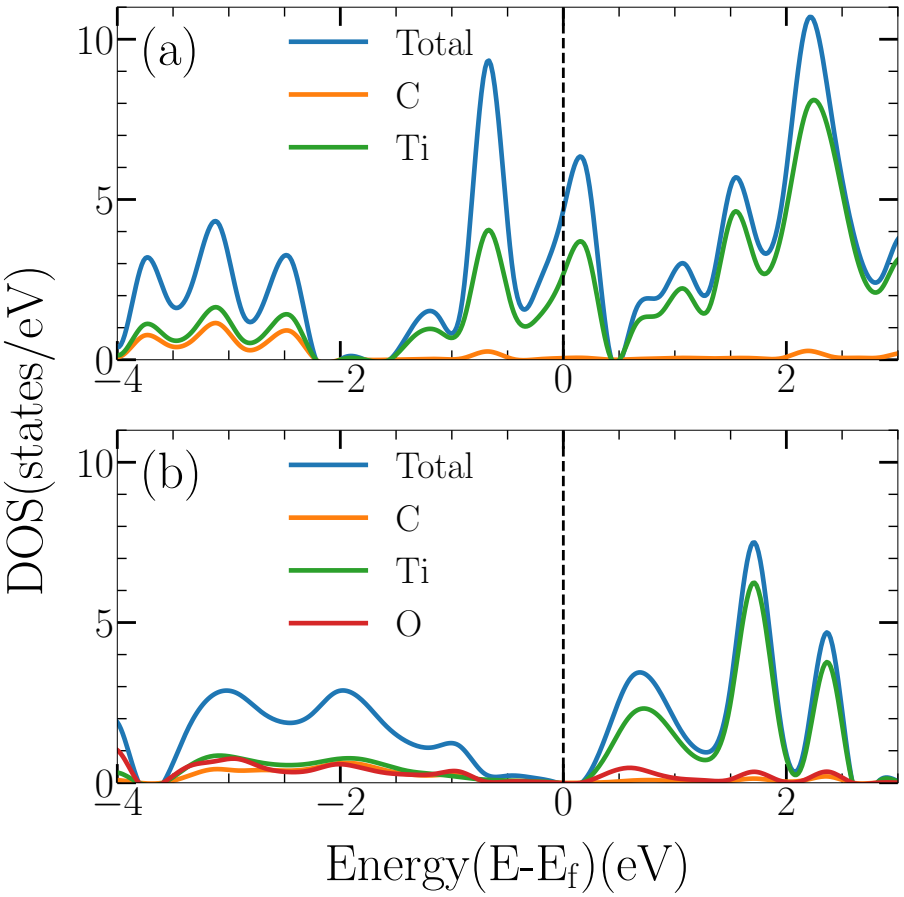

Figure 3.3: Partial and total Densities Of States(DOS) of Ti_2C (Top) and Ti_2CO_2(Bottom)

3.3.3 Pseudo-Capacitance & EDLC

To calculate the electrochemical performance of the MXenes, we applied the **RBA Method** as discussed in section 2.5.2. Pseudocapacitance C_{redox} of the pristine and Oxygen functionalized

Table 3.3: Average Charge Transfer(ΔQ)(e), Fermi-Shift(ΔE_f)(eV), Change in Work-Function(ΔWF)(eV) and Work-Function(WF)(eV) for Pristine and Oxygen Functionalized MXenes. All results are for 100% H adsorped system.

System	$M_{n+1}C_n$				$M_{n+1}C_nO_2$			
	Avg ΔQ	ΔE_f	ΔWF	WF	Avg ΔQ	ΔE_f	ΔWF	WF
Ti_2C	1.622	0.67	0.693	4.072	0.499	1.20	2.565	1.976
V_2C	1.536	0.70	1.836	4.961	0.479	0.515	3.770	2.168
Nb_2C	1.580	0.84	0.56	4.225	0.479	1.21	2.079	2.387
Mo_2C	1.478	0.95	0.561	4.604	0.506	2.11	2.805	2.421
Ti_3C_2	1.614	0.53	0.518	4.065	0.463	1.12	2.680	2.013
Nb_3C_2	1.589	0.74	0.411	4.294	0.480	0.715	2.600	2.121

MXene electrodes are calculated by considering them negatively charged; the electrolyte between the plates is such that H^+ ions will be adsorbed on their surfaces. The continuous adsorption of H^+ on the electrode surfaces would lead to faradaic charge transfer and give rise to C_{redox}. Since the charge transfer and the work function both are supposed to vary with change in the surface coverage with H^+, it would be interesting first to inspect the impact on C_{redox}. The trends in variations of C_{redox} with H-coverage for Pristine and Oxygen functionalized MXenes are shown in Figure 3.4. Following two important trends emerge from the results: first, like C_Q^{int}, C_{redox} of pristine MXenes are one order of magnitude higher than those of oxygen functionalized MXenes, and second, C_{redox} keeps on varying significantly as H-coverage changes that is as the voltage changes (the addition of each H^+ is equivalent to a change in the voltage). Although the variations are extremely wiggly, particularly in the case of pristine MXenes, we find that in cases of oxygen functionalized MXenes, $C_{redox}^{minimum-charged} < C_{redox}^{full-charged}$ in general (here, $C_{redox}^{minimum-charged}$ and $C_{redox}^{full-charged}$ stand for minimum H-coverage and 100% H-coverage respectively) whereas $C_{redox}^{minimum-charged} > C_{redox}^{full-charged}$ in case of pristine compounds. Such opposing trends emerge from the trends in the charge transfer ΔQ and the changes in work function ΔWF as the H-coverage increases. While for both pristine and functionalized MXenes, $\Delta WF^{minimum-charged} < \Delta WF^{full-charged}$, $\Delta Q^{minimum-charged} > (<) \Delta Q^{full-charged}$ for pristine (functionalized) compounds. The only exception to this general trend is Ti_2C. For the MXenes, following the general trends, the changes in the work function have been larger than in the charge transfer, making the work function the primary deciding factor in the variations of the C_{redox}.

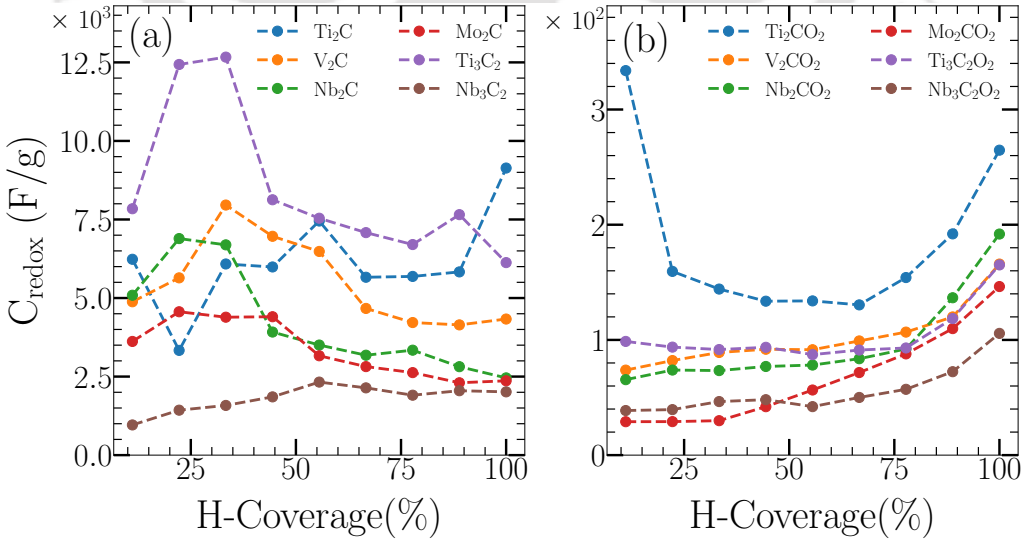

Figure 3.4: Variation in Pseudo-Capacitance(C_{redox}) with H-coverage for $M_{n+1}C_n$ (left) and $M_{n+1}C_nO_2$ (right) MXenes.

In Figure 3.5(b), we show C_{redox} for all the MXenes considered here, both in their pristine and oxygen-functionalized forms. The C_{redox} values given are the ones for calculations with full H-coverage of the surfaces. This makes sense as the full H-coverage results are equivalent to the

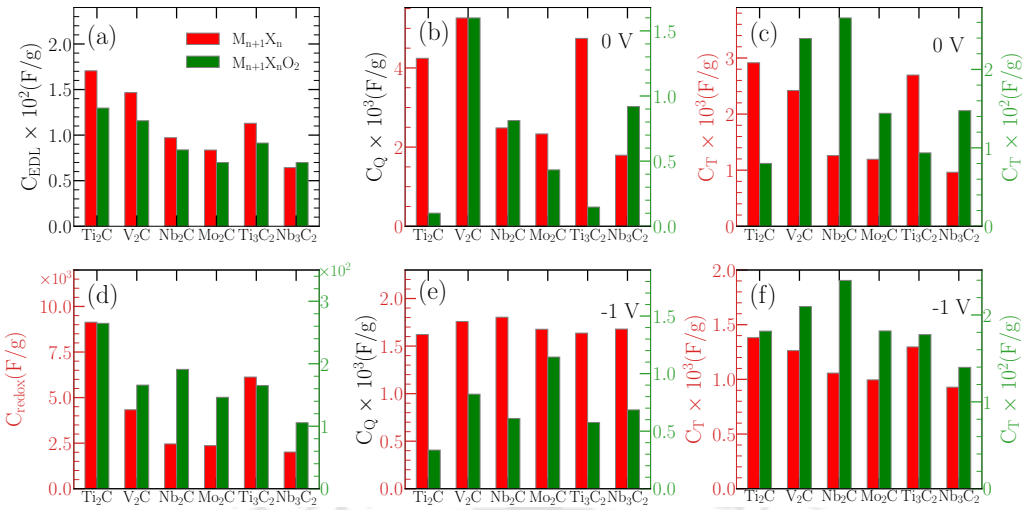

Figure 3.5: (a) C_{EDL}, (b) C_{redox}, (c) and (d) C_Q at ~ 0 V and at ~ -1 V, respectively, (e) and (f) C_T at ~ 0 V and ~ -1 V, respectively of $M_{n+1}C_n$ and $M_{n+1}C_nO_2$ MXenes.The red and green curves represent $M_{n+1}C_n$ and $M_{n+1}C_nO_2$ MXenes respectively. C_{redox}, C_Q and C_T plots each have two different y-ranges as marked.

condition when the plates are fully charged. We find the following trends: first, the functionalized MXenes have C_{redox} values one order of magnitude less than the pristine ones; second, C_{redox} of 211 MXenes (n=1) considered here are greater than those of 321 MXenes (n=2). To understand these trends, we first look at the trends in various quantities that make up the expression of C_{redox} (Equation refer Credox eqn) given in Table 3.3.
Before analysing the results given in Figure 3.5 and Table 3.3,it is worth mentioning that the following are found:

1. In case of neutral electrodes (no H-coverage), $WF^{functionalized}_{neutral} > WF^{pristine}_{neutral}$. Our calculations got this trend [118] right. Our calculated values of $WF^{functionalized}_{neutral}$ - $WF^{pristine}_{neutral}$ are also in good agreement with the results in Ref [118]. Thus, functionalization increases the Work function of the electrodes when they are neutral.

2. WF does not vary appreciably between neutral pristine and fully charged pristine while it drops by about 3 eV in the case of functionalized Ti_3C_2. The trend is similar for other MXenes. This implies that charging affects the functionalized MXenes significantly. Since a functionalized charged electrode is closer to reality than a pristine neutral one, this result is to be considered one of the important ones and needs to be understood.

For fully charged electrodes (Table 3.3), we find that across the compounds considered here,

1. $\Delta E_f^{pristine} < \Delta E_f^{functionalized}$, the difference is not too big though.

2. $WF^{pristine} > WF^{functionalized}$, the difference is about 2.0 eV.

3. $\Delta Q^{pristine} > \Delta Q^{functionalized}$ while $\Delta WF^{pristine} < \Delta WF^{functionalized}$.

4. $\Delta Q^{pristine}$ on an average is about $1.5e$ across compounds while $\Delta Q^{functionalized}$ on an average is $0.5e$. $\Delta WF^{pristine}$ is 0.5 eV while $\Delta WF^{functionalized}$ is 2.5 eV on an average.

The trends described above imply that both charged condition and functionalization affect the charge transfer and the changes in the Work function substantially. Therefore, an explanation of the drastic reduction of C_{redox} upon functionalization would require an understanding of changes in both quantities.

In the case of pristine compounds, ΔQ is larger as the hydrogen gets electrons from transition metal M directly, while in the case of functionalized one, hydrogen makes covalent bonds with oxygen and thus shares electrons. The interaction is no longer with the transition metal but through Oxygen. Presumably, Oxygen, being more electronegative, gains electrons from the M layers. Thus, an excess of negative charge is created on the outer layer of the surface. Oxygen

shares this charge with hydrogen. Hydrogen being more electropositive than Oxygen, the net charge transfer between hydrogen and functionalized substrate is much less.

It is a well-known fact that the work function of a surface increases when the surface adsorbate is more electronegative. This is perfectly consistent with our calculations if we look at the work functions of the neutral electrodes. This also means that the charging brings significant changes to reverse this trend. The question is why.

The large $\Delta WF^{functionalized}$ indicates that there is a significant change in surface dipole moment [118, 119]. This change in surface dipole depends on i) re-distribution of electronic charge between surface and adsorbate, ii) dipole moment of the adsorbates, iii) change in dipole moment due to surface relaxation, and iv) shift in Fermi level. In our case, more than the Fermi level shift, it is the other factors that must be dominant as differences between $\Delta E_f^{pristine}$ and $\Delta E_f^{functionalized}$ are not appreciable. The charge transfer, too, changes by only $0.07e$ from a neutral Ti_3C_2 to a neutral $Ti_3C_2O_2$,for example. However, there is a possibility of a significant charge re-distribution at the surface when an electrode is charged. There will be a dipole contribution from OH covalent bonds. It has already been established that the internal dipole moment of the OH functional group is appreciable and can significantly impact the WF of MXenes [118]. Finally, there can be a contribution due to appreciable surface relaxation due to charging in the case of functionalized MXenes. All these factors explain the trends in C_{redox} found in our calculations.

Electrochemical double-layer capacitance (C_{EDL}) can have a significant contribution to total capacitance. C_{EDL} is calculated using Equation (refer EDL eqn) and presented in Figure 3.5(a). In pristine compounds, C_{EDL} are orders of magnitude smaller than the other contributors to the total capacitance. Upon functionalization, the other two components reduce by orders of magnitude, and thus, the contributions of C_{EDL} would add up significantly to the overall capacitances.

3.3.4 Total capacitance C_T and comparison with experiments

In Figure 3.5(e) and (f), the total capacitance C_T for all $M_{n+1}C_n$ and $M_{n+1}C_nO_2$ compounds are presented. We have reported C_T values at two different voltage regions: near 0 V and the maximum, that is, -1 V. The reason behind choosing these two is the following: C_Q, a quantity often not taken into consideration, is dependent on the voltage directly. C_Q is significant as it can reduce the C_T substantially unless it is orders of magnitudes higher than the electrical part C_E of the total capacitance. In our case, while calculating C_{redox}, we modeled the systems as negative electrodes. Therefore, -1V is considered as the maximum voltage. Since the extrema in C_Q, in all cases, are close to 0 and -1 V as discussed in section 3.3.2, we have considered those values of C_Q only. This way, our results set the upper and lower bounds on the C_T.

A one-to-one correspondence between the experimental results and our computations is not possible. The electrochemical performance of a supercapacitor is experimentally obtained from the capacitance versus voltage curves (cyclic voltammograms). However, the capacitance values crucially depend on the electrolyte used and the voltage scan rates. Despite this, a rough comparison between our calculations and the available experimental results can be made. Here, we compare our results with the available experimental ones by considering the experimental results that yield maximum values of the capacitances in an electrolyte providing hydrogenic ions for a negative electrode. We find that our result for $Ti_3C_2O_2$ agrees reasonably with the experimental value of 246 F/g obtained at a scan rate of 2 mV/s in a 1 M H_2SO_4 [18]. In the case of Mo_2CO_2, our result is in excellent agreement with the experimental value of 196 F/g obtained at a scan rate of 2 mV/s in a 1 M H_2SO_4 [23]. The experimental value of 51 F/g in Ti_2CO_2 obtained at a scan rate of 5 mV/s in a KOH solution [120] too is in fair agreement with the minimum C_T reported by us. In the case of V_2C, the degree of agreement between the experiments and our calculations varied depending upon the electrolyte used in the experiment. The maximum capacitances obtained in experiments were 164 F/g [121],184 F/g, 225 F/g, and 487 F/g [78] in Na_2SO_4, KOH, $MgSO_4$ and H_2SO_4 solutions. Our calculated result is closer to the first three experimental values.

3.4 Conclusions

MXenes are a new class of low-dimensional materials with tremendous potential as supercapacitors. Although several MXenes have been synthesized and their electrochemical characteristics studied recently, to our knowledge, there needs to be systematic investigations into their capacitances by analysis of the various contributions from different sources. This work is the first in that direction

where the understanding of their capacitative behaviors is done from the electronic structures. The good agreement between our results and the experimental ones for the systems where experiments have been done demonstrates the correctness of our approach and that the models used closely mimic the experimental situations. Important aspects like the quantum capacitances and their variations with voltages, the impact of charging the electrodes, and the surface passivation have been discussed in detail. The results also establish the following: first, the results of pristine and oxygen-functionalized ones provide the limiting values of the total capacitance. Pristine compounds that exhibit an order of magnitude larger values of the capacitances are idealized systems, while fully surface passivated ones are the other extremes. In an experiment, the surface may not be fully functionalized or a mixture of functional groups. Thus, the truth, in all likelihood, will be in between the two extremes. Therefore, all the compounds considered here will display excellent capacitative behavior in reality if they are used as negative electrodes; second, although the transition metal constituents in the compounds considered are chosen from both $3d$ and $4d$ series, there is hardly any noticeable difference or a trend in their relative behaviors as far as the capacitances are considered; third, we find $Nb_{n+1}C_n$ as another potential negative electrode that can be used in a supercapacitor. Its C_T value, close to the other compounds, should attract the experimentalists to assess its electrochemical performance.

The 'RBA method' gives the variations in the capacitances with hydrogen coverage. It is unable to provide any information regarding electrode potential. In reality, experiments are reported with a capacitance profile in a chosen electrode potential window. The capacitance behavior changes significantly with the voltage window. It would be helpful to experimentalists if any theoretical approach could provide a capacitance profile with varying electrode potential and hydrogen coverages. Keeping this fact in mind, in the next chapter, we used a different approach to gain insight into the electrochemical performance of considered systems. The next chapter does a comparative study on the effects of doping and substitution on the storage capacity of $Ti_3C_2T_x$.

Chapter 4

Effects of doping and substitution on the electrochemical properties of MXene supercapacitor electrodes: case study with $Ti_3C_2T_x$

4.1 Introduction

Doping and substitution with heteroatoms is a proven effective tool to improve the physical properties of materials. The electrochemical performances of several 2D electrode materials like graphene [122], boron nitride [123], and molybdenum disulfide [124] could be significantly improved by manipulating their electron transport processes through doping. Significant enhancement in the capacitance was observed for nitrogen-doped Graphene[125, 126, 127, 128]. Very recently, electrochemical performances of nitrogen-doped Ti_3C_2 MXenes were investigated [129, 130]. In Ref [129], capacitance improvement by 460% was obtained at a low concentration of doped nitrogen. It degraded upon an increase in the nitrogen concentration. This significant increase was attributed to contributions from both EDL and redox mechanisms. A combination of DFT calculations and experimental measurements were reported in Ref [130]. They examined the influence of site occupancy of the dopant on the capacitance and inferred that nitrogen doping, in general, increases the value of the capacitance, although the gain was not as substantial as reported in Ref [129]. Their results indicated that the EDL mechanism dominates nitrogen substitution at the carbon site, while the redox mechanism prevails for doping at functional or surface sites. DFT calculations for Ti_3CN monolayer [131]that is a 50% substitution of nitrogen at carbon lattice site suggested that nitrogen substitution may lead to a significant increase in the charge storage capacity contributed mainly due to surface redox reaction.

In the investigations on the electrochemical performances of nitrogen-doped and substituted functionalized Ti_3C_2 done so far, understanding of the origin of the supercapacitative behavior is done only qualitatively, often in an indirect way. Direct computation of various contributions to the total capacitance providing robust ground to the qualitative understanding still needs to be improved. In this chapter, we look into this unexplored area for both doped and substituted Ti_3C_2 using DFT in conjunction with thermodynamic solvation models for an accurate description of the electrochemical phenomena at the surface of the electrode in an aqueous solution. Since a realistic MXene system has different functional groups attached while performing a theoretical treatment, they are to be incorporated into the modeling. In general, it is the -O and -OH groups that are present in higher proportions, activating the redox mechanism for charge storage in $Ti_3C_2T_x$ MXenes; T stands for functional groups, x denotes the percentages of them [132, 133, 134]. Taking this clue from experiments, here, we have worked with $Ti_3C_2T_x$ where T_x implies mixed functionalization, that is, our system evolves through states from $Ti_3C_2O_2$ to $Ti_3C_2(OH)_2$. We have systematically investigated the effects of doping nitrogen at three possible sites in functionalized Ti_3C_2 ($Ti_3C_2T_x$) by computations of the different contributions to the total capacitance. We also

[0]The contents of this chapter are published in 2022 J. Electrochem. Soc. 169 090525

investigated effects of substitution at other sites in $Ti_3C_2T_x$ by substitution of 50% C with N atom and 66% Mo at the outer Ti layer giving rise to Ti_3CNT_x and $Mo_2TiC_2T_x$ systems, respectively. The reason behind the choice of such specific substitution is that ordered structures for these two systems have already been synthesized [135, 136]. However, electrochemical measurements on them are yet to be done. This systematic exploration yields a substantial understanding of the impacts of doping and substitution at different sites on the supercapacitive properties of $Ti_3C_2T_x$.

4.2 Computational Details

In this chapter, we used Joint Density Functional Theory(JDFT) based **'Solvation method'** discussed in section 2.5.2 to compute the electrochemical storage performance of doped and substituted $Ti_3C_2O_2$. An implicit solvation model as implemented in the simulation package JDFTx[137] to obtain the electronic structure and the potential at the PZC of each H coverage for calculation of the free energy function is used. Φ_{SHE}, is taken to be the computational standard hydrogen electrode. It has been determined to be 4.66 V from PZC calibration of the CANDLE solvation model in JDFTx[110]. The Generalised Gradient Approximation with the Perdew-Burke-Enzerhof functional (GGA-PBE)[138] was considered to approximate electron exchange-correlation for the DFT calculations. Ultrasoft pseudopotentials[139] were used to describe the ion-electron interaction. Kinetic energy cut-off of 20 Hartree and 30 Hartree were used for structure optimization and single point energy calculation at the optimized geometry with convergence criteria of 10^{-6} Hartree. To model doped and substituted $Ti_3C_2O_2$, we have considered a $3 \times 3 \times 1$ supercell of $Ti_3C_2O_2$ unit cell.

4.3 Results and Discussions

4.3.1 Structural models and properties

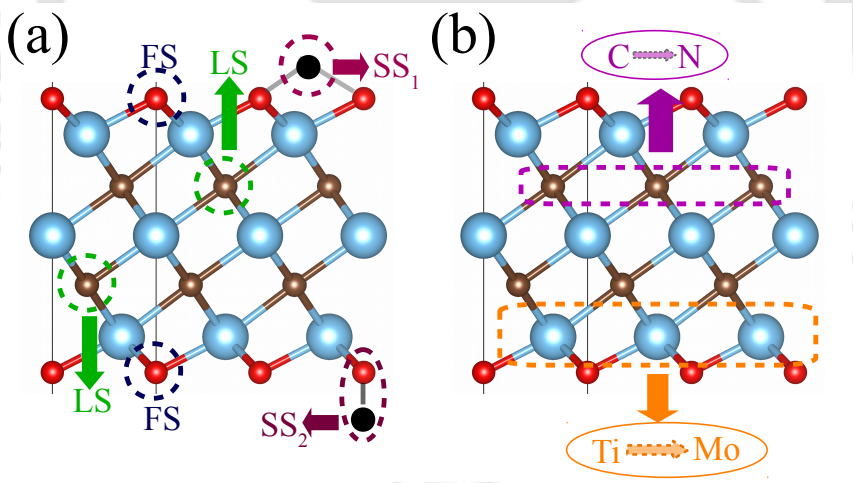

Figure 4.1: Possible sites of (a)N doping, (b) N or Mo substitution for $Ti_3C_2T_x$

In order to model N-doped and substituted $Ti_3C_2T_x$ MXenes, we start with optimized structure of $Ti_3C_2O_2$. In chapter 3, we observed that oxygen atoms energetically prefer to sit at the 'H' site of Ti_3C_2 to form -O functional MXene. The final structure is shown in Figure 3.1(e,f). Ti_3CNO_2 and $Mo_2TiC_2O_2$ are modeled by replacing 50% of carbon layer (of $Ti_3C_2O_2$) by nitrogen and by replacing the outer Ti layers (of $Ti_3C_2O_2$)by Mo, respectively as shown in the Figure 4.1(b). Modeling the nitrogen-doped $Ti_3C_2O_2$ is, however, different. It is because nitrogen atoms can occupy three possible positions when doped into $Ti_3C_2O_2$ MXene. Accordingly, three structural models can be constructed: Lattice-Site(LS) model, Functional-Site(FS) model, and Surface-Site(SS) model. The doped nitrogen replaces carbon and Oxygen atoms in LS and FS models, respectively, shown in Figure 4.1(a). In the SS model, they do not replace any atoms but position themselves on the surface of the MXene. They can occupy either the positions on top of the functional atoms (SS_2 of Figure 4.1(a))or the positions between the functional and Ti atom in the outer layers(SS_2

of Figure 4.1(a)). The SS model with an N atom on top of the O atom(SS_2) is unstable, whereas the model with an N atom at the midpoint of Ti and O atom(SS_1) is stable. In this work we have considered 10% nitrogen doping in $Ti_3C_2O_2$. Doped and substituted $Ti_3C_2T_x$ systems are then obtained by continuous addition of H atoms to both surfaces of the systems. All systems are optimized for each x, the H-coverage. The lattice parameters increase linearly with x for all systems. The lattice parameters of all the systems at x=0 and x=1 are given in Table 4.1. The results are in excellent agreement with the experimental ones [130]. The SS model is not considered as calculations in Reference [130] showed it to be dynamically unstable.

Table 4.1: Optimised lattice parameters of pristine and nitrogen doped $Ti_3C_2T_x$, Ti_3CNT_x and $Mo_2TiC_2T_x$ (T=O,OH) for x = 0 and x = 1 in Å

System	Lattice-parameter	
	x = 0	x = 1
$Ti_3C_2T_x$	3.03	3.08
LS-$Ti_3C_2T_x$	3.01	3.07
FS-$Ti_3C_2T_x$	3.04	3.10
Ti_3CNT_x	3.02	3.08
$Mo_2TiC_2T_x$	2.93	2.97

We find that the lattice contracts upon doping at the lattice site and expands upon doping at the functional site. This trend in the lattice parameters is consistent with the size of the atoms. The atomic radius of Oxygen, Carbon, and Nitrogen are 60pm, 70pm, and 65pm, respectively. The changes in the lattice parameters upon doping are consistent with this. The length of the Ti-C bond expands(contracts) in the FS(2.26Å)(LS(2.12Å)) model in comparison to that in the pristine(2.19Å) system. A reverse trend is shown in the case of Ti-T_x bond lengths, although the changes, in this case, are almost negligible. The Ti-N bond length changes substantially between the two models. This is expected since different atoms are replaced in different models. The charge sharing between Ti and N will be more in the case of the FS model than the LS one. Overall, the trends in the lattice parameters follow the trends in the Ti-C bond lengths.

4.3.2 Electronic Structure and Quantum Capacitance

The quantum capacitance of an electrode material depends on its electronic structure near the Fermi level. In Figure 4.2(a)-(c), we present the electronic structure of pristine and nitrogen-

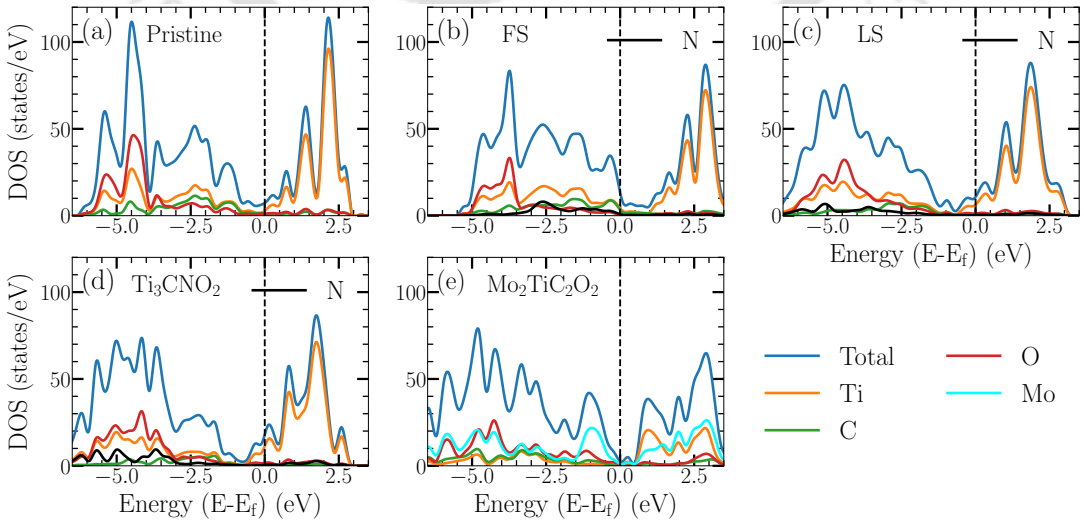

Figure 4.2: Electronic Structure of (a) Pristine, (b) FS-doped, (c) LS-doped $Ti_3C_2O_2$ and (d) Ti_3CNO_2 and (e) $Mo_2TiC_2O_2$

doped (both FS and LS) $Ti_3C_2O_2$. The nitrogen atom has one more valence electron than carbon and one less electron than oxygen. Therefore, when a nitrogen atom replaces a carbon(oxygen)

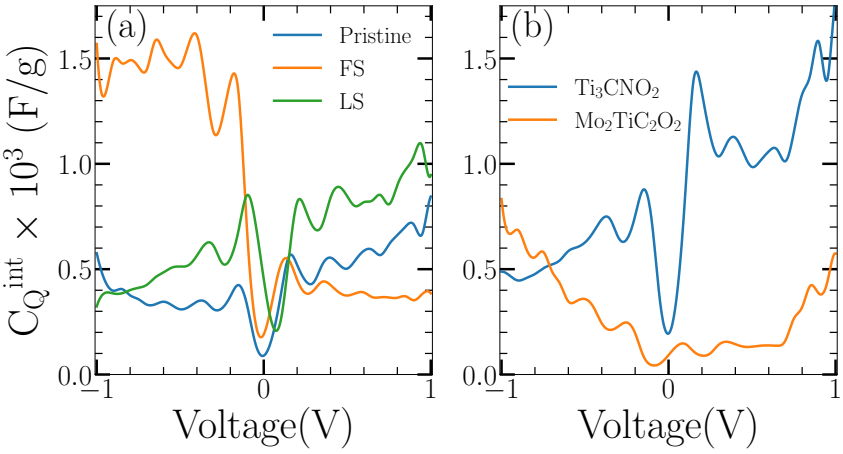

Figure 4.3: Integrated Quantum Capacitance of (a) Pristine and doped $Ti_3C_2O_2$, (b) Ti_3CNO_2 and $Mo_2TiC_2O_2$

atom, the total number of electrons in the system increases (reduces). As a consequence, the electronic bands around the Fermi levels are shifted. We find that in the case of doping at the functional site (Figure 4.2(b)), the electronic band shifts towards higher energies. This happens due to the reduced number of electrons in the system. In the case of doping at the lattice site, the shift of the electronic bands is towards lower energies(Figure 4.2(c)). This is due to an increase in the total number of electrons in the system. Close inspection of the densities of states reveals the following features: (a) the electronic structure near the Fermi level is most substantially affected in case of doping at the functional site. This is mostly due to the nitrogen p states occupying higher energy levels in the valence band, (b) in case of doping at the lattice sites; the nitrogen p states are deep within the valence band, unable to impact the features near the Fermi level. The features near the Fermi level, in this case, are mostly due to the Ti d states, (c) the unoccupied part of the spectra is overwhelmingly due to Ti d-bands, which implies serious consequences on the charge transfer. From these, we can predict that it is more likely that the largest contribution to C_Q will come from the functional site-doped system. In Figure 4.3, we present the variation of Integrated Quantum capacitance(C_Q^{int}) with absolute voltage. The voltage range is set between ± 1 V. This range is chosen because, at room temperature, the electrochemical stability window of the electrolyte solvent is about 1.25 eV [117]. In the negative part of the voltage window, the maximum C_Q^{int}(Figure 4.3(a)) of FS-doped $Ti_3C_2O_2$ is four times larger than that of the pristine MXene. This comparative behavior correlates to the changes in the electronic structure near the Fermi level. As expected from the features in the electronic structure, C_Q^{int} of LS-doped system(Figure 4.3(a)), though higher than the pristine system throughout the voltage window, is not as amplified as the FS-doped system.

Figure 4.2(d) and (e) show electronic structures of Ti_3CNO_2 and $Mo_2TiC_2O_2$. A comparison between LS-doped $Ti_3C_2O_2$ and Ti_3CNO_2 can be instructive. One of the prominent features is that with more nitrogen replacing carbon, the bands move towards lower energy, in general. A consistent trend emerges as one makes a comparison between pristine, LS-doped, and carbon substituted $Ti_3C_2O_2$. In Ti_3CNO_2, states near the Fermi level are populated due to more contributions from nitrogen. The shoulder at around 3 eV in LS-doped $Ti_3C_2O_2$ transforms to a peak in Ti_3CNO_2. The small peak closest to the Fermi level in the unoccupied part of the LS-doped system transforms into a prominent one with nitrogen substitution. Upon substitution of Mo at Ti positions, however, the electronic structure changes considerably. The densities of states in $Mo_2TiC_2O_2$ are dominated by contributions from Mo and O near the Fermi level in the occupied part of the spectrum. In the unoccupied part, states near the Fermi level have dominant contributions from Ti and Mo. The bands are more extended in $Mo_2TiC_2O_2$ in comparison to $Ti_3C_2O_2$ as Mo being from the 4*d* series has wider bands. These features reflect in variations in C_Q^{int}. C_Q^{int} of Ti_3CNO_2 and $Mo_2TiC_2O_2$ are shown in Figure 4.3(b). For Ti_3CNO_2, the higher density of states in the conduction band around the Fermi-level leads to significantly larger C_Q^{int} on the positive side of the voltage window in comparison with that on the negative side. As expected from the features of the densities of states, $Mo_2TiC_2O_2$ has the lowest integrated quantum capacitance throughout the voltage window. With

variations in x, there is no change in the overall electronic structure profile of all the materials except a rigid shift of bands. Therefore, for any given x, the trends observed in case of x=0 ($Ti_3C_2O_2$) remain the same. However, the rigid shifts in the band structures lead to significant changes in the electronic structure near the Fermi levels. These changes in electronic structures around the Fermi levels get reflected in the Integrated Quantum Capacitance as x changes. A general trend in almost all cases is noticed: C_Q^{int} increases with x for both positive and negative voltages, the only notable exception being negative voltages in case of FS-doped $Ti_3C_2T_x$ where higher C_Q^{int} are obtained for x=0. One can understand such trends from the features in the densities of states as x varies. Equation (2.35) implies that a larger value of quantum capacitance will lead to a higher value of the total capacitance where the electrical part of the total capacitance will be the sole contributor. If both electrical and quantum parts of the capacitance are comparable, the total capacitance will be lesser than the least. In the next sub-sections, we explore this point.

4.3.3 Electrical capacitance

As discussed in Section 2.5.2, we have used the model of MXene electrode in contact with an acidic electrolyte H_2SO_4 for the calculation of the EDLC and Pseudocapacitances. We specifically looked at the effects of doping and substitution at different sites on the evolution of the electron and proton transfers between the electrolyte and the electrode, giving rise to simultaneous contributions of EDL and redox capacitances. Experiments on undoped $Ti_3C_2T_x$ have discussed possible mechanism behind elevated values of its capacitances [132, 133, 134]. It was found that the dominant mechanism depends on various factors such as multi-layer nature, the intercalation of alkali ions [132, 133], and the presence of water between the layers [134]. The literature on nitrogen-doped functionalized multi-layer Ti_3C_2 has proposed EDL as a primary mechanism behind the elevated value of the total capacitance due to nitrogen doping [129, 130]. On the other hand, analysis based solely on the electronic structures of functionalized Ti_3CN monolayers inferred that the primary mechanism for O functionalized system is the surface redox reaction while for F and (OH) functionalization, it is EDL [131]. One of our motivations, therefore, is to investigate this aspect, albeit in the case of monolayer systems.

Nitrogen Doped $Ti_3C_2T_x$

According to Equation (2.49), the surface redox behavior is controlled by the adsorption of a proton on the electrode surface and subsequent electron transfer to the electrode at a given electrode potential. To determine the extent of the surface redox phenomenon, we calculated G(x,Φ) (Equation 2.50) for each H-coverage, x, at different fixed electrode potentials (Φ); Φ varying from -1 V to +1 V with respect to SHE. In Figure 4.4 (a)-(c), we show G(x,Φ) as a function of x for pristine, nitrogen-doped FS and LS $Ti_3C_2T_x$, respectively. For all systems and all Φ, G(x, Φ) is parabolic in nature. From the minima of G(x, Φ), we find that the ensemble-averaged coverage x_{avg}= 0.63 , 0.93. 0.73 for pristine, functional-site and lattice-site doped $Ti_3C_2T_x$, respectively. The result for the pristine compound agrees very well with the existing one [88]. The results imply that the electrode surfaces are not fully protonated even at -1 V for all systems. However, nitrogen doping enhances protonation, with the FS system having more than 90% covered, the maximum among the three systems. Another common feature in all systems is that the x_{avg} continuously decreases with increasing Φ leading to x_{avg}=0 at Φ =1 V.

The electrochemical behavior of a capacitor in acidic electrolytes like H_2SO_4 can be understood in terms of the net charge on the surface, responsible for EDL, and the proton transfer from the electrolyte ions to the electrode that is responsible for the redox reaction. The net number of electron transfers or the total charge storage in the electrode is decided by the cumulative effect of these two. The electron transfer, surface charge, and proton transfer numbers as a function of Φ are shown in Figure 4.5 (a)-(c) for pristine, nitrogen-doped FS and LS systems. The proton transfer number is given by x_{avg} while the surface charge is the ensemble average of Q in Equation (2.52). The electrons transferred across the charge layer accumulated over the electrode surface are obtained by adding these two. For all three systems, accumulated surface charge prohibits proton transfer to the surface. For the LS-doped system, the variations in surface charge, proton transfer, and, consequently, the electron transfer numbers are linear with Φ. The surface, in all three cases, is slightly positively charged. This is because part of the positive charge from proton transfer becomes the net surface charge. In the case of the pristine and the FS-doped systems, the variations are piecewise linear with changes in slopes at intermediate voltages, the slopes

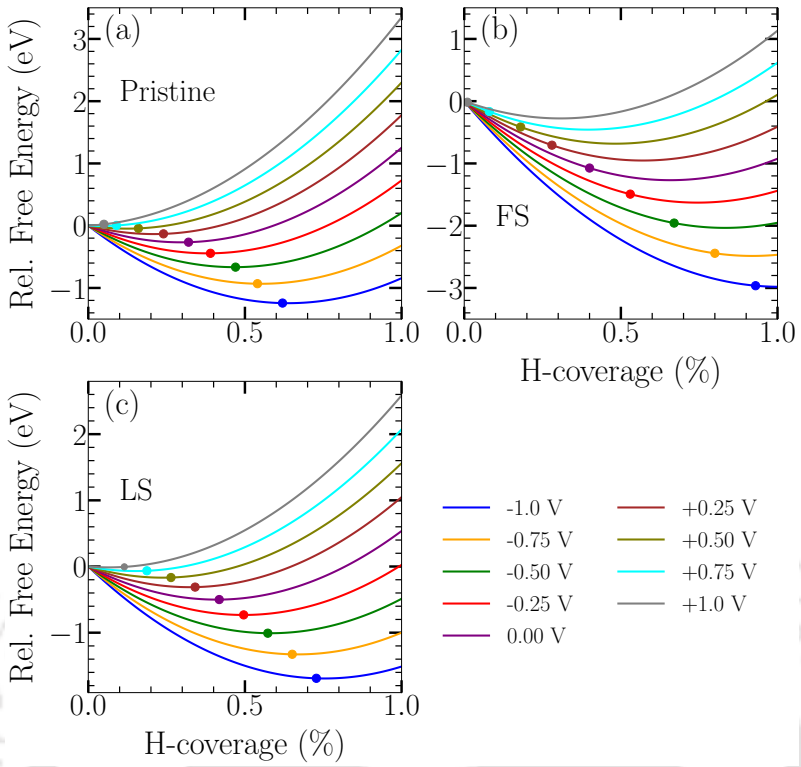

Figure 4.4: Variations in the Relative Free Energy with H-coverage at different fixed potentials for (a) Pristine, (b) FS, and (c) LS N-doped $Ti_3C_2T_x$.

being larger for the FS-doped system. The pseudocapacitance, the EDLC, and the total electrical capacitance are obtained from the slopes of proton transfer number, surface charge, and electron transfer number curves (Figure 4.5(a-c)), respectively. Figure 4.6 (a)-(c) shows variations in the capacitances for the three systems under consideration.

In the case of the pristine system, total electric capacitance is nearly constant at 250 F/g between -1 V and 0 V. It decreases linearly to 200 F/g for higher potentials. Both qualitative and quantitative agreements with the existing result [88] on the variation in the total capacitance with Φ are excellent. For the LS-doped system, the total capacitance is near constant at 250 F/g throughout the voltage range. This is because of the near-constant contributions from both EDLC and pseudocapacitance, which is due to the linear variations in proton transfer number and the surface charge. Therefore, nitrogen doping at the lattice site does not lead to any improvement in the electrical capacitance of $Ti_3C_2T_x$. The doping at the functional site, on the other hand, improves the total capacitance. This is due to the higher value of C_{redox} and lower value of C_{EDL} for this system. Since, in these cases, EDLC acts against pseudocapacitance, a lower value of C_{EDL} implies that the redox mechanism overwhelmingly determines the surface electrochemistry. In the case of the pristine and LS-doped $Ti_3C_2T_x$, the EDLC, both qualitatively and quantitatively, contributes substantially to the total electrical capacitance. In these two cases, though redox appears to be the dominating mechanism, the effect of EDL is recognizable. The dominance of redox reaction as found in our calculations, however, contrasts with the predictions made from the experimental results [129, 130]. A qualitative understanding of the larger value of redox capacitance for the FS-doped system compared to the LS-doped one can be understood from Bader charge analysis [140]. With full H-coverage, the average Bader charge transfer from the electrode to the H^+ ion is $0.463e$, $0.501e$, and $0.455e$ for pristine, FS-doped, and LS-doped systems, respectively. The largest charge transfer for the FS-doped system can explain the largest pseudocapacitance. The reason the FS-doped system has a larger charge transfer than the LS-doped one is the following: we find that the Ti-N bond length for the FS-doped system is 15% less than that in the LS-doped system. Ti-N and Ti-T_x bond lengths are comparable for FS-doped systems as doped nitrogen occupies the functional sites. Due to the significantly smaller Ti-N bond length, the charge sharing in the Ti-N bond is greater in the FS-doped system than in the LS-doped one. This, in turn, is responsible for a larger charge transfer to the H^+ ions, as can be seen quantitatively from the

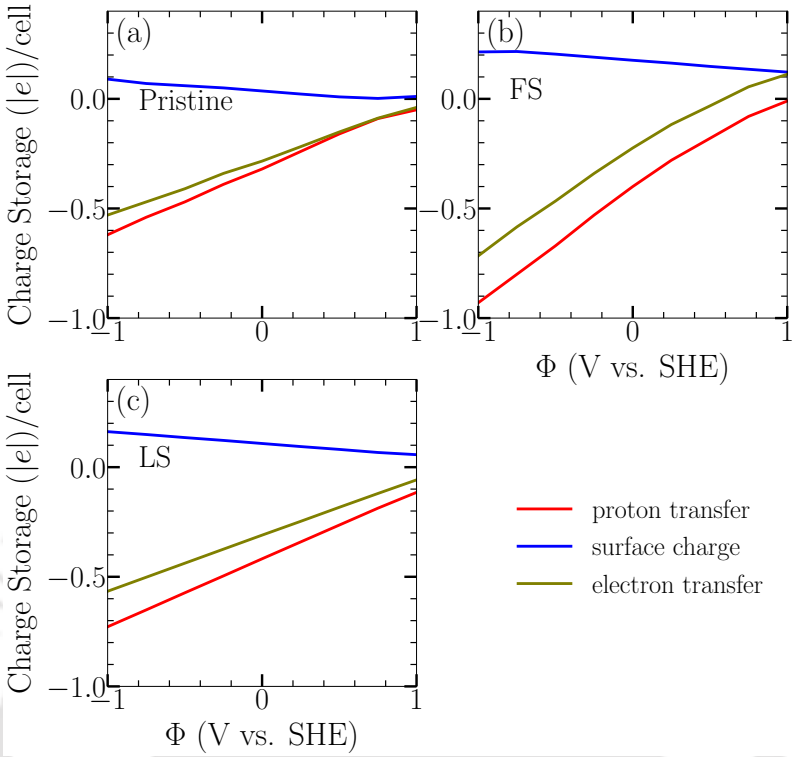

Figure 4.5: Charge storage with applied electrode potential (Φ) for (a) Pristine, (b) FS, and (c) LS N-doped $Ti_3C_2T_x$

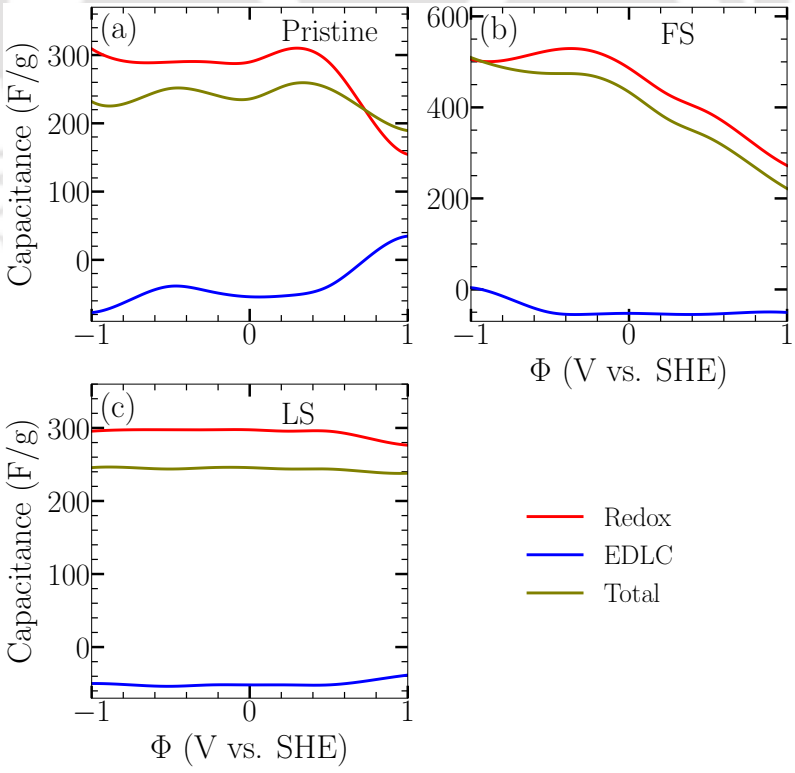

Figure 4.6: Electrical Capacitances with applied electrode potential (Φ) for (a) Pristine, (b) FS, and (c) LS N-doped $Ti_3C_2T_x$. The negative values of the EDL capacitances imply that the EDL mechanism is acting against the surface redox mechanism.

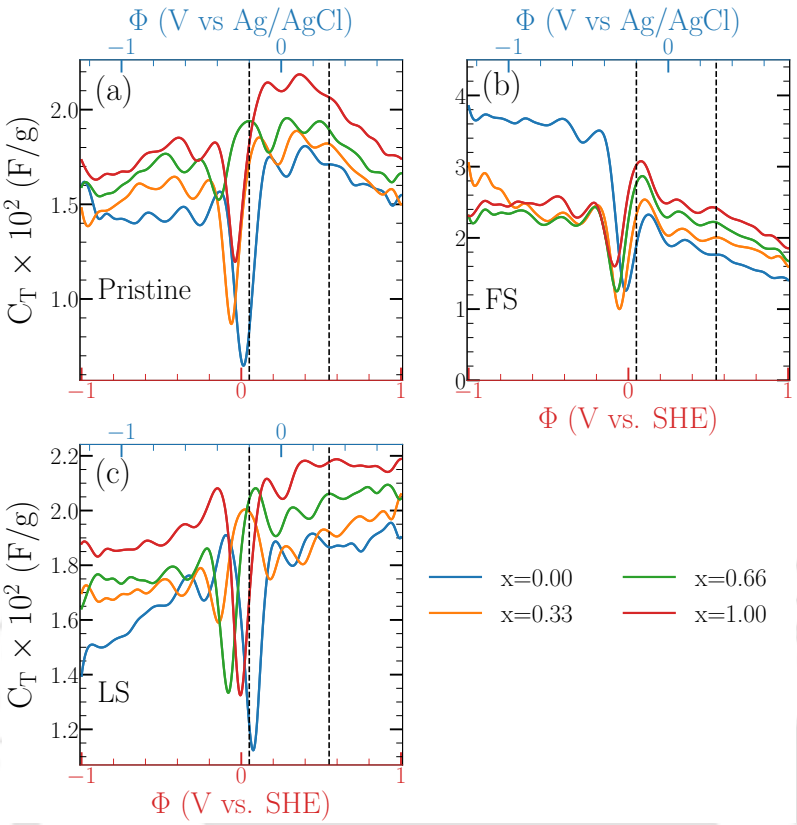

Figure 4.7: Total Capacitances with applied electrode potential (Φ) at different H-coverages(*i.e* x) for (a) Pristine, (b) FS, and (c) LS N-doped $Ti_3C_2T_x$

calculation of Bader charges on each atom.

Substituted $Ti_3C_2T_x$

The electrochemical behaviors of the substituted systems Ti_3CNT_x and $Mo_2TiC_2T_x$ throw up quite an interesting picture. Figure 4.8(a)-(b) show the G(x,Φ) as a function of H-coverage for Ti_3CNT_x and $Mo_2TiC_2T_x$, respectively. Unlike the doped systems, Ti_3CNT_x and $Mo_2TiC_2T_x$ have significantly low coverages, the highest x_{avg} being 0.35 and 0.31 respectively at -1 V. Behaviour of charge storages (Figure 4.9 (a)-(b)) too, are very different from the doped systems. The magnitude of the charges is less for substituted systems than the pristine and doped systems. However, the surface charge and protons do not act against each other. The lower amount of charge storage (compared to doped systems) and the negative sign of the surface charge (unlike the doped systems) can be correlated with the substantially low H-coverage. The qualitative and quantitative variations of various components in charge storage are reflected in the behavior of EDLC and pseudocapacitances (Figure 4.10(a)-(b). The non-linear variations of the proton and surface charges in Ti_3CNT_x determine the variations of the capacitances. While pseudocapacitance was the dominant contributor to negative voltages, EDLC started to play a significant role with increasing voltage, finally becoming the dominant one for positive voltages. Thus, in nitrogen substituted $Ti_3C_2T_x$, the mechanism of charge storage is dependent on the voltage window. Our quantitative calculations are in agreement with the quantitative analysis that Ti_3CNT_x cathode has surface redox reaction as the dominating mechanism [131].

The behavior of the components in electrical capacitance of $Mo_2TiC_2T_x$ is found to be different from all other systems. Here, the pseudocapacitance and EDLC do not oppose each other but collaborate. While pseudocapacitance turns out to be dominant, and both components remain near constant for most of the voltage window, beyond +0.5 V, EDLC assumes a more significant role. However, the absolute values are the least among the systems considered. This can be understood from the magnitudes of the charge storage, which in turn is connected to the lowest H-coverage and the fact that Mo, being 60% more electronegative than Ti, is unable to transfer as

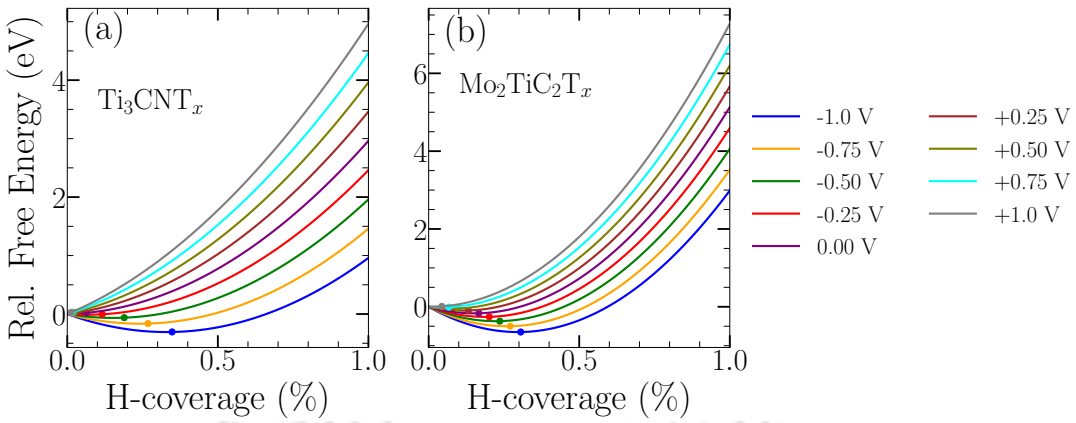

Figure 4.8: Variations in the Relative Free Energy with H-coverage at different fixed potentials for (a) Ti_3CNT_x (b)$Mo_2TiC_2T_x$

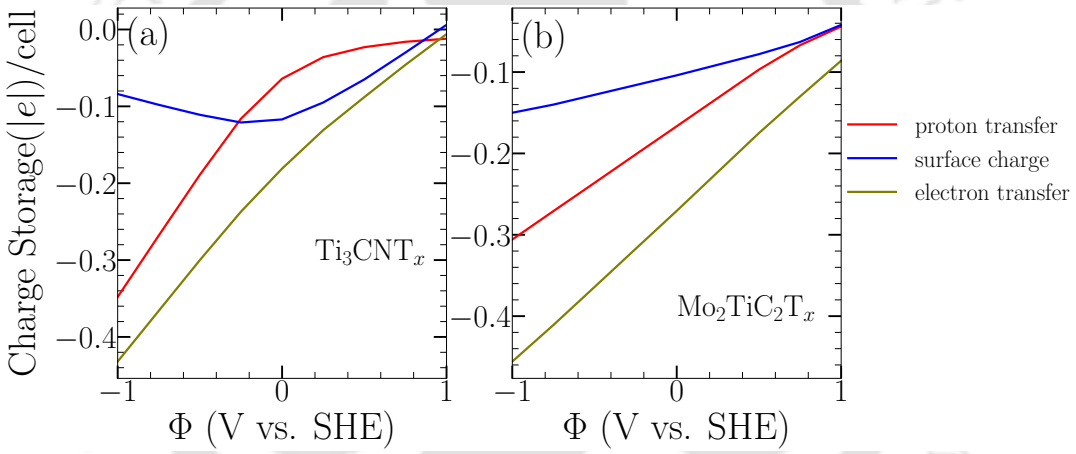

Figure 4.9: Charge storage with applied electrode potential (Φ) for (a) Ti_3CNT_x, (b) $Mo_2TiC_2T_x$

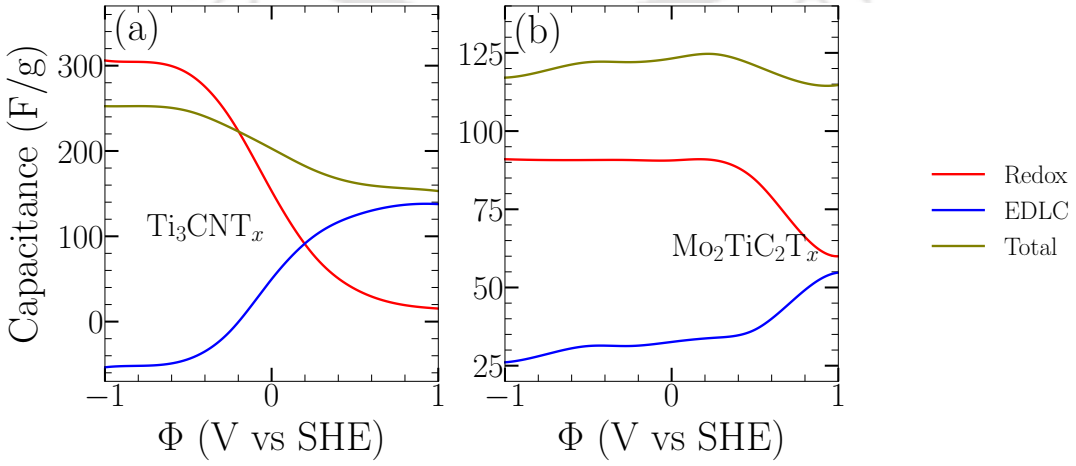

Figure 4.10: Electrical Capacitances with applied electrode potential (Φ) for (a) Ti_3CNT_x, (b) $Mo_2TiC_2T_x$. The negative values of the EDL capacitances imply that the EDL mechanism is acting against the surface redox mechanism.

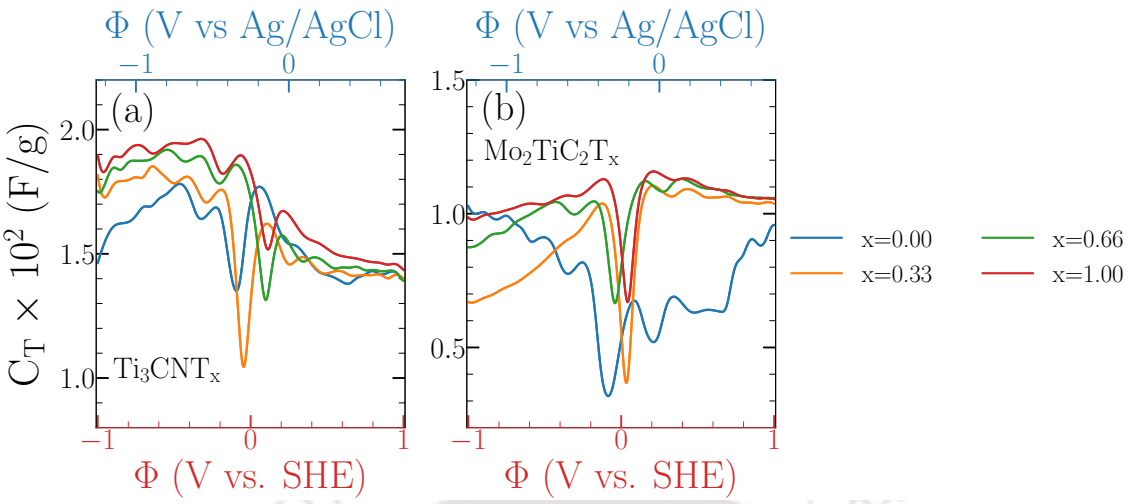

Figure 4.11: Total Capacitances with applied electrode potential (Φ) at different H-coverages(*i.e* x) for (a) Ti_3CNT_x, (b) $Mo_2TiC_2T_x$

much charge as Ti in the outer layers of the MXene.

4.3.4 Total Capacitance and comparison with experiments

Due to the dependence of C_Q^{int} on x, the total capacitance now depends on x. In Figures 4.7 (a)-(c) we show the total capacitance (calculated by Equation (2.35))of pristine and doped $Ti_3C_2T_x$. In Figures 4.11(a)-(b) results for Ti_3CNT_x and $Mo_2TiC_2T_x$ are shown. The variations in the capacitances (for different x values) are plotted with respect to SHE and Ag/AgCl electrode potentials. We find that by and large, the capacitance profiles for pristine and doped systems follow those of their quantum capacitances. This was expected as the orders of magnitude of C_E and C_Q are not too different for all systems except FS-doped one at negative electrode potentials. Consequently, we obtain high capacitances for FS-doped systems in the negative potential range. For the positive part of the SHE potential window, the capacitances of pristine, FS-doped, and LS-doped systems are comparable. A one-to-one comparison with the experimental results is difficult because of various factors. The capacitance crucially depends on the sample preparation method, the exact composition, the functional groups, and the electrolyte.
Moreover, in our computational model, the capacitance depends on the surface coverage, leading to a range of values for the total capacitance. Accordingly, our results contradict the ones obtained in Ref. [130], where the electrolyte is basic. The capacitances obtained in that work are significantly lower than our results. Also, they got the highest capacitance value for the LS-doped system and identified EDL as the primary mechanism, aided by the surface redox reactions due to the surface functional groups. On the other hand, some correspondences can be made with the experimental results of Ref. [129] as the electrolyte used was 1 M H_2SO_4, precisely the one used in the model implemented in our calculations. Although the maximum capacitance reported by them is only 32 F/g for the pristine system as opposed to values between 75-230 F/g in our estimates, there is a good agreement for the maximum capacitance of the nitrogen-doped system. The reported value of 192 F/g in the Ag/AgCl electrode potential window of -0.2-0.3 eV agrees well with the calculated values for FS (180-300 F/g) and LS (110-210 F/g) doped systems in the same window. However, there are specific qualitative differences between the results from the experiment and our calculations. From the high-resolution XPS study, it was suggested that the doped nitrogens occupy the carbon sites.
Therefore the capacitance reported in their work is that of an LS doped system. It is yet to be observed whether any further gain in capacitance can be obtained in an FS doped system in agreement with our results. The experiment also suggested that this gain in capacitance is due to a larger inter-layer distance due to doping leading to increased EDLC. Therefore, the primary mechanism in the doped system is EDL. Our calculations could not confirm it. In our estimates, the EDL part of the capacitance instead went the opposite way. However, it is worth mentioning that our calculations are on a monolayer implying infinite inter-layer distances. Moreover, no other

functional groups except -O and -OH were used in our model, while the experimental sample had -F functional groups in significant proportions. The presence of -F groups that are less redox active than -O and -OH in the experimental sample may explain the discrepancy between the experiment and theory in identifying the primary mechanism for charge storage. The total capacitance of the substituted systems is less than the doped systems. While the variation in the total capacitance of $Mo_2TiC_2T_x$ follows that of its quantum capacitance, the situation is different for Ti_3CNT_x. Though it had larger quantum capacitance for higher voltages (most significantly for x = 1), the drop in the electrical capacitance with increasing voltage brings the maximum total capacitance in the negative part of the SHE voltage window. These results show that the quantum capacitance is a vital component having a substantial influence on the quantitative estimation of capacitances of super- capacitors as observed earlier.

4.4 Conclusions

Using an implicit solvation model in conjunction with DFT, we have modeled the electrolyte electrode interaction at the electrode surface to compute the electrochemical parameters of doped and substituted oxygen functionalized Ti_3C_2 MXene. This model addresses the surface EDL and redox effects in H_2SO_4 electrolyte solution. We have computed the contributions to stored charges and the capacitances due to both effects when nitrogen is doped at different sites of $Ti_3C_2T_x$ as well as in substituted systems Ti_3CNT_x (nitrogen substitution at carbon site) and $Mo_2TiC_2T_x$ (molybdenum substitution at outer Ti layers). We find that upon inclusion of the quantum capacitance, the maximum gain in the capacitance is obtained for nitrogen-doped at functional sites of $Ti_3C_2T_x$ at negative SHE potentials. C_T can be as high as 380 Fg^{-1} for full H-coverage. This two-fold gain, compared to the pristine compound, is due to the larger charge storage dominated by the surface's redox activity. The presence of nitrogen dopants at the surface and the largest coverage of H^+ ions from the electrolyte are responsible for this. Our quantitative results suggest that the surface redox activity is primarily responsible for the electrochemical parameters for the pristine and doped systems, although the EDL mechanism competes with it. The two mechanisms act against each other and influence the capacitance's overall charge storage and electrical part. Our results agree with the experiment measurements. However, the qualitative explanation of increased capacitance value differs from ours. With the increase in nitrogen content such that it substitutes 50% carbon from the lattice site, the capacitance value degrades. It further degrades upon substituting the surface Ti atoms with more electronegative Mo. These are yet to be verified through electrochemical measurements, although both compounds have been synthesized. In substitution cases, though EDL and surface redox phenomena cooperate with each other, poorer charge transfer hinders the growth of capacitances. In the case of nitrogen substitution, we found the evolution of the EDL mechanism to become the dominant one upon the increase in voltage. The reverse trend compared to doped systems can be correlated with meager ion coverage from the electrolyte and subdued charge transfer on the surface due to more electronegative substituents. Our results suggest that nitrogen doping is a better strategy for better electrochemical performances in $Ti_3C_2T_x$ MXene electrodes. We also suggest that much better values of capacitances in nitrogen-doped $Ti_3C_2T_x$ can be obtained if samples are prepared with doping at the functional site, and electrochemical measurements are done in a larger negative voltage window with Ag/AgCl as reference electrodes. Here, the theory and experiments are compared for SHE and Ag/AgCl reference electrodes. However, this does not mean the calculations depend on the reference electrode's choice. The choice of other electrodes as the reference will only shift the voltage window, thus affecting the maximum and minimum values of the capacitances. To our knowledge, this work is the first of its kind where a systematic investigation of the effects of doping and substitution on the electrochemical property of the most extensively researched MXene Ti_3C_2 is done by computing different components of capacitances and providing insights from a microscopic point of view. This approach may pave the way for understanding the supercapacitative behavior in other MXenes. There are many scopes for an investigation into this class of materials.

One emerging class of two-dimensional material is **Janus** material. Janus is a unique two-dimensional structure where two elements of the same class span the two surfaces of a single-layer 2D material. The first synthesized Janus is MoSSe, a transition metal di-chalcogenides, where S and Se span the two surfaces. Experiments and theory suggest replacing one element from one surface with another same class element is an excellent surface engineering to improve a target property. We also attempted something like that with MXenes. In the next chapter, we present

results on the study of electrochemical properties of Janus MXene electrodes in contact with an acidic electrolyte.

Chapter 5

Improvement in charge storage capacities of supercapacitor electrodes by surface engineering: the case of Janus MXene

5.1 Introduction

One way to explore structure-property relations in 2D materials is to design compounds with asymmetric surfaces and study their impact on physical properties. To this end, quasi 2D Janus materials MoSSe[141] and WSSe[142] from the transition-metal dichalcogenide family have been synthesized. Experiments discovered that these compounds exhibit photo-voltaic properties[143], superior catalytic activity for hydrogen evolution reaction (HER) [144],vertical piezoelectricity[145], and Rashba effect[146, 147, 148, 149], among other novel features. These are the effects of the structural modifications of the pristine dichalcogenides. For example, the superior HER efficiency of MoSSe over MoS_2 is due to the presence of single S and Se vacancies that strengthen the binding of hydrogen with dichalcogenide monolayers, turning the inert surfaces highly active catalytically[144]. As a charge storage device, Janus MoSSe has shown greater potential, too. Monolayer MoSSe can simultaneously possess good storage ability and fast Na/K ion diffusion and thus can be used as an anode material for Na/K-ion batteries observed in DFT calculations[150]. First principles calculations on MoSSe monolayer and bi-layer have shown that they can be used as anodes in Li-ion batteries, too, as the charge asymmetry on the two surfaces induces an internal electric dipole moment that generates an intrinsic electric field from the Se layer towards S layer facilitating higher storage of Li ions [151]. Janus monolayer TiSSe and VSSe dichalcogenides, too, were predicted to be good anode materials for alkali ion metal batteries as computed by first-principles methods [152].

Though no Janus MXene has been synthesized, a plethora of First principles based simulations are available [153, 154, 155] that establish the thermal and mechanical stability of both $MM'XT_2$ and M_2XTT' compounds up to significantly high temperatures. (M, M′ (T, T′)) are two different transition metal constituents (functional groups). Calculations predict improved (over their end point constituents M_2XT_2) thermoelectric properties[156], HER activity [157], charge storage capacity in Li and Mg batteries [95], and magnetic properties [154] for a number of them. However, no investigation of the capabilities of Janus MXenes as electrodes in supercapacitors has yet been done. In this chapter, using the Joint Density Functional Theory based solvation method (section 2.5.2), we have investigated the charge storage capacities in two different groups of Janus MXenes $MM'CO_2$; in one group M,M′ are Ti,V, and Nb while in the other group, they are V, Cr, and Mn. M_2CT_2 MXenes as well as solid solutions $(M,M')_2CT_2$ (M,M′ are Ti,V,Nb) and MAX phases $(M,M')_2AC$ with M,M′ being V,Cr,Mn, have been synthesized [25, 84]. These indicate that there is a substantial possibility of the formation of Janus phases with these constituents. Without experimental reports, we have performed a detailed study on the chances of forming Janus MXenes by computing their thermal and mechanical stabilities. Our calculations show that of the six -O functionalized Janus compounds considered, only three are mechanically and thermally stable. The

electrochemical properties of these three in an acidic electrolyte solution are then computed and compared with the results on end point MXenes. Better performance due to this surface engineering is observed in all three cases, suggesting this as a possible route to enhance charge storage in MXene electrodes for supercapacitor applications.

5.2 Structural Model of functionalized Janus MXenes

Monolayer of Janus MXene MM′C is obtained from monolayers of M_2C pristine MXenes by replacing transition metal M atoms of one of the two surfaces with another transition metal M′. The structure of MM′C MXene is shown in Figure 5.1. During the synthesis process, MXene surfaces are passivated by functional groups T; the most common are -F, -O, and -OH. In this work, we have considered Janus MXenes with surfaces passivated by -O. In Figure 5.1, we show different positions available to -O for a given surface : (1) site T, the position right over the transition metal; (2) site H, the hollow site of a carbon atom and (3) site C, the hollow position corresponding to the transition metal element on the other surface (Figure 5.1(a)). Two asymmetric surfaces and three possible sites result in 3^2,*i.e*, nine models for a MM′CO_2 Janus MXene. We first compute the total energies of all nine structures to obtain the ground state. We then check the dynamical and thermal stability of the ground state structure by computing the phonon spectra and performing *Ab initio* molecular dynamics (AIMD) simulations.

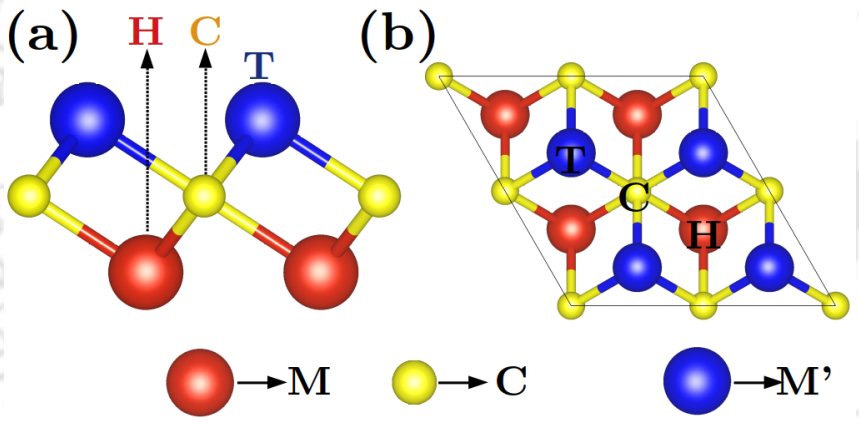

Figure 5.1: (a) Side view and (b) Top view of MM′C Janus MXene structure. Yellow, Red, and Blue balls represent the C, M, and M' elements, respectively.

5.2.1 Computational Details

The total energies and the electronic structures are calculated by the DFT-based projector augmented wave method[158] as implemented in Vienna ab-initio Simulation Package(VASP)[159]. The exchange-correlation part of the Hamiltonian is described by Perdew-Burke-Ernzehof (PBE) Generalized Gradient Approximation (GGA)[138, 160]. We use a kinetic energy cut-off of 520 eV and a Monkhrost-pack[161] grid of 12×12×1 for self-consistent calculations. A larger k-mesh of 24×24×1 is used for the Densities of States calculations. The convergence criteria for energy and force criteria were set to 10^{-6} eV and 10^{-5} eV/Å, respectively. The second-order interatomic force constants(IFCs) are calculated by the density functional perturbation theory (DFPT)[162] method implemented in VASP using a 3×3×1 supercell and 6×6×1 k-mesh. The phonon spectra are generated using these IFCs by the finite-difference method as implemented in the PHONOPY [163] package. *Ab initio* molecular dynamics (AIMD) simulations are performed with 3×3×1 supercell at 300K with Nose-Hoover thermostat[164, 165] as implemented in VASP for 10 ps with a time step of 2 fs.

For Joint Density Functional Theory calculation, Generalised Gradient Approximation with the Perdew-Burke-Enzerhof functional (GGA-PBE)[138] is considered as an approximation to exchange-correlation part of the Hamiltonian. Ultrasoft pseudopotentials[139] are used to describe the ion-electron interaction. Kinetic energy cut-off of 20 Hartree and 30 Hartree are used for structure

Table 5.1: Total energy of the Janus MXenes MM′C for different models according to sites of O occupancy.

System	Total Energy (eV) for -O occupancy sites			
	CC	HH	CH	HC
$TiNbCO_2$	0.57	0.09	0.00	0.59
$NbVCO_2$	0.03	0.00	0.26	0.13
$VTiCO_2$	-	0.00	-	0.16
$CrMnCO_2$	0.00	0.57	0.33	0.25
$CrVCO_2$	0.04	0.44	0.00	-
$MnVCO_2$	0.03	0.32	0.00	-

optimization and single point energy calculation at the optimized geometry with convergence criteria of 10^{-6} Hartree. For all calculations, 3×3×1 supercells of the unit cells are considered.

5.3 Results and Discussions

5.3.1 Structural stability and parameters

As mentioned in section 5.1, we have worked with six different -O functionalized Janus MXenes: TiNbC, VTiC, NbVC, CrMnC, MnVC, and CrVC. As a first step towards investigating their structural stability, we have performed total energy calculations for each of the nine models discussed in section 5.2. Out of the nine possible combinations of the two O atoms, ones involving the position 'T' (Figure 5.1(a) and (b)) deform the structures completely. Therefore, those possibilities are discarded. The total energies for the other four models are shown in Table 5.1 for each one of the compounds. For each system, the model with minimum energy is considered as the reference to scale energies in other models. We find that while both O atoms occupying H sites minimize the energy for $NbVCO_2$ and $VTiCO_2$, in the case of $CrMnCO_2$, both O minimize the total energy by occupying C positions. For the other three compounds $TiNbCO_2$, $CrVCO_2$ and $MnVCO_2$, the O atom associated with the surfaces of Ti(Nb),Cr(V) and Mn(V) occupies C(H) positions to minimize total energies. It is to be noted that the structures of $VTiCO_2$ in CC, CH models and those of $CrVCO_2$ and $MnVCO_2$ in HC models distort. Those models are, therefore, discarded from further consideration. In the next step, we perform phonon calculations on all the remaining configurations where the structures are undistorted. We find that only three systems, $NbVCO_2$, $CrMnCO_2$ and $MnVCO_2$ are dynamically stable (Figure 5.2). While $CrMnCO_2$ and $MnVCO_2$ are dynamically stable in their respective ground states (Table 5.1), dynamical stability in $NbVCO_2$ is obtained in the CC model, which is energetically only about 5 meV per atom higher than the ground state. The phonon spectra presented in Figure 5.2(a) are, therefore, calculated with the CC model. Since the energy of the CC model is very close to that of the ground state, forming this phase at low temperatures is possible, and thus, assessment of the dynamical stability of $NbVCO_2$ by considering this configuration is justified. The phonon spectra of the dynamically unstable configurations are shown in Figures (5.3)-(5.4). The dynamically stable structures of the three functionalized Janus MXenes are shown in Figure 5.5(a)-(c). We further assess the stability of these three compounds against thermal excitations by performing AIMD at room temperature. The results are shown in Figure 5.6(a)-(c). The variations in the Free energies and the temperatures over the observation time imply that the structures are stable. The final structures shown in the insets of the figures confirm that they are stable against thermal excitations.

In Table 5.2, information on ground states and structural parameters for the three Janus MXenes are shown. The information of the end point MXenes M_2CO_2 and M'_2CO_2 are also shown for comparison. Due to magnetic constituents Mn and Cr in $MnVCO_2$ and $CrMnCO_2$, additional magnetic calculations were done for these systems to ascertain the ground state. We find that though O atoms stabilize Mn_2CO_2 by occupying 'H' positions, in both $MnVCO_2$ and $CrMnCO_2$, the O atoms associated with the Mn surfaces prefer to occupy 'C' positions. The O atoms on V and Cr surfaces in Janus compounds, however, occupy the same positions as those in the end point compounds V_2CO_2 and Cr_2CO_2. In the case of $NbVCO_2$, the structure is stabilized when O atoms occupy 'C' positions on both surfaces, although both end point compounds have 'H' as the preferred position of O atoms. Thus, in $MnVCO_2$, the passivation on two surfaces leads to different

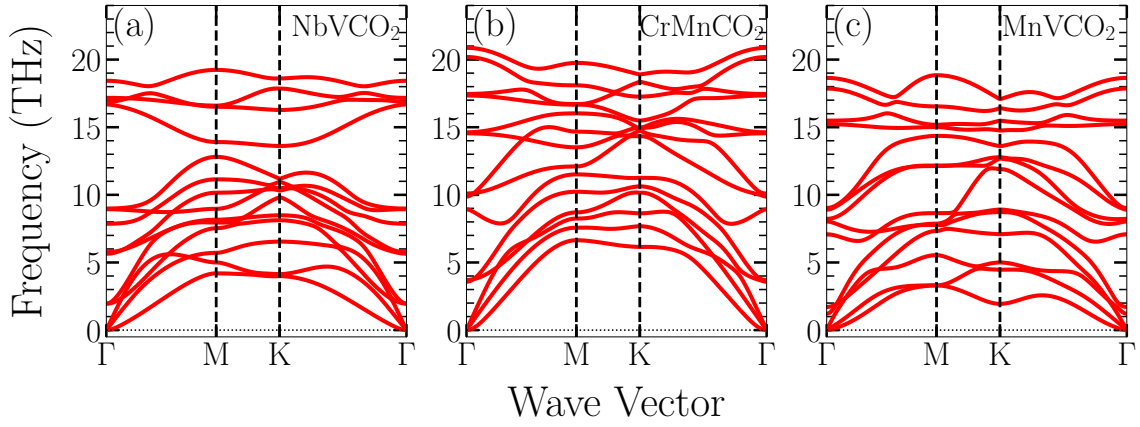

Figure 5.2: Phonon spectra of (a)$NbVCO_2$, (b)$CrMnCO_2$ and (c) $MnVCO_2$. Calculations are done with models CH for $CrMnCO_2$ and $MnVCO_2$. Model CC is used to compute phonon spectra of $NbVCO_2$.

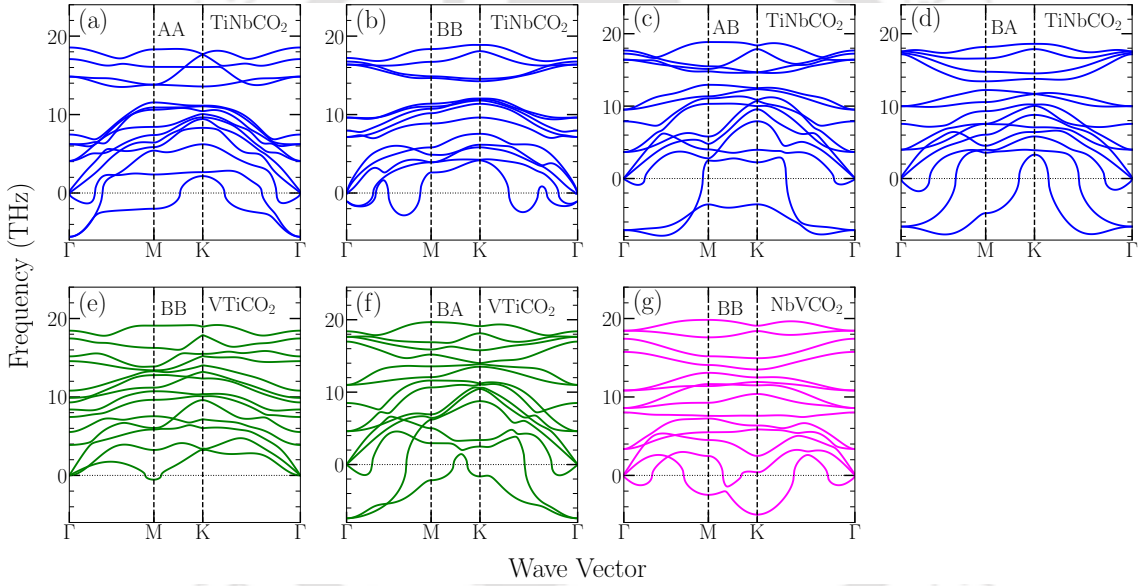

Figure 5.3: Phonon spectra of $TiNbCO_2$ in (a) CC, (b)HH, (c)CH, (d)HC model; $VTiCO_2$ in (e)HH, (f)HC model; $NbVCO_2$ in (g)HH model

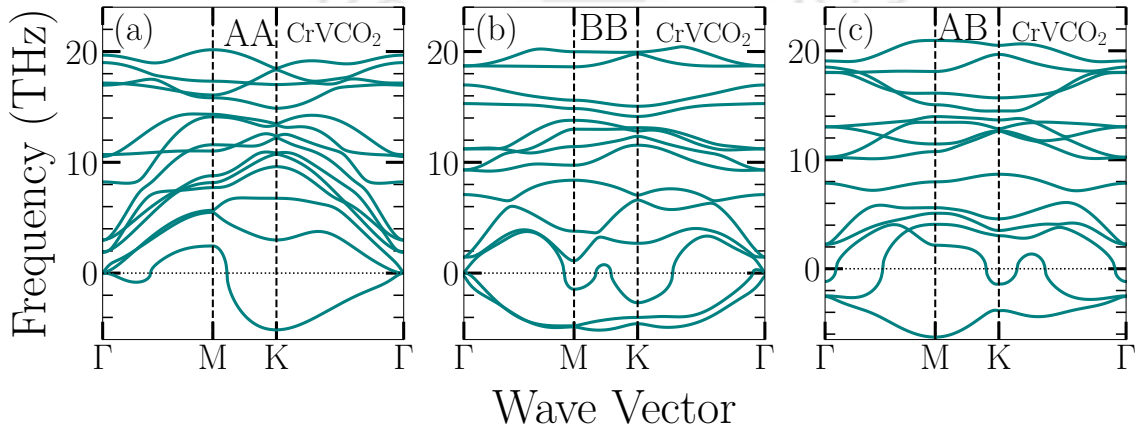

Figure 5.4: Phonon spectra of $CrVCO_2$ in (a)CC, (b)HH and (c)HC model

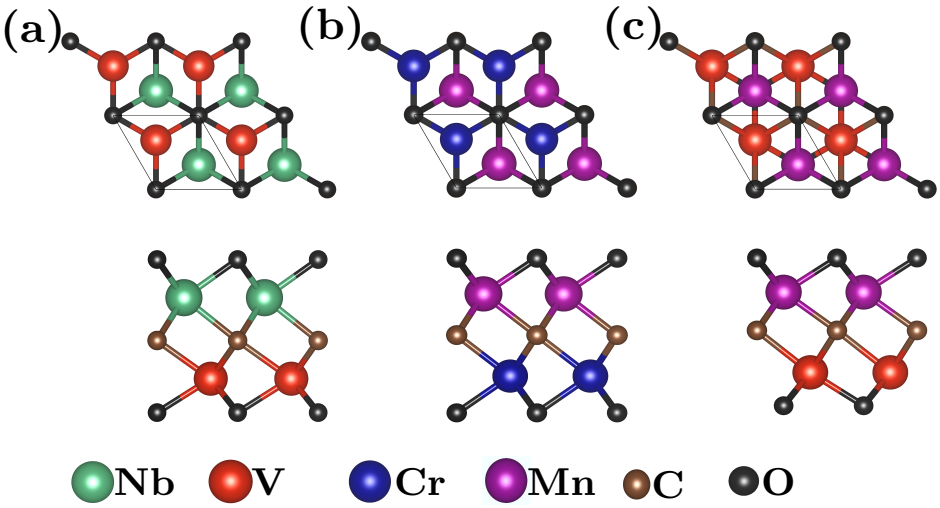

Figure 5.5: Dynamically stable lowest energy structures of (a)$NbVCO_2$, (b)$CrMnCO_2$, and (c)$MnVCO_2$. Both top (upper row) and side (lower row) views are shown.

symmetry. While the functionalization on the Mn surface gives rise to trigonal prismatic symmetry, that on the V surface leads to octahedral symmetry. For the other two Janus compounds, the symmetry is trigonal prismatic, irrespective of the surface passivation. The magnetic ground state in $MnVCO_2$ is ferromagnetic (FM), different from the antiferromagnetic (AFM) ground state in Mn_2CO_2. The electronic ground state, too, is different in $MnVCO_2$ as compared to Mn_2CO_2. The semiconducting ground state of Mn_2CO_2 transforms to a metallic one when $MnVCO_2$ Janus is formed. In the case of $CrMnCO_2$ Janus, too, the electronic ground state is metallic, the same as that of Cr_2CO_2. However, unlike the non-magnetic ground state of Cr_2CO_2, we get an AFM ground state in $CrMnCO_2$. The points to note are that although the electronic ground states in both $MnVCO_2$ and $CrMnCO_2$ are the same as the end compound MXenes V_2CO_2 and Cr_2CO_2, the magnetism driven by the inclusion of Mn in one of the surfaces lead to different ground states. In $CrMnCO_2$, the magnetic ground state of Mn_2CO_2 is retained but in $MnVCO_2$, it changes as well. It appears that while the properties of V and Cr surfaces are driving the electronic ground states, the passivation on different surfaces leading to different crystal symmetries in $MnVCO_2$ is responsible for the magnetic ground state of this compound being different from that of Mn_2CO_2. In both Mn-based Janus, the Mn moments are nearly equal and are substantially reduced from that in Mn_2CO_2. This is expected as the Mn-Mn inter-layer exchange interactions are absent in Janus compounds. In the case of $NbVCO_2$, both surfaces are passivated by O atoms that conform to the same symmetry. The Janus system is metallic and non-magnetic like their end compound MXenes Nb_2CO_2 and V_2CO_2. The lattice constants of $CrMnCO_2$, $MnVCO_2$ and $NbVCO_2$ Janus compounds are almost same as that of Cr_2CO_2, Mn_2CO_2 and V_2CO_2 MXenes, respectively. In $CrMnCO_2$ and $MnVCO_2$, Mn-C and Mn-O bond lengths decrease around 2-2.5 % in comparison to those in Mn_2CO_2. The Cr-C bonds in $CrMnCO_2$ shorten by 1% only with respect to Cr_2CO_2. On the other hand V-C bond lengths in $MnVCO_2$ increase by 1% while V-O bonds shorten by 2.5% in comparison to V_2CO_2.The Mn-C bond lengths in this compound decrease by 2% compared to Mn_2CO_2. The relative changes (with respect to quantities in the end point MXenes) of M-C, M′-C, M-O, and M′-O bond lengths are more significant in $NbVCO_2$ Janus. While there is hardly any change in Nb-C and Nb-O bonds, V-O bonds increase by 3% as compared to that in V_2CO_2. We can infer that overall, there are no significant changes in the structural parameters when Janus MXene is constructed out of regular MXenes.

5.3.2 Electrochemical Capacitances

We now discusses the charge storage capacities of Janus compounds by making a comparison with corresponding end point MXenes. In both cases, the MXene electrodes are in contact with H_2SO_4 solution. In this work, we have calculated charge transfers and capacitances with applied electrode potential(ϕ) in the range -1V to +1V vs. SHE. In Figure 5.7(a)-(f), variations in proton number,

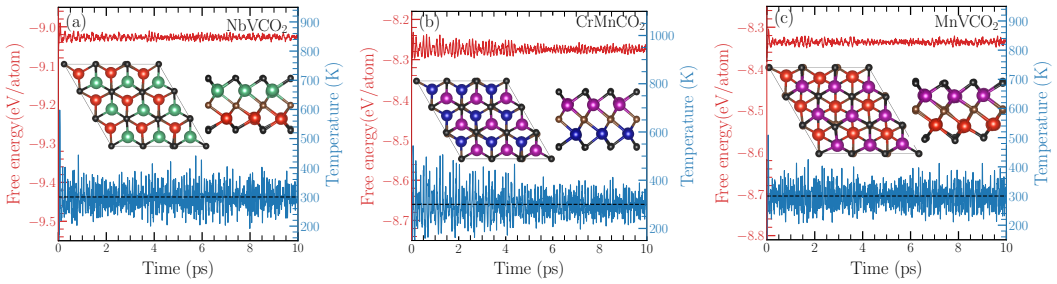

Figure 5.6: Variations in Free Energy(eV/atom) and Temperature(K) with time step(in ps) in AIMD calculations for (a)$NbVCO_2$, (b)$CrMnCO_2$, and (c)$MnVCO_2$. Insets show the top(left) and side(right) views of the final structures.

Table 5.2: Sites of -O functionalisation, lattice-parameter(a), lengths of M-C(d_{M-C}),M′-C($d_{M'-C}$), M-O(d_{M-O}), M′-O ($d_{M'-O}$) bonds, electronic and magnetic ground states (GS) of all the $MM'CO_2$, M_2CO_2 and $M'CO_2$ MXenes are shown. Magnetic moments of transition metal constituents are also shown for magnetic systems.

Properties	Systems						
	Nb_2CO_2	$NbVCO_2$	V_2CO_2	$MnVCO_2$	Mn_2CO_2	$CrMnCO_2$	Cr_2CO_2
Sites of -O functionalisation	HH	CC	HH	CH	HH	CC	CC
a(Å)	3.12	2.95	2.91	2.87	2.88	2.68	2.69
d_{M-C} (Å)	2.19	2.17	2.06	2.00	2.04	2.00	2.02
$d_{M'-C}$ (Å)	-	2.06	-	2.08	-	2.00	-
d_{M-O} (Å)	2.09	2.08	1.95	1.93	1.93	1.92	1.92
$d_{M'-O}$ (Å)	-	2.01	-	1.92	-	1.90	-
Magnetic GS	NM	NM	NM	FM	AFM	AFM	NM
Electronic GS	metallic	metallic	metallic	metallic	semi-conductor	metallic	metallic
Magnetic moment μ_i of magnetic species i (in μ_B)	-	-	-	μ_{Mn}=1.2 μ_V = 0.95	μ_{Mn}=±2.8	μ_{Cr}=±0.1 μ_{Mn}=±1.0	-

surface charge, and electron number along with variations in corresponding capacitances with ϕ are shown for $NbVCO_2$ Janus and the corresponding end point MXenes Nb_2CO_2 and V_2CO_2). To understand the results, we first discuss the charge storage mechanism of Nb_2CO_2 and V_2CO_2. As seen from Figure 5.7(a), the proton transfer number of Nb_2CO_2 decreases following a parabolic trajectory as the voltage is increased from -1V, resulting in a decrease of C_{redox} (Figure 5.7(d)). The change is substantial - from 251 F/g at -1V (vs. SHE) to 10F/g at 0.6V (vs. SHE), saturating thereafter. C_{EDL} of Nb_2CO_2 shows the opposite trend. The surface charge increases with ϕ (Figure 5.7(a)), the change being slower than the proton transfer. Accordingly, C_{EDL} increases continuously and eventually becomes the dominant contributor to C_E at $\phi > -0.25V$. Thus, both EDL and Redox mechanisms contribute to the charge storage capacity of this compound, producing a maximum(minimum) C_E of 240(64) F/g (Figure 5.7(d)). The storage mechanism of V_2CT_2, on the other hand, is significantly dominated by the Redox mechanism. The proton transfer number varies linearly with ϕ, the slope of the curve being large. The variation in surface charge is linear, too. However, the change is rather small with increasing ϕ (Figure 5.7(c)). As a result both C_{redox} and C_{EDL} remain constant at values 264 F/g and 36 F/g, respectively up to $\phi = 0.4V$. After that their values decrease slightly to 237 F/g and 30 F/g, respectively at $\phi = 1$V (Figure 5.7(f)), resulting in a maximum C_E of 228 F/g.

Both proton transfer and surface charge variations in the case of $NbVCO_2$ follow two distinct patterns in two potential windows. The proton transfer number varies linearly up to between -1.0-0.25V, following the pattern of V_2CO_2, albeit with a higher slope. Between 0.25V and 1.0V, the variation is like the one obtained for Nb_2CO_2. The same trend is found for variations in the surface charge. Consequently, in the negative (positive) potential window, both C_{redox} and C_{EDL} behaviors resemble that of V_2CO_2(Nb_2CO_2). However, due to sharper variations in the proton transfer implying higher redox activity, as compared to the end point MXene compounds, C_{redox} varies between 328 F/g and 307 F/g in the negative potential window. In the positive potential window,

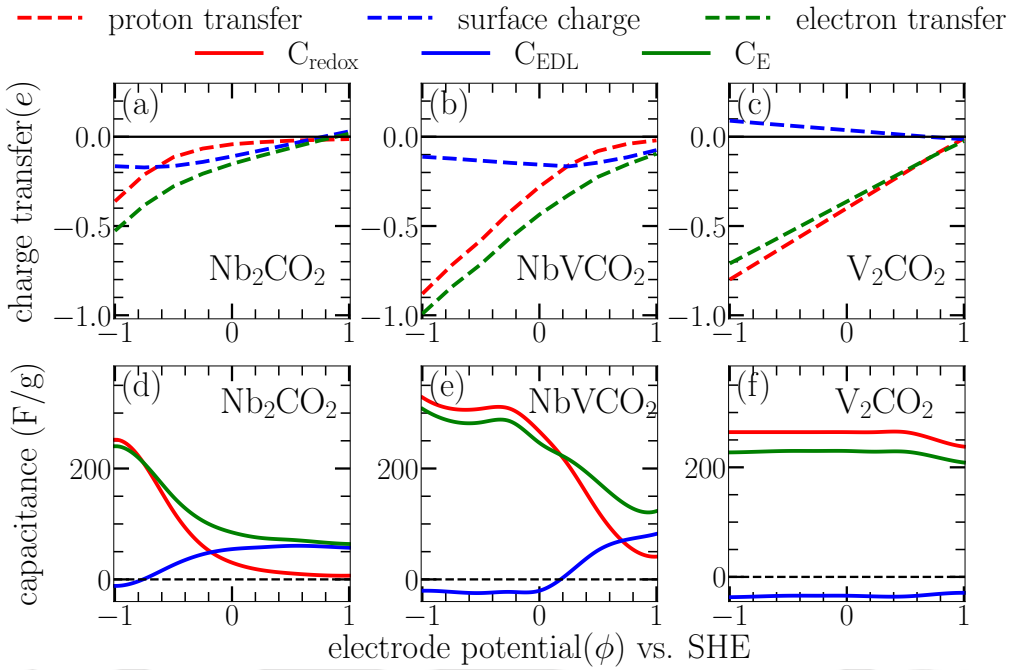

Figure 5.7: Various contributions to charge transfer and capacitance for Nb_2CO_2, $NbVCO_2$ and V_2CO_2

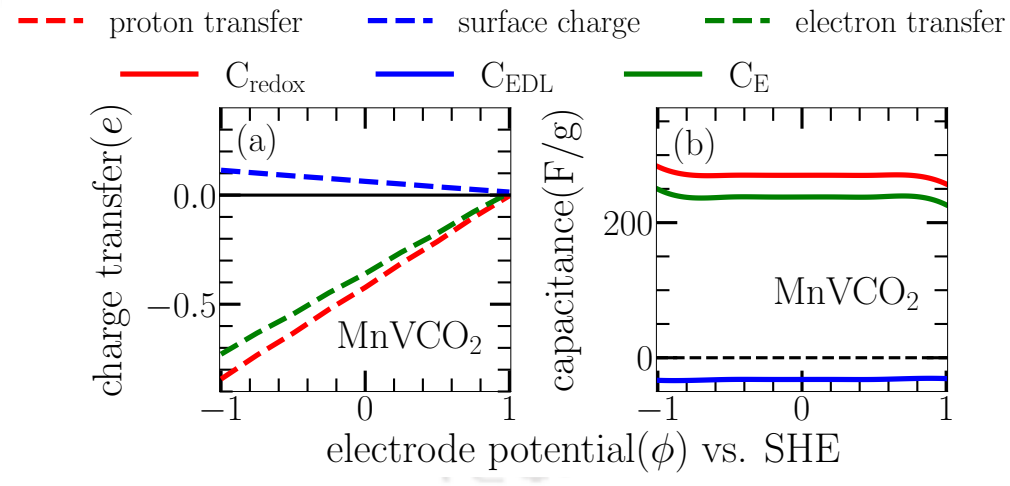

Figure 5.8: Various contributions to charge transfer and capacitance for Nb_2CO_2, $NbVCO_2$ and V_2CO_2

C_{redox} decreases rapidly to about 50 F/g at 1.0V. C_{EDL}, on the other hand, increases continuously to a maximum of 80 F/g at 1.0 V. Therefore, the total capacitance C_E varies between 307-285 F/g (170-130 F/g) in the negative (positive) potential window. This implies that if one chooses the negative potential window, the enhanced redox activity will produce a significantly larger C_E for this Janus compound in comparison to their M_2CO_2 counterparts. Moreover, this result suggests that more power density, compared with the end compound MXenes, can be extracted from Janus $NbVCO_2$ in the negative ϕ window. On the other hand, in the positive ϕ region, larger energy density along with substantial power density can be obtained by synthesizing Janus out of Nb_2CO_2 and V_2CO_2 MXenes, making this Janus very useful as a supercapacitor electrode.

In Figure 5.8, we present the electrochemical behavior of $MnVCO_2$. Here we have not shown the electrochemical behavior of the end point compound Mn_2CO_2. The electronic ground state

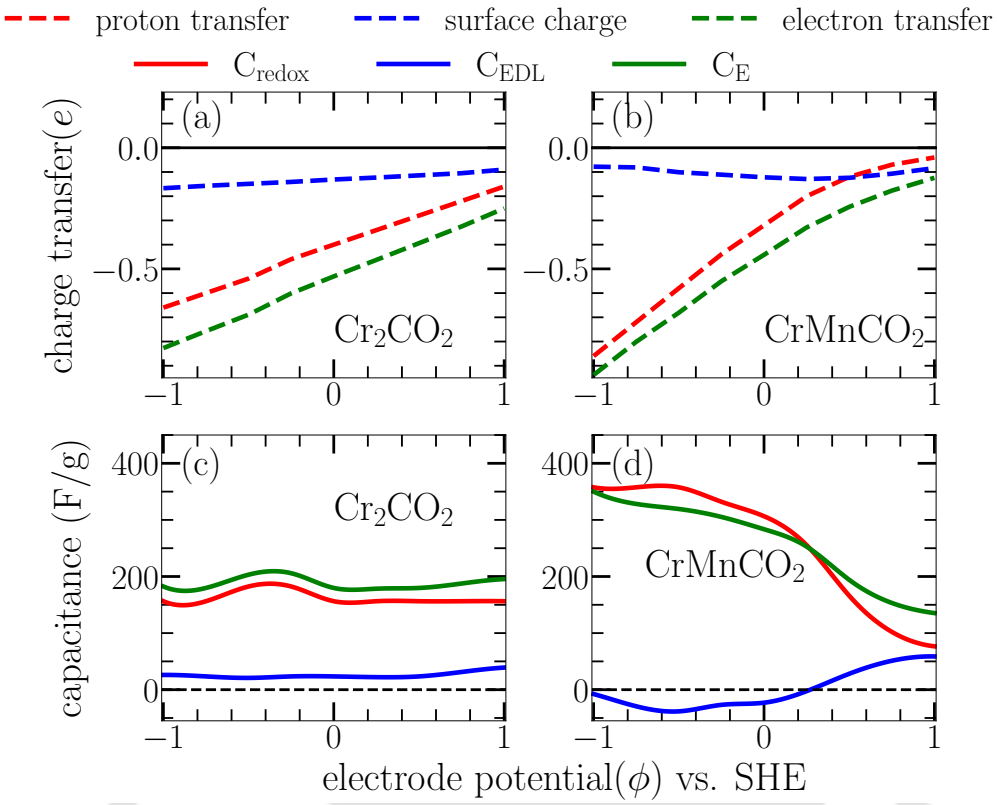

Figure 5.9: Various contributions to charge transfer and capacitance for Nb_2CO_2, $NbVCO_2$ and V_2CO_2

of Mn_2CO_2 is semiconducting. Thus, it cannot be a high-rate storage device like a metal. The variations in surface charge and proton transfer will be much less than the metallic MXenes. The variations in proton transfer number, surface charge, and consequently the capacitances of $MnVCO_2$ Janus, expectedly, follow the same trend as that of V_2CO_2. The sharper variations in the proton transfer, however, produce C_{redox} larger than that obtained for V_2CO_2. As a result, the total capacitance C_E varies between 249 F/g - 226 F/g over the entire potential window.

Various contributions to the charge transfer and capacitance and their variations with ϕ for Cr_2CO_2 and $CrMnCO_2$ are shown in Figure 5.9. Like V_2CO_2, the charging mechanism in Cr_2CO_2 is dominated by the redox charge transfer. But unlike V_2CO_2, EDL has a co-operative effect to C_{redox}. Smaller variation in the proton transfer, in comparison to V_2CO_2, however, limits C_{redox} to a maximum value of 175 F/g for a small potential window and to a constant value of 156 F/g for the rest of the potential range. Consequently, C_E varies between 179 -200 F/g. The variations of the electrochemical parameters in $CrMnCO_2$ Janus, contrary to the intuition, are quite different. The proton transfer number and the surface charge vary in such a way that between -1V-0.25V, the C_{redox} after staying constant initially decrease; C_{EDL} opposes C_{redox} in this potential window. Between 0.25-1.0V, C_{redox} decreases faster while C_{EDL} co-operates with it. In this potential range, the EDL charge storage mechanism catches up with the redox one gradually, having almost equal contributions at ϕ close to 1V. It is noteworthy that at ϕ=-1V, EDL has no contribution to total capacitance, and total capacitance is 350 F/g, the highest among the three Janus compounds considered in this work. Due to the continuous weakening of the redox mechanism and thus gradual fall in C_{redox}, C_E also decreases substantially to a minimum of 135 F/g at ϕ=1V.

The similarity among the three Janus compounds concerning their electrochemical properties is the dominance of the redox mechanism of charge storage along with significant enhancement in the capacitances to the end point M_2CO_2 MXenes. The dissimilarity is in the trends in the capacitance variations, particularly C_{redox} over the potential window considered. To understand the origin of these, we look at the variations in the charge states of the transition metal constituents in M_2CO_2 and the corresponding Janus MXene. In $NbVCO_2$, in the redox-dominated potential window that

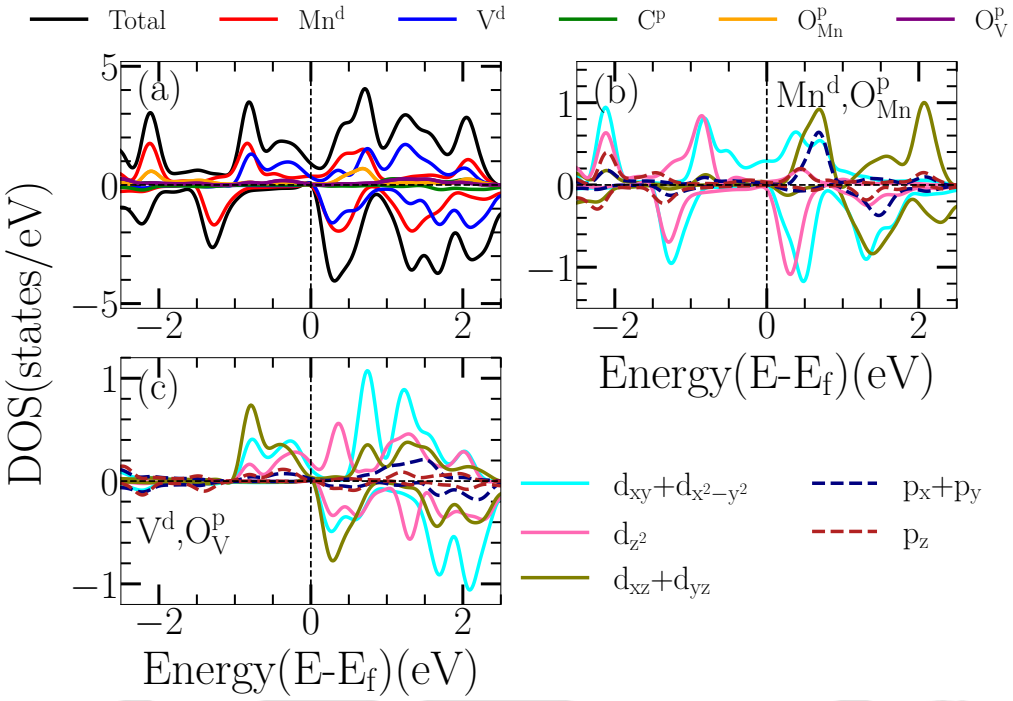

Figure 5.10: (a) Total and Partial densities of states of $MnVCO_2$ (b) d and p orbital projected densities of states of Mn and O(connected to Mn), (c) d and p orbital projected densities of states of V and O(connected to V)

is predominantly $\phi \leq 0$V, the charge state of Nb hardly changes (1.83-1.86) while the charge state of V changes substantially from 1.51 to 1.63. This change is quantitatively slightly more than the change in V_2CO_2 (1.57-1.67). However, the change is more rapid in the Janus compound. For $\phi > 0$V, the change in the charge state of V in $NbVCO_2$ is substantially smaller (1.63-1.69) than that in V_2CO_2 (1.67-1.78). This is the reason behind significant drop in the C_{redox} for $\phi > 0$V in $NbVCO_2$. Therefore, the variations in C_{redox} of $NbVCO_2$ can be understood in terms of the variations in the charge states of Nb and V. In Janus $MnVCO_2$, the charge of V does not undergo a significant deviation from V_2CO_2, either qualitatively or quantitatively. In the Janus, it varies between 1.54 and 1.70 over the entire potential window. In V_2CO_2, the variation is between 1.57 and 1.78. The Mn charge state, on the other hand, undergoes a variation that is larger and more rapid than that in end point MXene Mn_2CO_2. In Mn_2CO_2, the charge state of Mn varies between 1.51 and 1.63 over the entire potential window. In $MnVCO_2$, it varies between 0.97 and 1.28 over the same window. The larger values of C_{redox} along with its nature of variation for $MnVCO_2$, thus, is due to the chemistry of the Mn surface. The case of $CrMnCO_2$ is intriguing. Since Mn_2CO_2 is a semiconductor and variations in the capacitances of $MnVCO_2$ followed the qualitative nature of V_2CO_2, it is only natural to expect that the same would happen in $CrMnCO_2$. The departure from the expectation has roots in the behavior of the charge states of Mn and Cr. In Cr_2CO_2, the charge state of Cr varies by 0.04 as ϕ varies between -1V and 0.25V. The variations for the rest of the potential window are even smaller. This explains the maximum C_{redox} around -0.5V (Figure 5.9))and a smaller value of it in comparison to V_2CO_2. Neither the charge state nor its variation undergoes any noticeable change in $CrMnCO_2$ except that beyond ϕ=-0.25V, the charge state almost does not change. The Mn charge state in $MnCrCO_2$, on the other hand, behaves differently in different potential windows. The charge state of Mn varies more rapidly in $CrMnCO_2$ than in Mn_2CO_2. In the negative potential window, between ϕ=-1.0V and -0.5V, Mn charge state changes by 0.19 in the Janus compound; the change is only 0.02 in Mn_2CO_2. However, in the Janus, the maximum change in the charge state of Mn for the rest of the potential window is 0.02. Such a large variation in Mn charge state for a small window explains the largest possible C_{redox} obtained in the work. The stagnant charge state of both Mn and Cr for the larger part of the potential window explains why C_{redox} continuously decreases in $CrMnCO_2$.

Thus, for both the Mn-based Janus, it is the Mn that takes the pro-active role to enhance the redox mechanism and consequently the redox charge storage capacity, despite the absence of redox

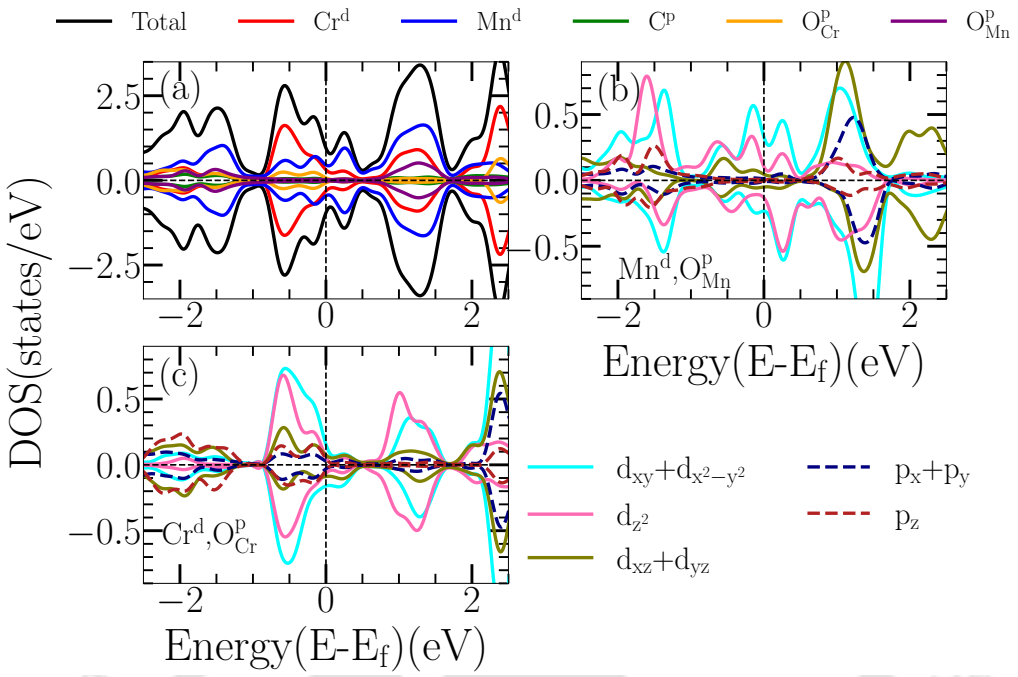

Figure 5.11: (a) Total and Partial densities of states of $CrMnCO_2$ (b) d and p orbital projected densities of states of Mn and O(connected to Mn), (c) d and p orbital projected densities of states of Cr and O(connected to Cr)

activity in Mn_2CO_2 MXene. The reason must lie in the changes in the electronic structure of Mn in both Mn-based Janus compounds. The significant re-distribution of Mn states in metallic Janus compounds in comparison with Mn states in semiconductor Mn_2CO_2 changes Mn charge states substantially. From Figures 5.10 and 5.11, we can see that the Mn $d_{xy} + d_{x^2-y^2}$ states are dominant near the Fermi level of both Janus compounds. Hybridizations with p states of O and d states of the other transition metals delocalize the Mn states to a large extent. This explains why, even before the application of a voltage, the Mn charge state changes from 1.51 in Mn_2CO_2 to 1.28 in both Janus. It is to be noted that no other transition metal constituent has undergone such significant change in their charge states upon formation of Janus: V charge state changes from 1.78 in V_2CO_2 to 1.70 and 1.69 in $MnVCO_2$ and $NbVCO_2$, respectively, Nb state changes from 2.0 in Nb_2CO_2 to 1.88 in $NbVCO_2$, Cr state varies from 1.38 in Cr_2CO_2 to 1.28 in $CrMnCO_2$. The application of external voltage, therefore, affects the charge state of Mn more than that of others.

5.4 Conclusions

This work is the first attempt to assess the potential of Janus MXenes as electrodes in supercapacitors. Since the experimental synthesis of Janus MXenes is yet to happen, we chose systems in which either the Janus MAX phase or a MXene solid solution is synthesized. Careful test on their thermal and dynamical stabilities are performed to make sure the choice of Janus phase in these compounds are justified. Out of six compounds considered, only three were found to be thermodynamically stable up to room temperature. The key result obtained is that the charge storage capacity increases significantly in Janus MXenes $MM'CO_2$ in comparison with the end point MXenes M_2CO_2 and M'_2CO_2. In all cases, the enhanced storage capacity is due to enhanced redox activity upon formation of Janus. The reason behind such enhancements lies in the rapid changes in the charge states of the transition metal constituents forming the Janus. The formation of Janus breaks the symmetry of M_2C MXenes and affects the electronic structures of the constituents substantially. This in turn affects the charge states. The degree of variation in the charge states decides the quantum of increment in redox capacitance. This work throws a reasonable amount of light on the role of surface engineering and the chemistry of materials in the context of energy storage devices. Our work shows that this can be a viable route to obtain greater storage capacity when MXenes are used as electrodes in supercapacitors.

An important outcome of this work is the influence of the magnetic element (here, Mn) present in the electrode material on the charge storage capacity. It goes without saying that the, extensive change in the charge state of Mn on changing the electrode potential has affected the surface redox activity of $MnVCO_2$ and $CrMnCO_2$. To our knowledge, no experimental or theoretical study exists to assess the positive effect of magnetic elements on the surface redox activity of a system. In the next chapter, we dig further into this aspect by considering charge storage capacities of solid solution MXene electrodes comprising of two transition metal constituents, out of which one is magnetic.

Chapter 6

Effects of chemical and magnetic disorder on electrochemical properties of MXene supercapacitor electrodes

6.1 Introduction

Solid solutions of compounds are often considered to be the route to achieve improvements in the target properties. Attempts in this direction have been made for MXenes as well. Consequently, $(Ti,V)_3C_2$[166], $(Nb,V)_2C$[84, 167] and $(Ti, Nb)_2C$,[84, 167] $(Ti,V)_2C$[167] MXene solid solutions have already been synthesized. The variations in the electrochemical performances of $Ti_{2-y}Nb_yT_x$ and $V_{2-y}Nb_yT_x$ ($0<y<2$) solid solutions as a function of compositions have been investigated by Wang *et.al.*[84]. To our knowledge, this is the first comprehensive study on the electrochemical properties of solid solution MXene. In this work, they found that the charge storage capacities of $(Ti,Nb)_2C$ and $(V,Nb)_2C$ solid solutions lie between the end-point compounds. Apart from these, several solid solutions of MAX compounds, the precursor to MXenes, have been prepared [25]. The synthesis of MAX compounds implies that obtaining MXene solid solutions with those constituents is only a matter of time.

Prominent among the solid solutions in MAX compounds are $(V,Mn)_2C$, $(Cr,V)_2C$, and $(Cr,Mn)_2C$ [25]. These compounds stand out as either one or both transition metal constituents are magnetic elements. Although the study of magnetism in 2D materials is still in its infancy, enormous potential in the fabrication of devices by exploiting different magnetic orders makes them interesting research subjects. The long-range orders found in recently synthesised 2D CrI_3 [168], VSe_2 [169], $Cr_2Ge_2Te_6$ [170] and Fe_3GeTe_2 [171] have given the research on exploring magnetism in 2D crystals a filip. In recent years, investigations into the structure-magnetic property relations in MXenes have also started. Although the number of experimental results on magnetic MXenes, to date, is limited, a plethora of first-principles electronic structure calculations [172, 173, 174, 175, 176] have revealed exciting magnetic behavior in them.

With regard to studies on MXenes in assessing their potential for various applications, what is absent is studies on the impact of magnetism on properties other than the magnetic ones, for example, the electrochemical performances. As MXenes have mostly been investigated with regard to their electrochemical performances so that they can be used as suitable electrodes in electrochemical reactions, it is only appropriate to assess the electrochemical performances of MXenes having one or more magnetic constituents. The role of magnetic orders on the electrochemical performances in such systems would provide important insights into the interrelations of magnetic and chemical interactions. Moreover, the simultaneous presence of chemical and magnetic disorders in a single material can give rise to interesting and novel phenomena that can provide a different perspective on the physics and chemistry of the material. Solid solution MXenes with magnetic components are tailor-made systems for such investigations into the effects of chemical and magnetic disorders on their electrochemical properties.

Using Density Functional Theory (DFT)[177] based electronic structure methods, in this work, we

investigate the impacts of chemical and magnetic orders on the electrical and geometrical contributions to the total capacitances and, thus, the charge storage capacities of oxygen (-O) functionalized $V_{2-x}Mn_xC$ MXenes. We systematically investigate the effects of different disorders by tuning the degree of spin disorder for systems with a given chemical composition. For the first time, our work addresses such issues by making an in-depth exploration of physics at the microscopic level. Our results illustrate the inter-dependence of chemical and magnetic disorders in modifying the charge storage capacity of MXenes, an important aspect of device fabrication.

6.2 Modeling of chemical and magnetic disorder and Computational details

6.2.1 Modeling of chemical disorder

Our modeling of the 2D solid-solution structure of $V_{2-x}Mn_xC$; $x = 0.5, 1, 1.5$ starts by the construction of a 4×4×1 cell of optimized V_2C MXene. The monolayer is modeled by keeping a large inter-layer distance of 15 Å. The solid solutions that are completely random alloying of V and Mn are then obtained by replacing V with Mn atoms in such a way that each Mn has the same environment. This results in 12, 12, and 4 configurations for systems with $x = 0.5, 1.5$ and 1, respectively. The stabilities of these configurations are assessed by computing their formation energies

$$E_{formation} = E(V_{2-x}Mn_xC) - [(2-x)E(V) + (x)E(Mn) + E(C)] \quad (6.1)$$

$E(V_{2-x}Mn_xC)$; x=0.5,1.0,1.5, is the total energy of the solid solution considered, and E(Mn),E(V), and E(C) are the energies of constituent elements in their respective ground states. The process of exfoliation of MXene from the MAX phase inevitably results in surface passivation of by -F, -O, and -OH functional groups[10]. There is enough evidence to suggest that the -O functional group primarily contributes to the redox capacitance, whereas -F and -OH contribute to the electrical double-layer capacitance[88]. For the purpose of our investigation, in this paper, we consider -O surface passivated solid solution MXene $V_{2-x}Mn_xC$. The three possible positions of -O atoms on the surface of pristine MXenes are shown in the Figure 2.2(a, b). Accordingly six different O occupancy models are possible. In this work, we have considered all six models for finding the most stable configuration of the functionalized MXene solid solutions.

6.2.2 Modeling of magnetic disorder

In order to investigate the role of magnetism on the functional properties the first thing to determine is whether the ground states of the systems considered are magnetic. To do this, we first consider five different ordered spin configurations for spin-polarised calculations (Figure 6.1(a)-(e)), namely, A) Ferromagnetic where all M elements have their moments aligned along c-axis (Figure 6.1(a)), B) Anti-ferromagnetic-c, where M elements in the top(bottom) layers have their moments aligned(anti-aligned) along c-axis (Figure 6.1(b)) but in-plane moments align, C) Anti-ferromagnetic-a where the moments are anti-aligned along a-axis but are aligned along other two directions (Figure 6.1(c)), D) Anti-ferromagnetic-b where (Figure 6.1(d)), the moments are anti-aligned along b-axis but are aligned along other two directions and E) Anti-ferromagnetic-abc where the system overall has an anti-ferromagnetic structure (Figure 6.1(e)). For a given chemical composition, the energetically lowest state obtained from total energy calculations on all five magnetic configurations is identified as the ground state of the system. With the increase in temperature, the spin ordering gradually gives way to a partial and finally complete spin-disordered paramagnetic state. A key component in the present work is to investigate the impact of the magnetic disorder on the electrochemical properties of the MXenes considered. One may think of turning the spin polarisation off to model the paramagnetic state as the total magnetic moment is still zero in the paramagnetic state. This would, nevertheless, amount to a loss of information on magnetic interactions among transition metal atoms which are very much prevalent in the paramagnetic state. Moreover, the modeling of the partial magnetic disordered states that are indirect representations of different temperatures of the systems would not be possible to model. A solution to this problem is wonderfully addressed by the Disordered Local Moment (DLM) method [178, 179]. In this method, each lattice site having magnetic constituent M is populated with a 50-50 binary disordered alloy $M^{\uparrow}_{0.5}M^{\downarrow}_{0.5}$; the ↑ (↓) indicate moments aligning along (against) the magnetization axis. This model thus simulates the

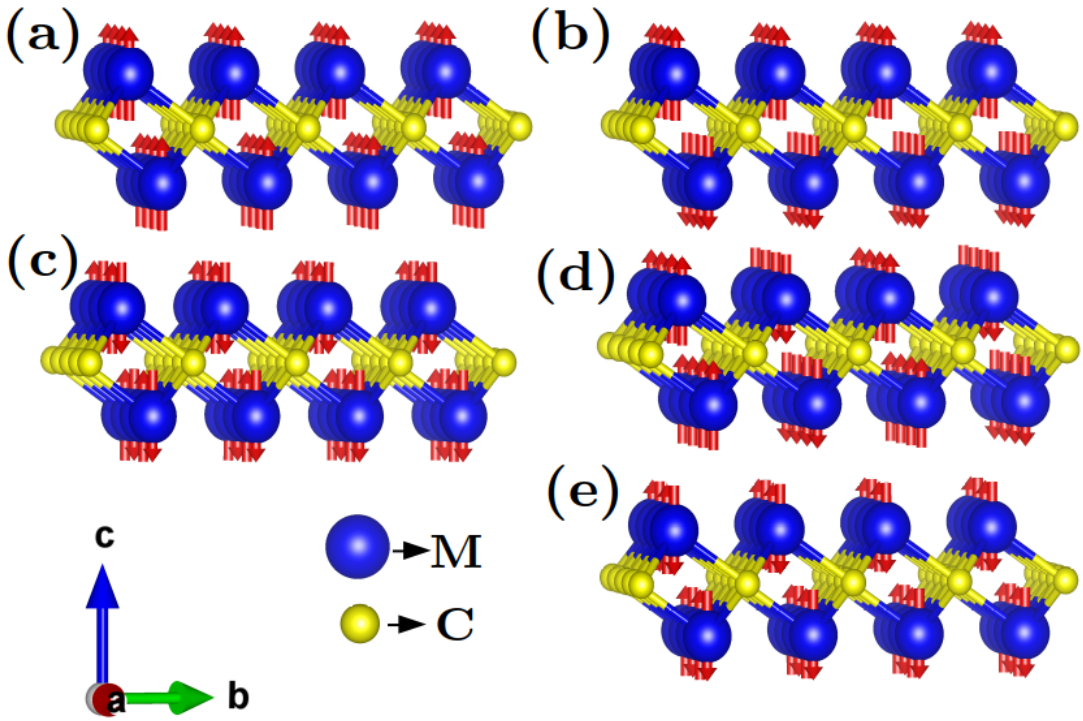

Figure 6.1: Illustrative representations of different ordered magnetic configurations considered in this work: (a)FM, (b)AFM-c, (c)AFM-a, (d)AFM-b, (e)AFM-abc.

paramagnetic state where local moments exist but due to the disorder, the global magnetization vanishes. Consequently, a partial disordered local moment (PDLM) state that models partially ordered magnetic structure is obtained by considering a binary alloy $M^{\uparrow}_{1-y}M^{\downarrow}_{y}$ at the site of the magnetic constituent M where 0<y<0.5. In a supercell setup, we obtain a DLM state by randomly orienting the moments of atoms in the direction of the magnetization axis, keeping the number of sites where moments are aligning with the magnetization axis equal to the number of sites where moments are anti-aligning (Figure 6.2 (a)). The PDLM state $M^{\uparrow}_{1-y}M^{\downarrow}_{y}$ is obtained by randomly picking up sites N, out of total M sites, where the spin configuration of N((M-N)) sites are ↑ (↓). A PDLM system with y=0.25 is schematically shown in Figure 6.2(b). In this work, for each of the three chemically disordered $V_{2-x}Mn_xCO_2$ MXenes, identified by their x values, we have considered several PDLM states by changing the ratio $\frac{y}{1-y}$ of moments aligning with the magnetization axis and moments aligning against it. Each PDLM state is identified by a parameter $\eta = \frac{n^{\uparrow}-n^{\downarrow}}{n^{\uparrow}+n^{\downarrow}}$, implying the degree of magnetic disorder; $n^{\uparrow}(n^{\downarrow})$ are the number of transition metal sites where spin moments aligned along (against) the magnetization direction. A decrease in η, therefore, corresponds to an increase in magnetic disorder in the system. Each PDLM state, thus obtained, is stabilized by performing a series of DFT+U calculations [180] where the Hubbard U parameters for Mn and V are systematically reduced from a high value to zero. This procedure not only stabilizes the PDLM states but also stabilizes the individual magnetic moments of Mn and V, converging them to values close to their ground states for a given solid solution system.

6.2.3 Computational Details

The electronic structure calculations are performed by the DFT-based projector augmented wave method [160]as implemented in Vienna ab-initio Simulation Package(VASP)[159]. The exchange-correlation part of the Hamiltonian is described by the Generalized Gradient Approximation (GGA)[138]. We use a kinetic energy cut-off of 520 eV and a Monkhorst-pack [161] grid of 4×4×1 for self-consistent calculations. A larger k-mesh of 6×6×1 is used for the Density of States calculations. The energy and force criteria were set to 10^{-6} eV and 0.05 eV/. We use RBA method (discussed in section 2.5.2)to compute the Electrical(C_E) capacitance of the considered systems.

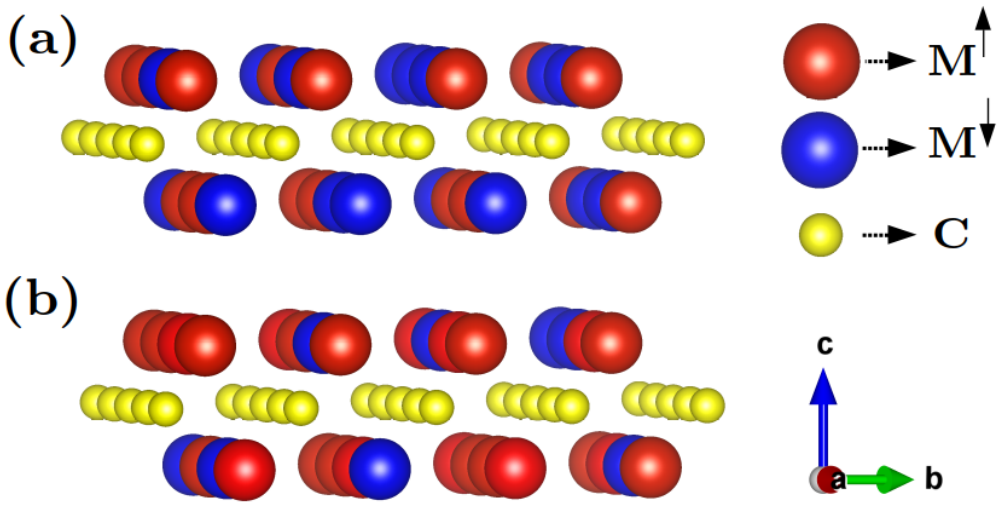

Figure 6.2: Illustrative representation of the arrangement of spin moments under the DLM picture used in this work: (a) a DLM system $M^{\uparrow}_{0.5}M^{\downarrow}_{0.5}$, and (b) a PDLM $M^{\uparrow}_{0.75}M^{\downarrow}_{0.25}$. $M^{\uparrow(\downarrow)}$ atoms are shown by red(blue) balls.The yellow balls represent the C atoms.

6.3 Results and Discussions

6.3.1 Ground state properties

The ground states of $V_{2-x}Mn_xCO_2$ for three different x are obtained the following way: non spin-polarised calculations are first done to find the optimised structure of $V_{2-x}Mn_xC$. In Figure 6.3(a), we show the formation energies of the configurations, relative to that of the ground state for each one of the three $V_{2-x}Mn_xC$ compounds. We find that the ground states are lower in energy by about 8 meV/atom at least, thus negating possibilities of near degeneracies in the configurations with respect to the ground state one.

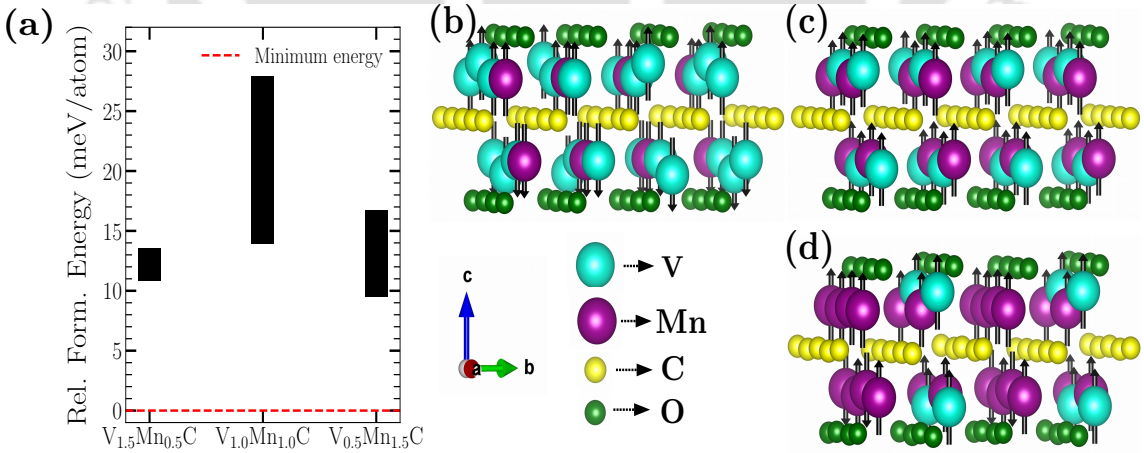

Figure 6.3: (a) The relative formation energies (Rel. Form. Energy) of $V_{2-x}Mn_xC$ for x=0.5, 1.0, 1.5 is shown. The red dashed line indicates the minimum energy configuration for that particular alloying composition and is set at 0 meV/atom. The respective black bars show the range of relative formation energies for the other configurations considered. Magnetic ground state of (b) $V_{1.5}Mn_{0.5}CO_2$, (c) $V_{1.0}Mn_{1.0}CO_2$ and (d) $V_{0.5}Mn_{1.5}CO_2$

For each of the three solid solution compounds, six different calculations by placing the oxygen atoms at different positions (H,C,T as shown in Figure 2.2(a, b)) on both surfaces are then done to determine the preferable sites of -O functionalization. After optimisation of the functionalised solid solution MXenes spin polarised calculations are done for each of the five magnetic configurations (Figure 6.1). The lowest energy structure obtained from the calculations is considered the final ground state of $V_{2-x}Mn_xCO_2$ for a given x. The ground states for the three compounds are

shown in Figure 6.3(b)-(d) and the relevant properties are listed in Table 6.1. In the ground states

Table 6.1: Lattice-parameters(a), magnetic ground states, and magnetic moments of constituent atoms of $V_{2-x}Mn_xCO_2$

System	a(Å)	magnetic ground state	moment(μ_B)			
			Mn	V	C	O
$V_{1.5}Mn_{0.5}CO_2$	11.64	AFM-c	+2.09 , -2.09	0.02	-0.07	-0.01
$V_{1.0}Mn_{1.0}CO_2$	11.64	FM	2.422	0.053	-0.03	-0.01
$V_{0.5}Mn_{1.5}CO_2$	11.48	FiM	2.7, 2.6,-1.7	0.38, 0.14	-0.07	-0.02

of the compounds, the favorable positions of the oxygen atoms are over the hollow sites of the transition metal atoms (Position "H" in Figure 2.2(a, b)). This is consistent with the fact that for the end-point compounds Mn_2C and V_2C, this is the preferred site for the oxygen functional group. However, the surfaces of the solid solution MXenes are rumpled. This rumpling is caused by significant differences in the distances between the two transition metal atom types on the top and bottom surfaces. This, once again, follows the trend found in the end-point compounds. The distance between M_1 and M_2 layers in V_2C (Mn_2C) is 2.18 Å (2.0 Å).Such differences are observed even in the solid solution of $MnVCO_2$. The V_1-V_2 (Mn_1-Mn_2) distances are 3.00 Å, 2.68 Å and 3.06 Å (2.22Å, 2.2 Å and 2.21 Å) for x=0.5,1.0 and 1.5, respectively. From Figure 6.3(b)-(d) and Table 6.1 it is evident that the magnetic ground states change with changes in the chemical composition. While the ground state of $V_{1.5}Mn_{0.5}CO_2$ is AFM-c, we get a ferromagnetic (FM) ground state for $V_{1.0}Mn_{1.0}CO_2$. The magnetic ground state of $V_{0.5}Mn_{1.5}CO_2$ is quite unique. For this compound in the ground state, the top surface comprises of Mn spins aligned along c-direction with moments 2.7 and 2.6 μ_B. The bottom surface, on the other hand, has a ferrimagnetic alignment of Mn spins. On this surface, one-third of the Mn atoms align anti-parallel to the other Mn atoms. The magnetic moments on anti-aligned Mn atoms are significantly reduced to 1.7 μ_B while the aligned Mn atoms have a moment of 2.7 or 2.6 μ_B on them. One more noteworthy result is the different V moments of the atom on the two surfaces of $V_{0.5}Mn_{1.5}CO_2$. While the V atoms in the top surface have a sizable magnetic moment of 0.38 μ_B, the bottom surface ones have only 0.14 μ_B of moment on them. This distribution of magnetic moments over Mn and V atoms on different surfaces can be correlated with their magnetic environment and variations in the lengths of the chemical bonds connecting neighboring transition metal atoms. Such surface dependent magnetic moments are not observed for the other two compounds. The moments of all Mn atoms for compositions with x=0.5,1.0 are the same. For these two compounds, the Mn moment increases with an increase in Mn concentration, an expected outcome due to the presence of more Mn in the neighborhood of each Mn. The correlations between the magnetic configurations on the surfaces and the chemical environment around a transition metal atom is likely to influence the localization of charges along a chemical bond. This in turn should have impacts on the surface-related phenomena, the main interest of this chapter. The following section discusses the correlation between the chemical and magnetic environment with the magnetic ground properties of $V_{2-x}Mn_xCO_2$.

Magnetic and chemical environments on the surfaces: correlations with the ground state magnetic properties of $V_{2-x}Mn_xCO_2$

There are 16 transition metal atom positions on either surfaces of $V_{2-x}Mn_xCO_2$ MXene solid solution in the $4 \times 4 \times 1$ supercell used here. The Carbon layer too has 16 positions. On each surface, there are 16 oxygen positions passivating the surfaces. For the ground state of x=1.5, the atomic arrangements on top and bottom surfaces are shown in Figures 6.4(a) and (b), respectively. On the top surface, spins of all Mn atoms align along c-direction while on the bottom surface, specific four out of twelve Mn atoms have their spins aligned opposite to c. Each one of these anti-aligned Mn is surrounded by four aligned Mn atoms in a hexagonal environment while each Mn atom, aligned along c, is in the surrounding environment of four Mn atoms, out of which two are also aligned. Two V atoms occupy the remaining vertices of this hexagonal network. In bottom surface the atoms Mn_{13}-Mn_{16} are anti-aligned whereas the rest are aligned. If one considers the hexagon with Mn_{16}, an atom whose spin is aligned opposite to c-direction (the other three with the same spin direction, out of total 12 atoms on this surface, are Mn_{13}-Mn_{15}), at the center, the four Mn atoms Mn_{19},Mn_{20},$Mn_{22}$and Mn_{24} occupying vertices of the hexagon, have their moments aligned along c. On the other hand, if the hexagon with Mn_{19} at the center is considered, Mn_{21}

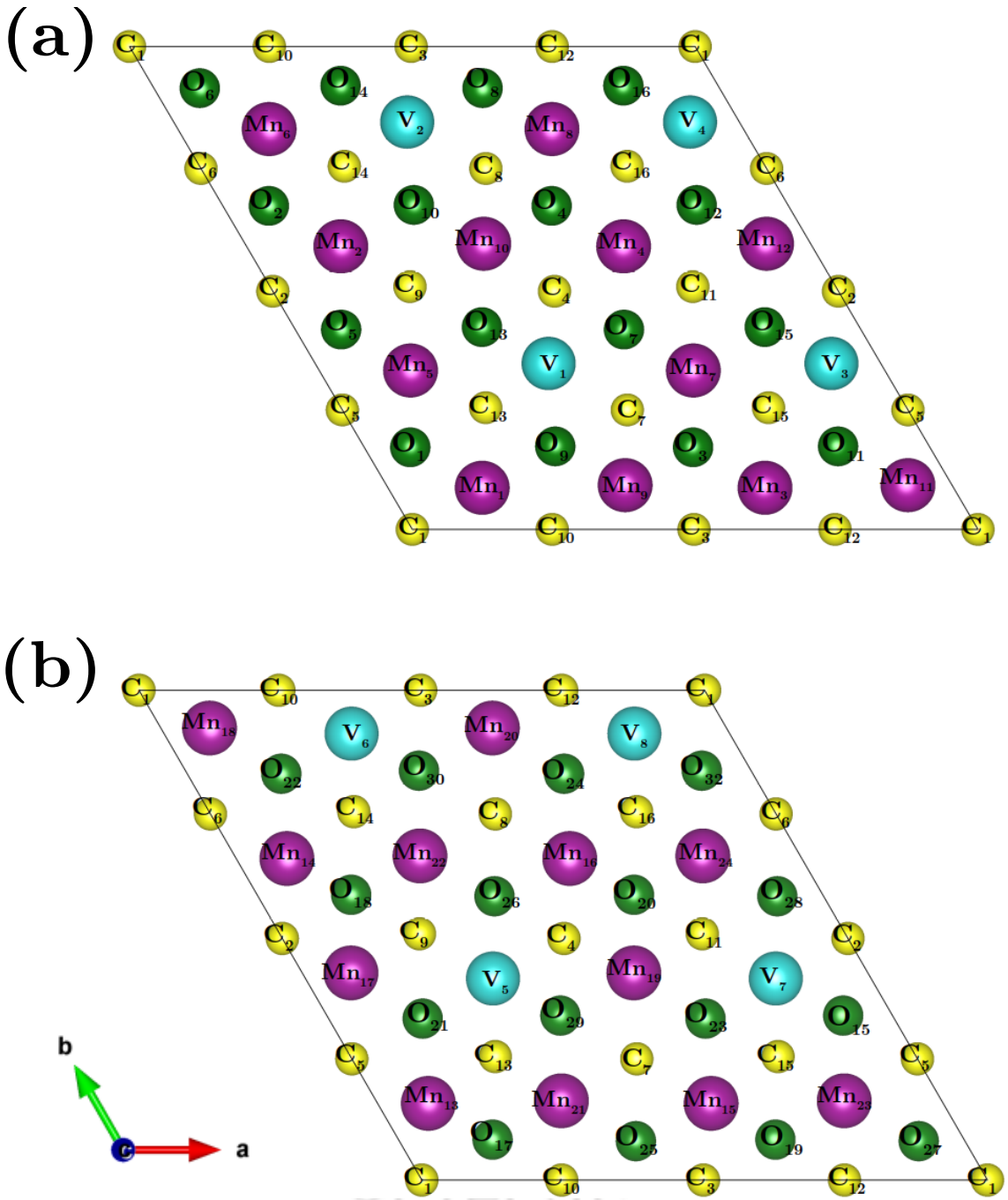

Figure 6.4: Top view of the (a)top and (b)bottom surfaces displaying full atomic arrangement in the ground state of $V_{0.5}Mn_{1.5}CO_2$

and Mn_{24} having aligned moments occupy two vertices while Mn_{15} and Mn_{16}, the two having spins anti-aligned, occupy other two vertices. Such arrangements make the magnetic environment around Mn atoms in the bottom surface inhomogeneous though the chemical environment is homogeneous. Upon inspecting the Mn-Mn bond distances, we find the following: (a) The Mn atoms in the top surface having a moment of 2.7 μ_B are connected to four Mn atoms sitting on the vertices of the hexagon around them with Mn-Mn bond distances along a line connecting three Mn atoms (which means two Mn-Mn bonds) between 2.84-2.86 Å and 2.92-2.94 Å For example, consider Mn_4 in Figure 6.4(a). The Mn_8-Mn_4, Mn_7-Mn_4,Mn_{10}-Mn_4 and Mn_{12}-Mn_4 bond distances are 2.83 Å, 2.93 Å, 2.86 Å and 2.92 Å, respectively. The ones that have their moments slightly reduced have one of the bonds shrunk to 2.75 Å while the other along the same line joining the three Mn elongated to 3.02 Å.For example, Mn_8-Mn_{10} and Mn_5-Mn_{10} bond lengths are 2.75 Å and 3.02 Å respectively,

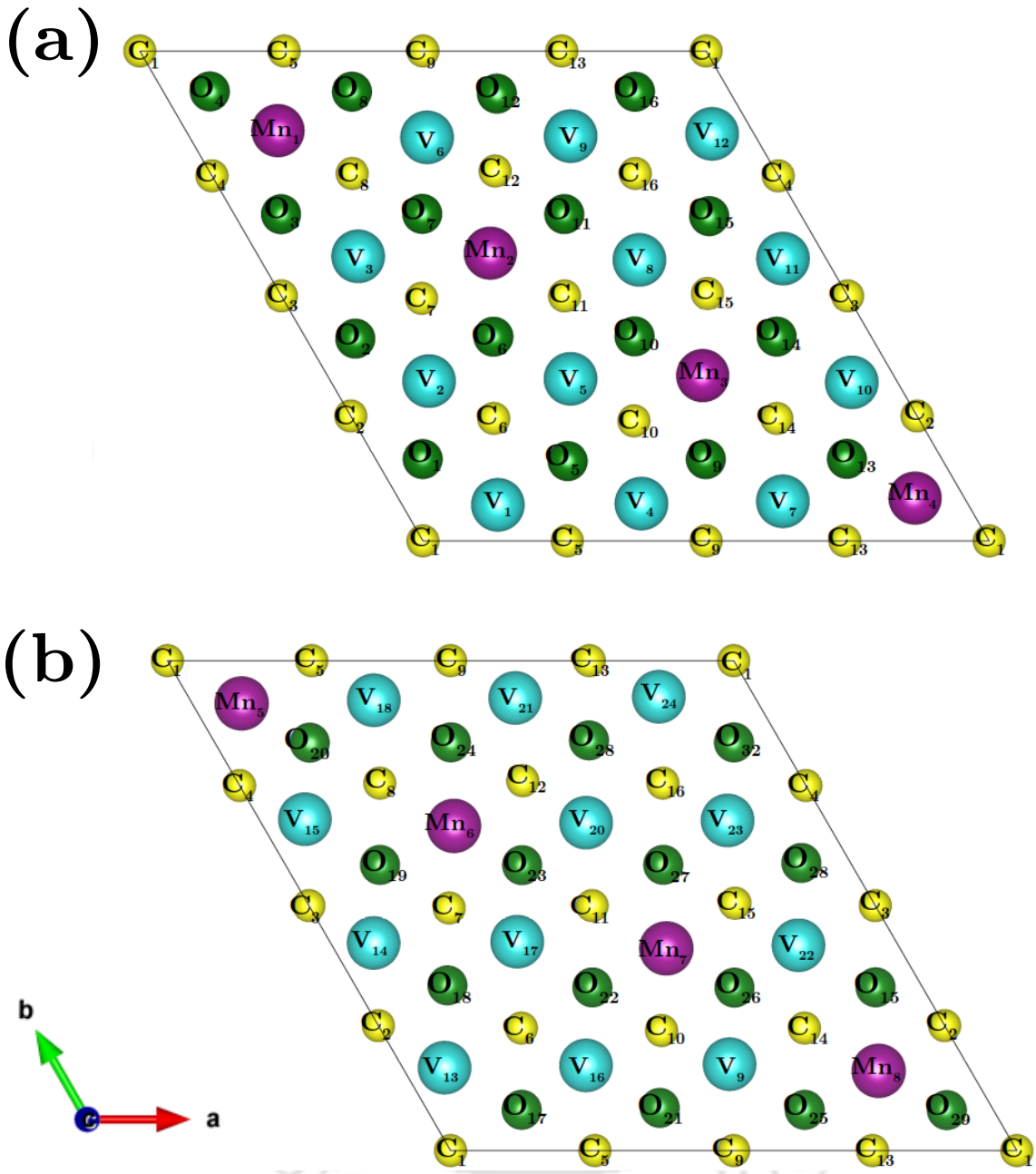

Figure 6.5: Top view of the (a)top and (b)bottom surfaces displaying full atomic arrangement in the ground state of $V_{1.5}Mn_{0.5}CO_2$

while Mn_2-Mn_{10} and Mn_4-Mn_{10} distances are more uniform, 2.86 Å and 2.92 Å, respectively. The Mn-V bond distances vary too; for Mn_1-Mn_4, the bond distances are 2.89 Å and 2.93 Å while for the rest 8 Mn, they are 2.84 Å and 3.0 Å rendering the bond lengths along a V-Mn-V line non-uniform, (b) in the bottom surface, when an anti-aligned Mn is connected to four aligned Mn, the two bond distances along a line connecting three Mn atoms are significantly non-uniform, one between 2.68 and 2.72 Å and the other between 3.06 and 3.1 Å. For example, in Figure 6.4(b), Mn_{16}-Mn_{22},Mn_{16}-Mn_{24},Mn_{16}-Mn_{19} and Mn_{16}-Mn_{20} bond lengths are 3.06 Å, 2.72 Å, 2.68 Å and 3.1 Å, respectively. When an aligned Mn is connected to two anti-aligned atoms, the distribution of bond distances are same. However, the two bond distances for bonds connecting three aligned Mn atoms are 2.77 Å and 3 Å For example, Mn_{19}-Mn_{24} and Mn_{19}-Mn_{21} shown in Figure 6.4(b), similar to the case of Mn in the top layer, have a moment of 2.6 μ_B. The moments on the V atoms on different surfaces can also be correlated to their chemical and magnetic environments. While the V atoms in the bottom surface, located at the center of a hexagon whose vertices have Mn atoms only, have moments of only 0.14 μ_B, the ones in the top layer, sitting in the same environment of

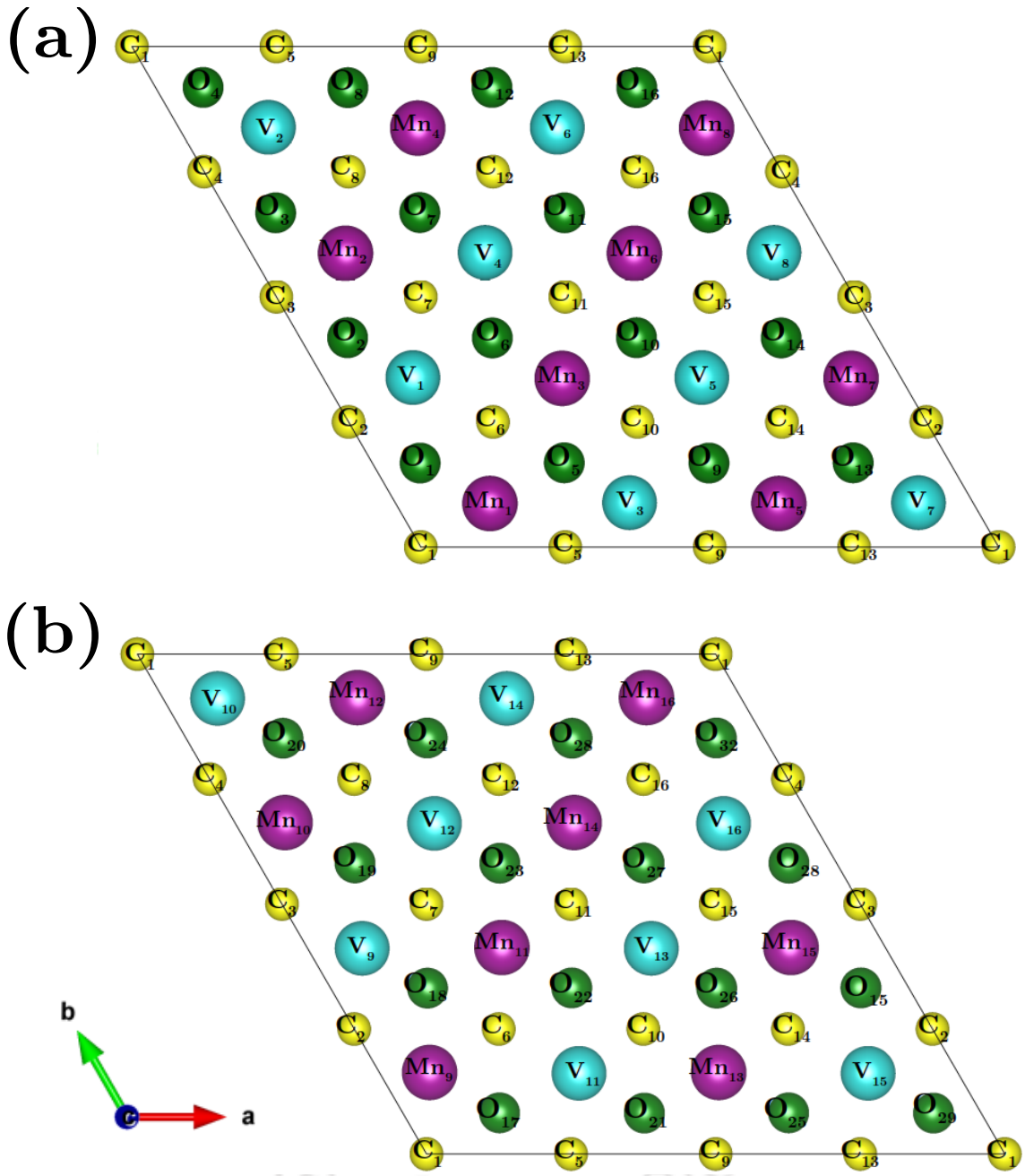

Figure 6.6: Top view of the (a)top and (b)bottom surfaces displaying full atomic arrangement in the ground state of $V_{1.0}Mn_{1.0}CO_2$

Mn, have moments of 0.38 μ_B localised on them. Here too we find an asymmetry in the Mn-V bond distances in the two surfaces. While the five Mn-V bond distances of the bottom surface vary between 2.87-2.94 Å, one of the Mn-V bonds in the top surface is elongated to 3 Å. Since the spin polarisation in V must be due to the magnetic Mn atoms, a slightly higher moment on V atoms in the top layer can be correlated with the non-uniform Mn-V bond distances.

In Figure 6.5(a)-(b), the arrangements of atoms on both surfaces of V-rich $V_{1.5}Mn_{0.5}CO_2$ are shown. Each surface has 12 V and 4 Mn atoms. Here each hexagon with a Mn at the center has six V atoms on the vertices. The distribution of Mn-V bond lengths are identical for both surface (There are three Mn-V distances, 3.07 Å, 2.95 Å and 2.72 Å). This can be correlated with identical Mn moments on each atom, irrespective of its location. The V moment is almost zero due to the lack of enough Mn in the neighborhood to polarize V.

In Figure 6.6(a)-(b), we show the atomic arrangements on the surfaces of $V_{1.0}Mn_{1.0}CO_2$. Here a Mn at the center of a hexagon has four V and two Mn on the vertices while a V at the center of

a hexagon has four Mn and two V at the vertices of the hexagon. In this case the bond lengths between the transition metals are again identical for both surfaces. The distribution of bond lengths in the neighborhood of a transition metal atom is also identical with Mn-V bond lengths being 2.82 Å, 2.86 Å, 2.99 Å and 3.02 Å, while Mn-Mn and V-V bonds having identical length of 2.91 Å. Due to no inhomogeneity in magnetic and chemical environment, moments on all Mn atoms are identical. The V atom is only slightly polarised due to presence of more Mn in its neighborhood in comparison with V-rich compound.

6.3.2 Electronic Structure: effect of chemical and magnetic disorder

The changes in the electronic structures due to changes in chemical composition and magnetic order are expected to be significant and throw insights into the role of each type of disorder. This may have a substantial impact on the electrochemical properties. Quantum capacitance is directly related to the electronic structure of the material; the changes in the charge transfer due to disorder will have effects on the electrical capacitance. In Figure 6.7 we have shown the total and atom projected densities of states of $V_{2-x}Mn_xCO_2$ for different chemically disordered compounds in the ground state. Since Mn and V atoms should play key roles, only their partial densities of states are shown. Though the ground state magnetic order is different in the three compounds, there are a few noticeable features that follow a trend. There is a sharp pseudo-gap around -1 eV in both majority and minority spin bands of $V_{1.5}Mn_{0.5}CO_2$. The symmetry with respect to the spin band is due to AFM-c magnetic order in this compound. This pseudo-gap turns shallow and nearly non-existent in $V_{1.0}Mn_{1.0}CO_2$. With further increase in Mn content, the pseudo-gap somewhat re-appears in the ground state of $V_{0.5}Mn_{1.5}CO_2$ at an energy closer to the Fermi energy and in the minority spin band only. The partial densities of states for the three compounds clearly show that the V bands are nearly unoccupied irrespective of the composition and the magnetic ground state. This explains the near-zero or at the most a small V moment. In order to understand the electronic structures better, we did a detailed analysis of all Mn and V partial densities of states in ground state in the following section.

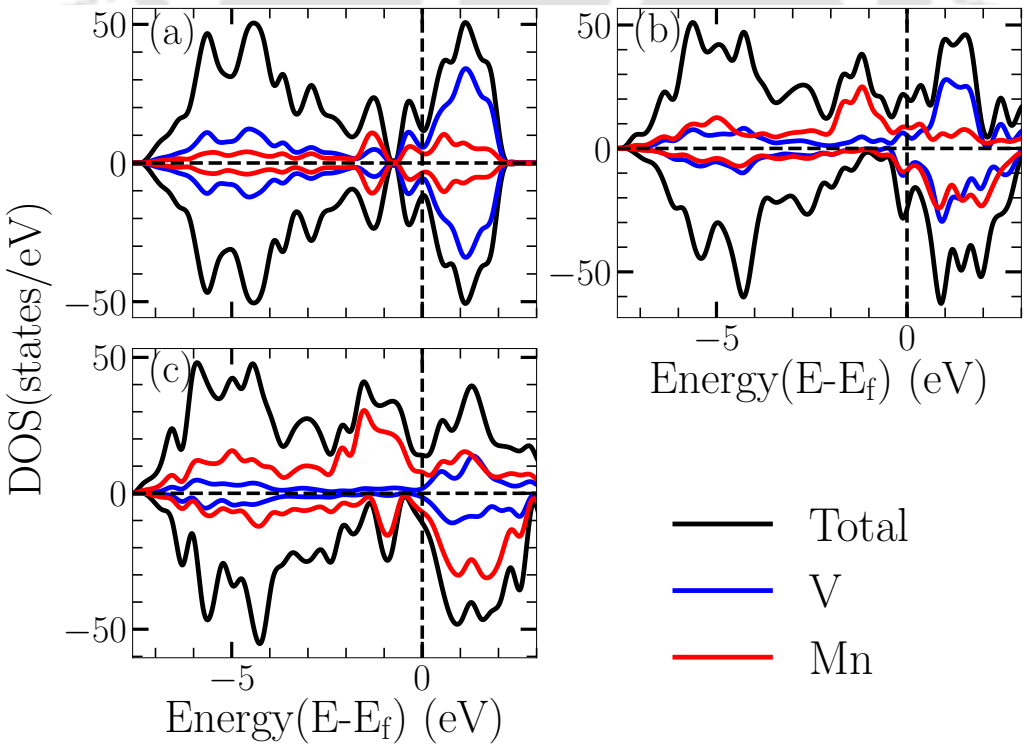

Figure 6.7: Electronic structure of the respective magnetic ground state of (a)$V_{1.5}Mn_{0.5}CO_2$, (b) $V_{1.0}Mn_{1.0}CO_2$ and (c) $V_{0.5}Mn_{1.5}CO_2$.

Mn and V partial densities of states in ground states of $V_{2-x}Mn_xCO_2$

Mn and V densities of states for $V_{2-x}Mn_xCO_2$ for different x in the ground states are shown in Figures 6.8-6.13. The features in the total densities of states shown in the Figure 6.7 can be understood in terms of the features in the atom projected densities of states. We find that the magnetic and chemical environment have significant effect on the atom projected densities of states. We find the presence of a pseudo-gap in V-rich compound that diminishes as Mn concentration increases, only to re-appear, albeit with strength considerably reduced, for the Mn-rich compound. The sharp pseudo-gap in the electronic structures of $V_{1.5}Mn_{0.5}CO_2$ is a consequence of strong hybridization of Mn d, V d and O p states.

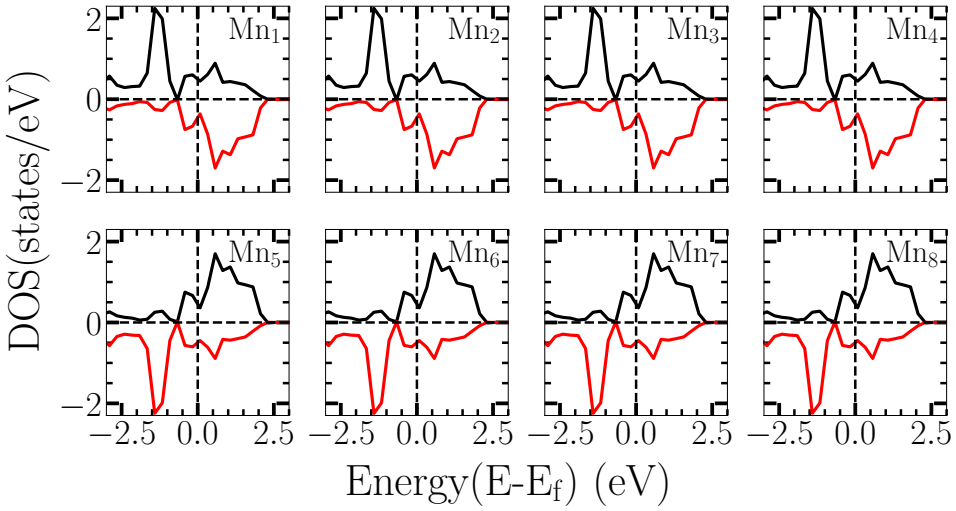

Figure 6.8: Projected Densities of States of each Mn atom in Ground State of $V_{1.5}Mn_{0.5}CO_2$

In this compound, the electronic structure of each Mn atom (Figure 6.8) is identical which is a reflection of an identical environment around them, in terms of chemical specie and the bond distances. Apart from Mn-V bond distances that are uniformly distributed within the hexagon around an Mn atom, Mn-O, and Mn-C bonds are nearly uniform (Mn-O bond lengths vary between 1.96 Å and 2.05 Å while Mn-C bond lengths vary between 2.03 Å and 2.08 Å). The V partial densities of states, on the other hand, can clearly be grouped into two bunches. Eight V atoms (V_2, V_4, V_9, V_{11}, V_{14}, V_{16}, V_{21} and V_{23}, Figure 6.9) have identical densities of states with a pseudo-gap like feature around -1 eV in both majority and minority bands. For these V atoms, out of the three V-O bonds, two are significantly smaller (1.76 Å) in comparison to the other (1.88 Å). For the other 16 V atoms, V-O bonds are much longer, between 1.93 and 2.12 Å. Such shorter V-O bonds result in stronger hybridization between d orbitals of V and p orbitals of O leading to the pseudo-gap in the electronic structures. This pseudo-gap like feature is observed in the other 16 atoms at a deeper energy. All Mn and V atoms in the ground state of $V_{1.0}Mn_{1.0}CO_2$ have identical electronic structures(Figure 6.10 and 6.11). This is expected as the chemical and magnetic environment around each atom is the same. The surfaces have identical spin alignments too. The effect of an increase in Mn content is visible if one compares with the Mn-deficient compound. An increase in chemical disorder smears the main Mn peak observed in the Mn-deficient compound, producing a peak and a shoulder. The Mn-V bonds relax as compared to the ones in the Mn-deficient system. In $V_{1.5}Mn_{0.5}CO_2$, Mn-V bond distances were 2.72 Å and 3.07 Å. In $V_{1.0}Mn_{1.0}CO_2$, they are 2.82 Å, 2.86 Å, 2.99 Å and 3.02 Å. Such relaxations in the bond lengths reduce the Mn-V hybridizations resulting in the pseudo-gap completely vanishing in the majority spin band and becoming shallow in the minority one. Larger disorder in Mn-rich $V_{0.5}Mn_{1.5}CO_2$, as compared to the Mn-deficient system now further delocalizes the Mn states (Figure 6.12). However, sharp peaks and more localization of the majority states is observed for 4 Mn atoms (Mn_1-Mn_4) in the upper surface. For these Mn, the Mn-transition metal bond lengths are more uniformly distributed, varying between 2.83 Å and 2.99 Å. For the other Mn atoms, two Mn bonds along a line joining 3 Mn atoms are severely non-uniform, 2.75 Å and 3.01 Å. The Mn-V bond lengths corresponding to these Mn atoms follow the same trend. Thus, in spite of having identical chemical environments, the larger non-uniformity in bond distances leads to a slightly smaller exchange splitting for these

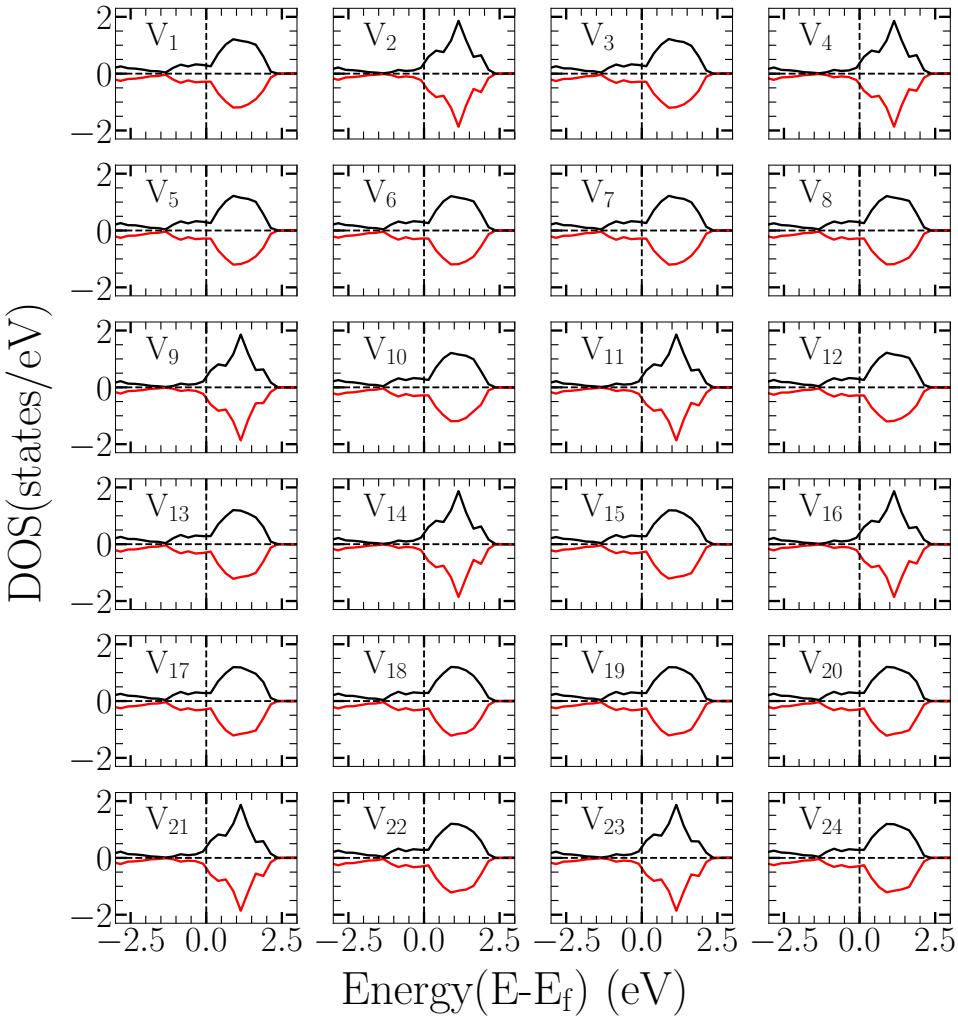

Figure 6.9: Projected Densities of States of each V atom in Ground State of $V_{1.5}Mn_{0.5}CO_2$

Mn atoms and delocalization in Mn states. The electronic structures of the V atoms are identical as expected(Figure 6.13). In the bottom surface, the inhomogeneity in the magnetic environments around a transition metal atom affects their electronic structures. Mn_{13}-Mn_{16} have their spins aligned along $-c$ direction and have more localized Mn states as compared to the other 8 Mn atoms in this surface which have spin orientations opposite to them. They are surrounded by four Mn with spins aligned along c and two V atoms. On the other hand, any one of the other eight atoms on the surface is surrounded by two Mn which have the same spin alignment as the atom in question and two others which have spin alignment opposite to it. This leads to a frustrated triangular network of Mn atoms resulting in a more delocalized electronic structure. The electronic structures of the four V atoms on this surface are identical as they are in identical chemical and magnetic environments. A pseudo-gap-like feature is observed in their minority bands, suggesting slightly stronger hybridization in comparison to that in $V_{1.0}Mn_{1.0}CO_2$. This can be due to slightly shorter and near uniform Mn-V bonds(bond lengths varying between 2.89-2.94 Å). The pseudo-gap-like feature is observed in the top surface Mn minority bands. There too, out of four Mn-V bonds, three vary between 2.84-2.93 Å only.

Electronic structure of $V_{2-x}Mn_xCO_2$ in magnetically disordered states

Total and atom-projected densities of states of $V_{2-x}Mn_xCO_2$ (x=0.5, 1.0, 1.5) for different magnetic disorder (η states) are shown in Figures 6.14-6.16. In Figure 6.14(b), we show the densities of states of a PDLM state $\eta = 0.5$ for $V_{1.5}Mn_{0.5}CO_2$. The PDLM state is obtained by flipping the spins of one atom (Mn_4, Figure **??**(c)) from the top surface and three atoms from the bottom surface (Mn_6-Mn_8, Figure **??**(d)). Consequently, the loss of symmetry with respect to the

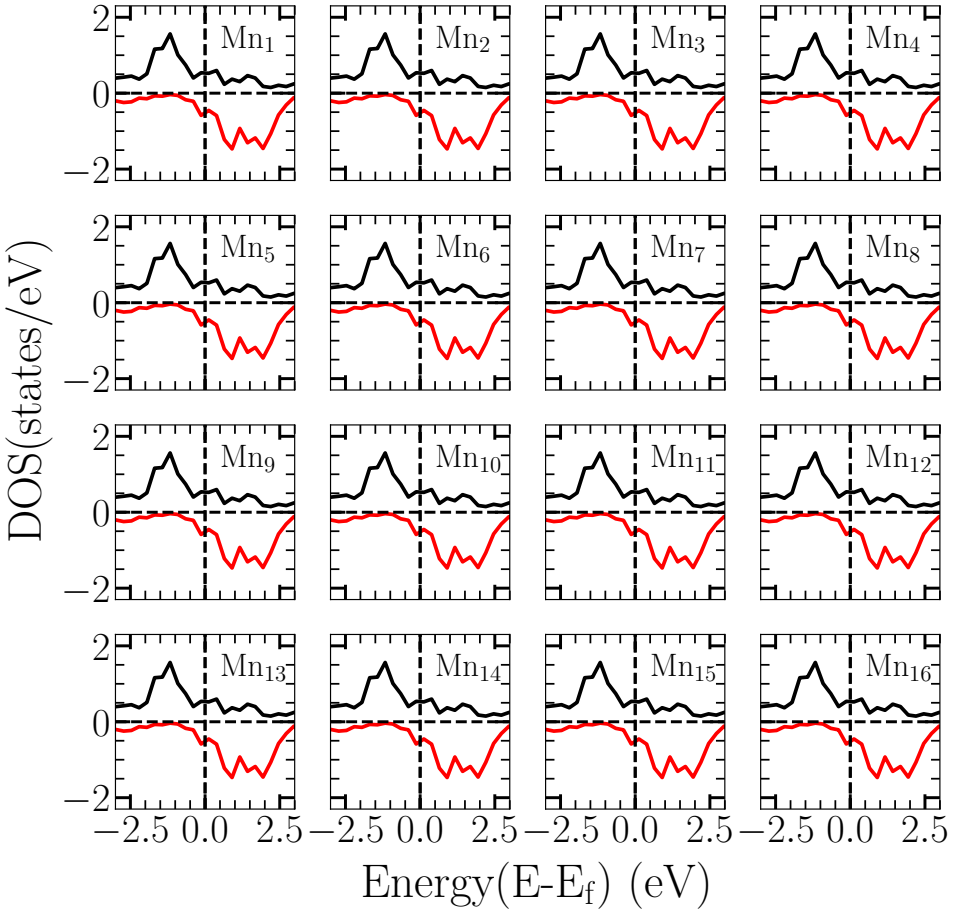

Figure 6.10: Projected Densities of States of each Mn atom in Ground State of $V_{1.0}Mn_{1.0}CO_2$

spin orientation affects the electronic structures of different atoms in different ways. That the anti-alignment of spins along c-axis has a profound effect on the electronic structure becomes clear from the electronic structures for the complete magnetically disordered state $\eta = 0$ (Figure 6.14(c)). We find that the total densities of states for both spin bands are very similar to that of the ground state. Total and Mn densities of states for $\eta = 0.5$ state of $V_{1.0}Mn_{1.0}CO_2$ are shown in Figure 6.15(c). In comparison with the ground state, We find substantial changes in both spin bands, for energies near Fermi level. The peak in the minority band and the valley, flanked by two peaks, at the Fermi level of the ground state, are absent in this partially disordered state. Densities of states of different Mn atoms undergo noticeable changes from the magnetically ordered ground state. The presence of anti-aligned spins for pairs of Mn forces a change in the exchange field each Mn atom is subjected to, resulting in changes in their electronic structures. When the magnetic disorder is complete ($\eta = 0$), there are further changes in the densities of states close to the Fermi level (Figure 6.15(c)). In case of $\eta = 0.5$ partial disordered state of $V_{0.5}Mn_{1.5}CO_2$ too, the electronic structure near Fermi level changes considerably (Figure 6.16(c)). The pseudo-gap in the minority spin band is now wider in comparison with the ground state. The peak around -1 eV next to the pseudo-gap observed in the ground state has now disappeared. In the complete disordered phase ($\eta = 0$), the electronic structure undergoes further modifications (Figure 6.16(f)). The changes are prominent in the minority spin band near Fermi level in the occupied part and in both spin bands in the unoccupied part. The electronic structures for other partially ordered magnetic states are shown in Figure 6.15 and Figure 6.16 for $V_{1.0}Mn_{1.0}CO_2$ and $V_{0.5}Mn_{1.5}CO_2$, show that there are only slight changes near Fermi level in most cases when η changes. It is also demonstrated that the ordering (or lack of it) of spins and not the number of spins with a particular orientation has a significant impact on the electronic structures. As an example, one can compare the ground state and $\eta = 0.66$ state of $V_{0.5}Mn_{1.5}CO_2$. The differences in the total densities of states between the ordered ground state and the partially ordered state (Figure 6.16(a) and (b)) are evident, even though both have the same number of spins aligned along c-direction. In a nutshell, the state of

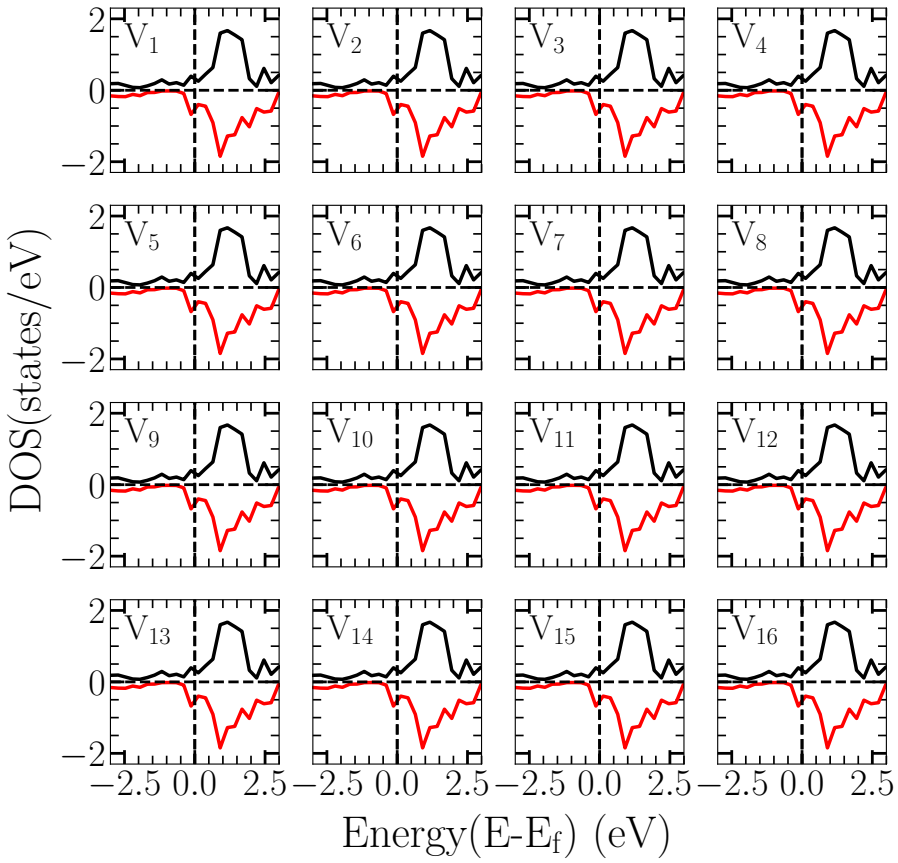

Figure 6.11: Projected Densities of States of each V atom in Ground State of $V_{1.0}Mn_{1.0}CO_2$

magnetic order has non-negligible effects on the electronic structures of $V_{2-x}Mn_xCO_2$ MXenes, particularly for the energies close to the Fermi level.

Magnetic disorder has non-negligible effects on the electronic structures of $V_{2-x}Mn_xCO_2$ MXenes, particularly for the energies close to the Fermi level. The changes in the electronic structures due to introduction of magnetic disorder should have effects on the Quantum capacitances of the chemically disordered compounds. In the next sub-section, we present results on this.

6.3.3 Effects of chemical and magnetic disorder on capacitances

In this section, we systematically discuss the changes in the quantum and electrical capacitance of $V_{2-x}Mn_xCO_2$ MXene electrodes when in contact with an acidic electrolyte like H_2SO_4. To this end, we discuss the variations in the integrated quantum capacitance (C_Q^{int}) over a voltage window ± 1 V for different x in the respective ground state. The results are shown in Figures 6.17(a)-(c). C_Q^{int} for non-magnetic states for each chemical composition are shown for the sake of comparison. C_Q^{int} are calculated at room temperature. The wiggled structure in the C_Q^{int} is an outcome of the modulations of the densities of states with the thermal broadening function (Equations (2.40)-(2.42)). We find that irrespective of composition, the maximum of C_Q^{int} occurs near 0V for the magnetic ground states. This is consistent with the fact that the changes in the electronic structures across the chemical degrees of the disorder occur near the Fermi level. Although qualitative behaviour similar to magnetic states is observed, the maxima of quantum capacitance for non-magnetic states are found to be higher than the magnetic states. Irrespective of the chemical composition, the maximum value increases with increasing x. However, this is due to the large densities of states at the Fermi level of non-magnetic states, which signify instability of the non-magnetic phases. The variations in the maximum C_Q^{int} with x for the magnetic ground state are non-monotonic. This is due to the fact that the magnetic ground states are different for different x. However, since the typical voltage window used in the experiments are rather narrow and may not include 0V, it is more useful to look for the maximum C_Q^{int} in the positive

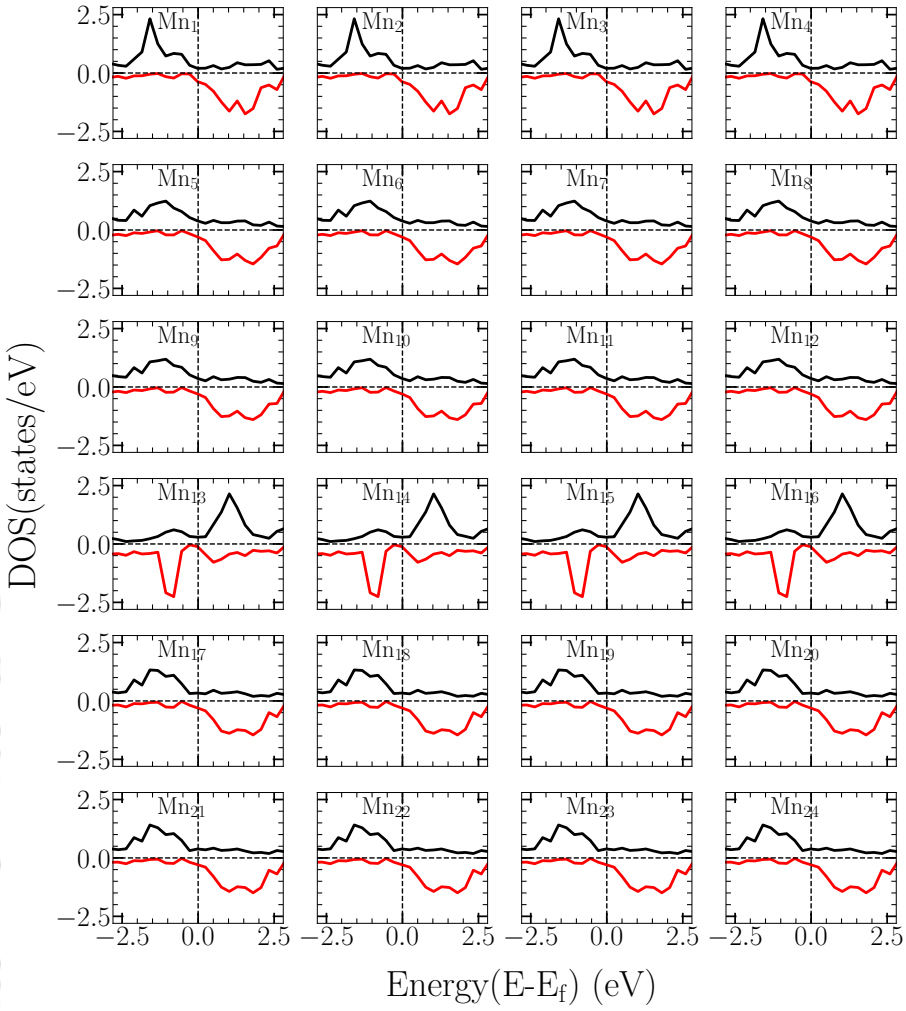

Figure 6.12: Projected Densities of States of each Mn atom in Ground State of $V_{0.5}Mn_{1.5}CO_2$

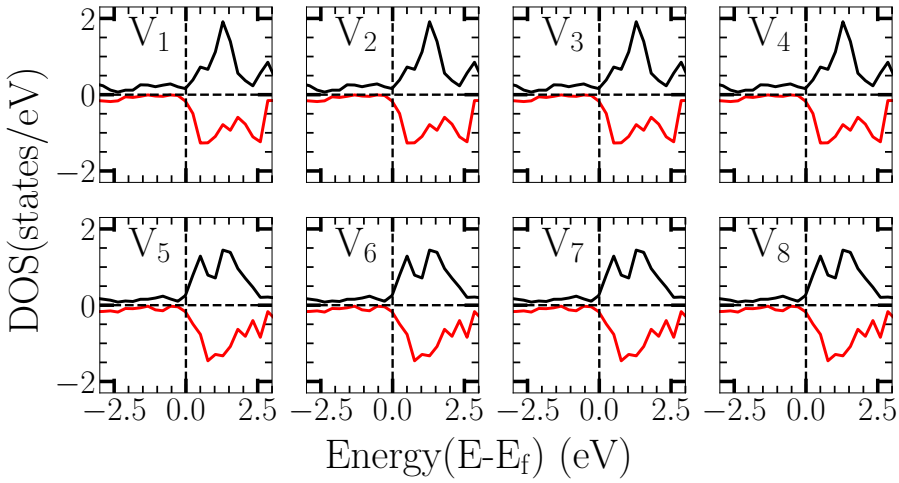

Figure 6.13: Projected Densities of States of each V atom in Ground State of $V_{0.5}Mn_{1.5}CO_2$

and negative voltage windows. Upon inspecting the variations in C_Q^{int} in two windows separately, we do not find any specific trend except that the maximum value of C_Q^{int} is 1500(2000) F/g in the negative(positive) voltage window. For all compositions, there is no specific magnetic state that can be singled out to be the provider of the highest value of C_Q^{int} as C_Q^{int} for all η states show similar wiggly behaviour in the chosen potential window.In fact, on the positive side of the voltage

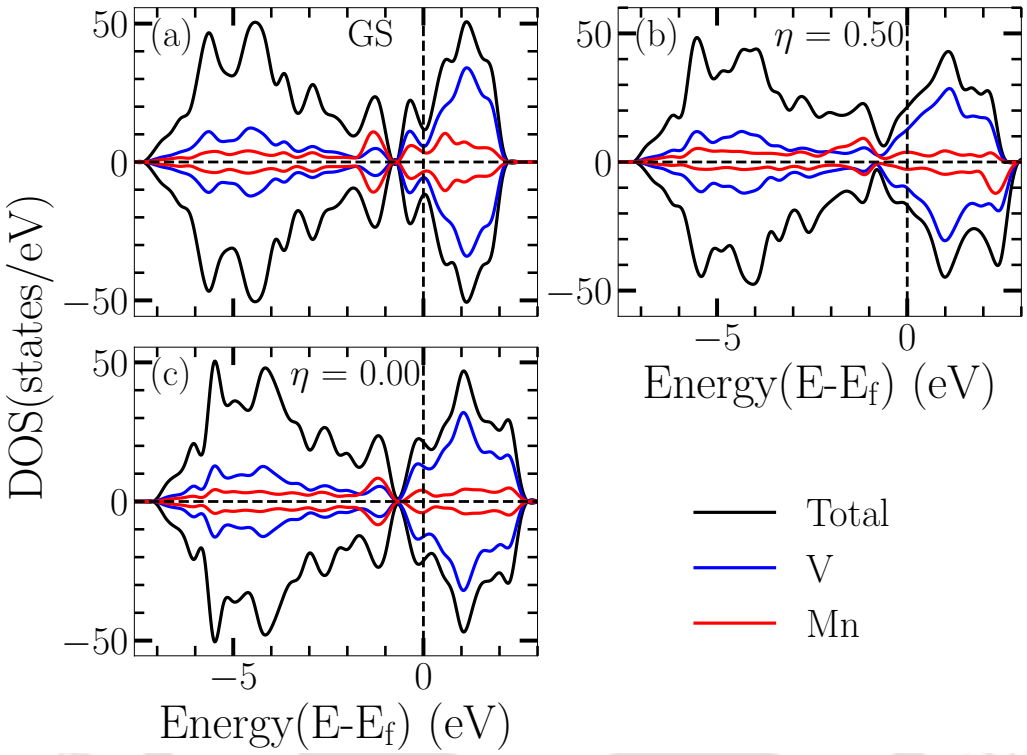

Figure 6.14: Total, Mn and V Densities of States of $V_{1.5}Mn_{0.5}CO_2$ in (a)Ground (GS), (b)η=0.5 and (c)η=0.0 states.

window, several partially ordered magnetic states along with the ground states have nearly the same maximum value of C_Q^{int}. Due to the lack of any clear trend over the entire voltage window, a more appropriate quantity to assess the potential best choice among these compounds is ΔC_Q^{int}, the difference between the maximum and minimum values of C_Q^{int}. The one with the least ΔC_Q^{int} is expected to be a better choice as one can then work with a larger voltage window. In Figure 6.18, we show ΔC_Q^{int} of $V_{2-x}Mn_xCO_2$ compound for the magnetically ordered ground state and various spin-disordered states associated with each value of x. The results show that the variations in the quantum capacitance over the entire voltage window are largest for the ground states of Mn-deficient and Mn-rich compounds, while the least variations are found for fully or near fully spin-disordered states. This implies that using these MXenes as electrodes can be advantageous if operated at higher temperatures.

The redox (C_{redox}) and electrochemical double layer (C_{EDL}) capacitances are calculated using equations (2.44)-(2.48). In the formalism used, the variations in the EDL capacitance are only due to the changes in the area of the electrode, which is estimated by the lattice parameter of the compound, as the other parameters (ϵ_0, ϵ_r =6 and d = 2.8) are constant for a given electrolyte. The calculated EDL capacitance of $V_{1.5}Mn_{0.5}CO_2$, $V_{1.0}Mn_{1.0}CO_2$, $V_{0.5}Mn_{1.5}CO_2$ is 55.78F/g, 56.70 F/g and 54.18 F/g, respectively. The surface redox contribution to the electrical capacitance, on the other hand, is expected to be significant with changes in chemical and magnetic disorder as different chemical and magnetic constitutions at the surfaces, along with variations in bond distances, should affect the surface charge transfer. In Figure 6.19(a),(b), and (c), variations in charge transfer (ΔQ), change in work-function (ΔWF), and C_{redox} with magnetic disorder for $V_{2-x}Mn_xCO_2$ are shown. The calculated values of these quantities demonstrate the following: (a) There is no significant change in C_{redox} and thus in C_E values of $V_{1.5}Mn_{0.5}CO_2$ and $V_{1.0}Mn_{1.0}CO_2$ as one changes the magnetic state from the ordered ground state to the complete spin disordered state. Thus, neither the chemical composition nor the spin disorder has any substantial effect on the electrical capacitances of these two compounds. The insensitivity in these quantities with regard to disorders is due to a near constant charge transfer and a maximum variation of 4% in ΔWF, (b) the case of Mn-rich composition $V_{0.5}Mn_{1.5}CO_2$ shows an anomaly. Here both ΔQ_{tot} and ΔWF for the ground state are significantly different from the values obtained for various magnetically disordered states of this particular compound. A larger charge transfer and a relatively smaller ΔWF in the

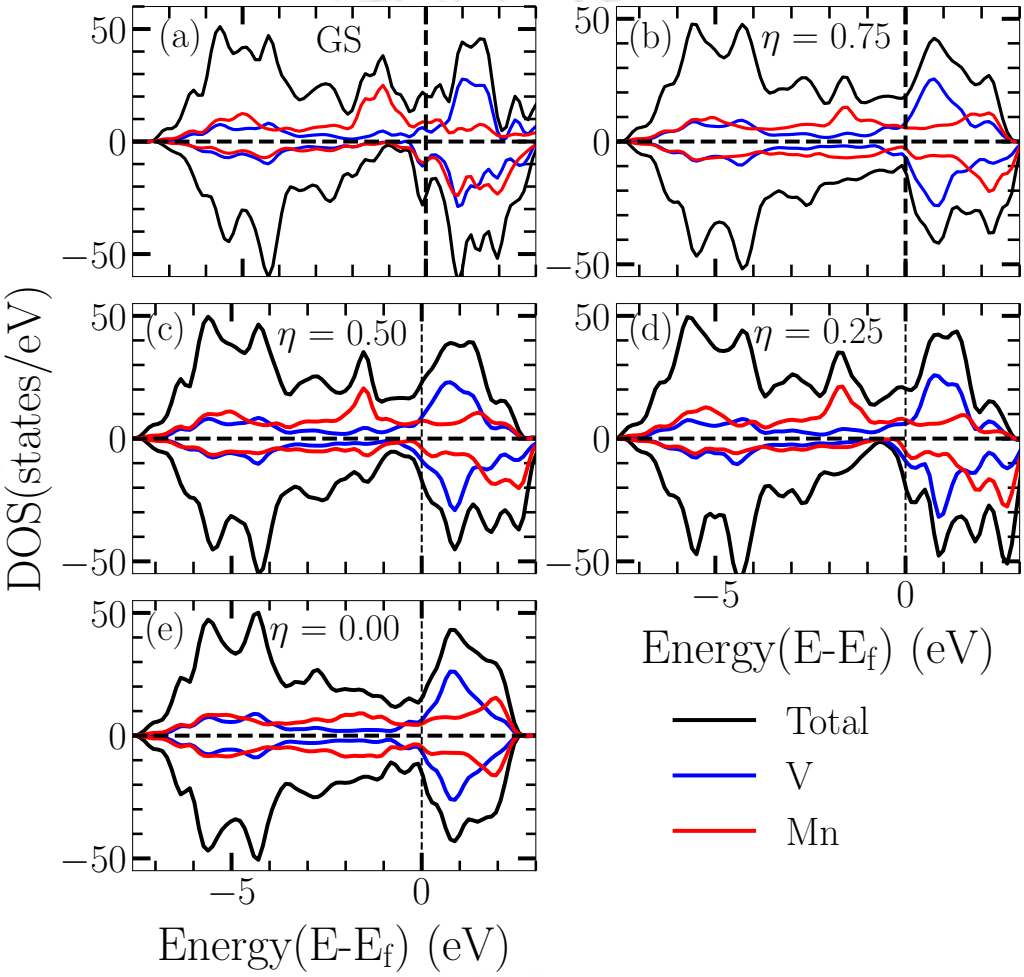

Figure 6.15: Total, Mn and V Densities of States of $V_{1.0}Mn_{1.0}CO_2$ in (a)Ground (GS), (b)η=0.75, (c)η=0.50, (d)η=0.25 and (e)η=0.00 states.

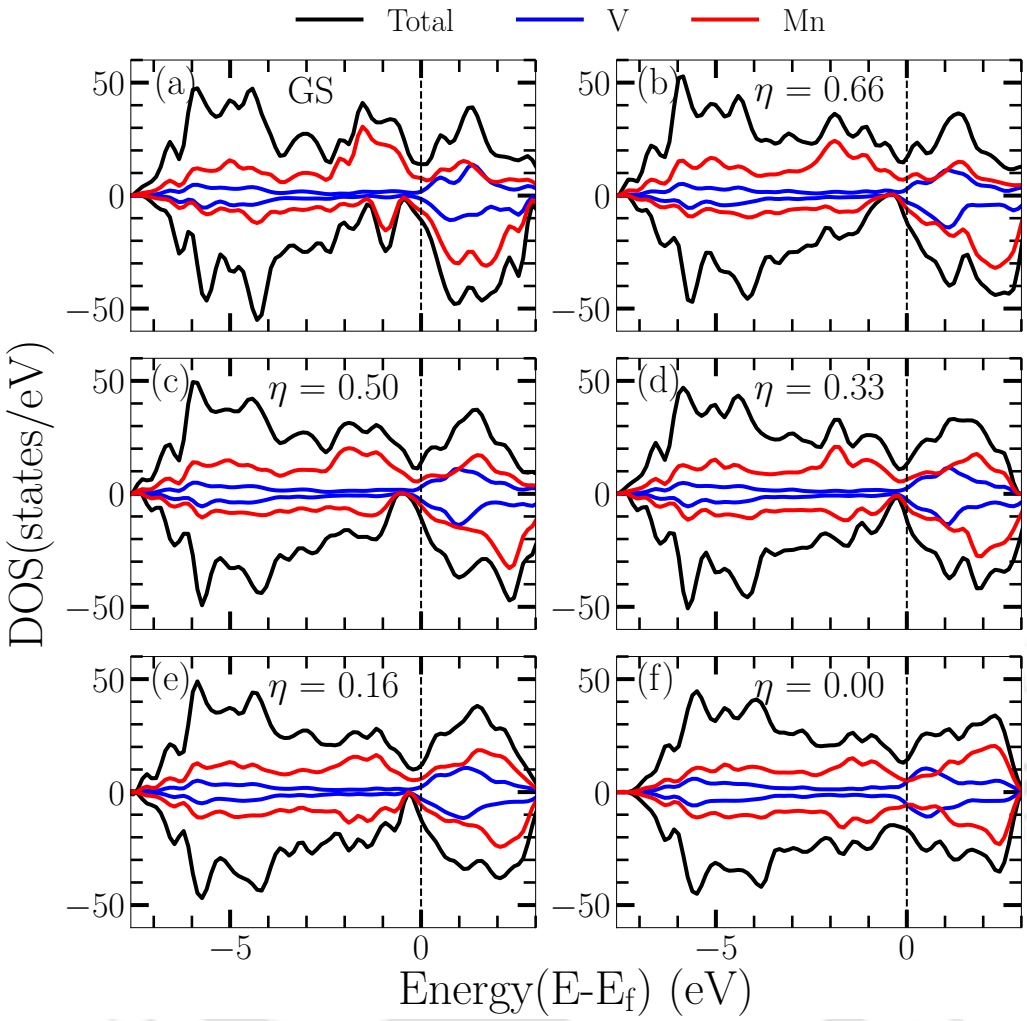

Figure 6.16: Total, Mn and V Densities of States of $V_{0.5}Mn_{1.5}CO_2$ in (a)Ground (GS), (b)η=0.66, (c)η=0.50, (d)η=0.33, (e)η=0.16, and (f)η=0.00 states.

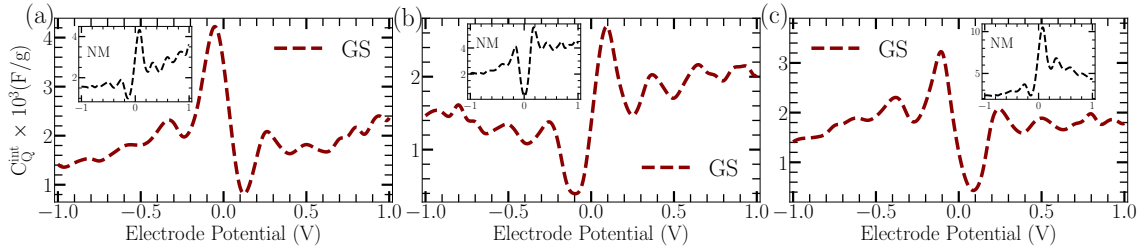

Figure 6.17: Integrated Quantum Capacitance (C_Q^{int}) of ground states of $V_{2-x}Mn_xCO_2$; x=0.5,1.0,1.5. Results for non-magnetic cases are shown in the respective insets.

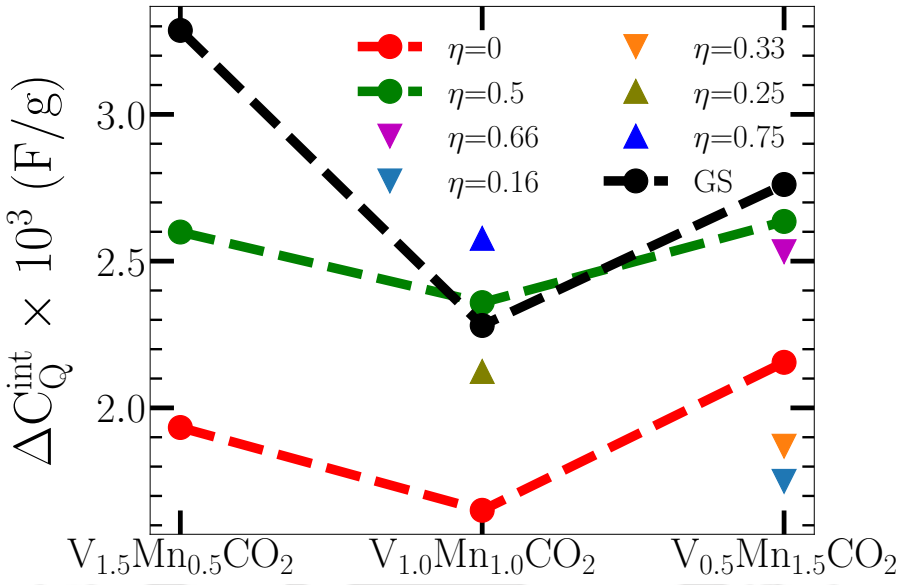

Figure 6.18: ΔC_Q^{int} for ground and various magnetic disordered (η) states of $V_{2-x}Mn_xCO_2$; x=0.5, 1.0 and 1.5.

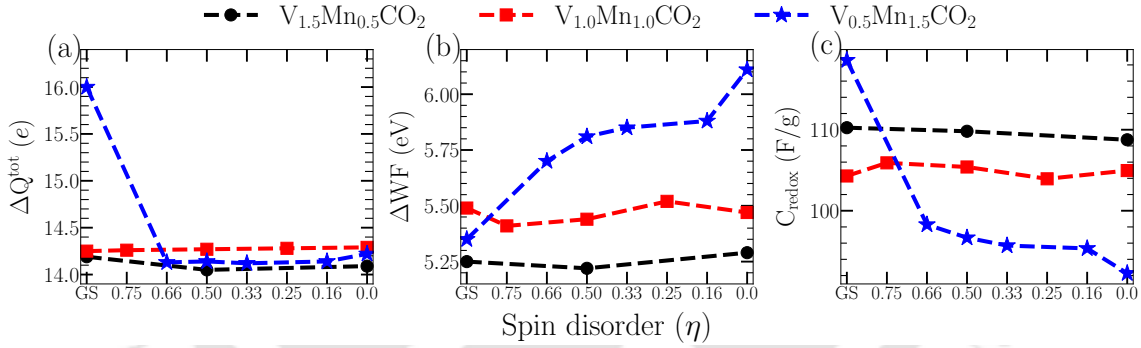

Figure 6.19: Variations in (a)charge transfer(ΔQ), (b)change in work-function(ΔWF) and (c)redox capacitance(C_{redox}) with spin disorder(η) for $V_{2-x}Mn_xCO_2$.

ground state produces a C_E value of 172 F/g, the highest among all cases considered. Moreover, C_{redox} for various η states are lower among all systems across compositions and magnetically disordered states. This is due to the fact that upon introduction of spin disorder in this compound ΔQ_{tot} decreases by about 2e; e the charge of the electron, and stays near constant with changes in the degree of spin disorder. Moreover, the ΔQ_{tot} values for the spin-disordered states are almost the same as those found in the other two compounds. On the other hand, ΔWF values are relatively high in comparison with those in the other two compounds along with a 7% variation among the magnetically disordered states. This variation is only 1% for the other two compounds. The root of this anomalous behavior lies in the magnetic constitution of the two MXene surfaces and will be discussed in the next subsection.

The total capacitance is calculated using equation (2.35). However, since C_Q is a function of the applied voltage while C_E is not, it is more appropriate to consider the average values of C_Q and hence C_T for each case. The averages of quantum(C^Q_{mean}) and total capacitance (C^T_{mean}) are calculated by taking the averages over the entire potential window considered here. The average values of the capacitances imply the most likely outcome of the experiments done within the voltage window. In Figure 6.20, we present C_E, C^Q_{mean} and C^T_{mean} as a function of the degree of spin disorder η for each one of the three compounds. We find that in all three compounds, the variations in the C^T_{mean} follow the trends in the C_E closely. This is understandable from the fact that C^Q_{mean} is one order of magnitude greater than C_E, and thus its role of it primarily is to reduce the total capacitance from its electrical capacitance value. The results demonstrate that while the C^T_{mean} in

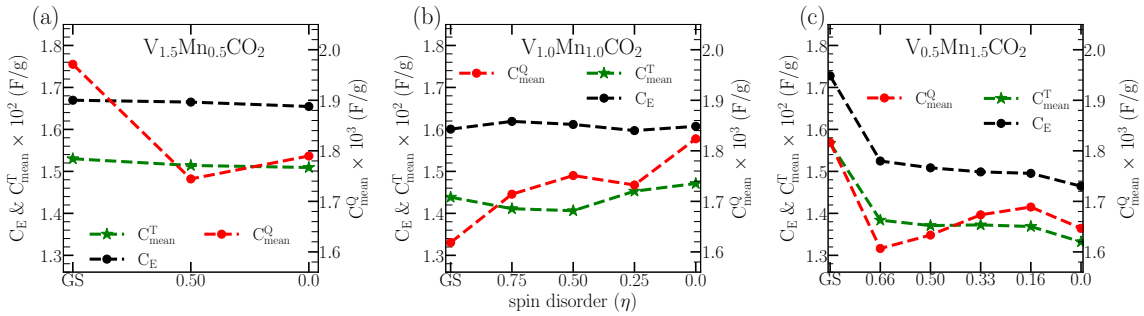

Figure 6.20: Variations in Electrical capacitance(C_E), mean quantum capacitance(C^Q_{mean}) and total capacitance(C^T_{mean}) with spin disorder(η) for $V_{2-x}Mn_xCO_2$.

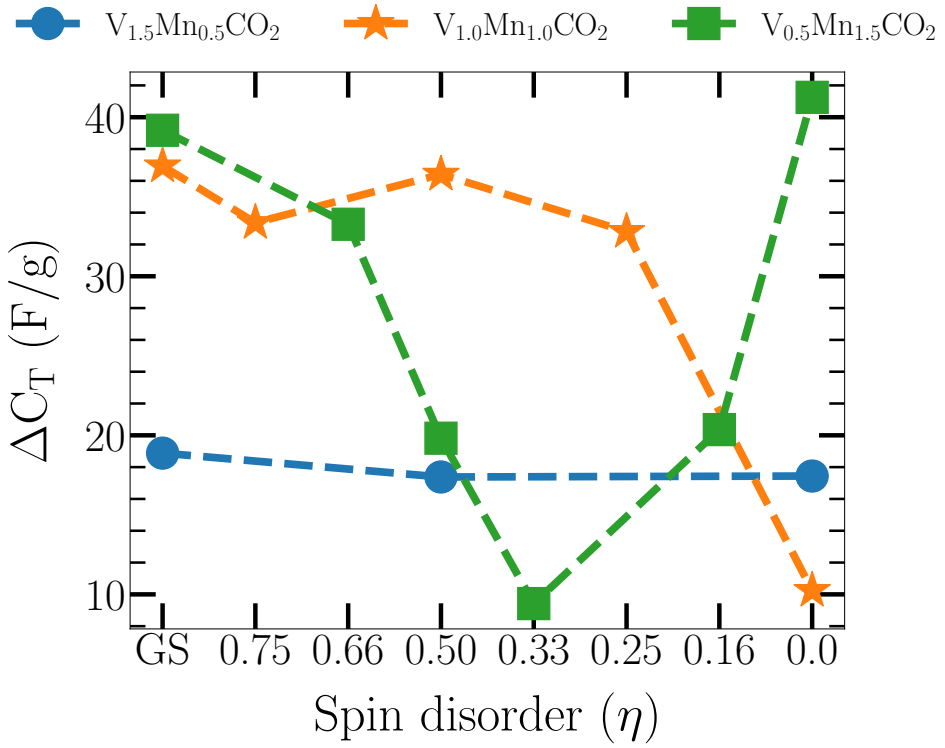

Figure 6.21: ΔC_T for the ground (GS) and different spin disordered (η) states of $V_{2-x}Mn_xCO_2$ (x=0.5,1.0,1.5).

$V_{1.5}Mn_{0.5}CO_2$ varies insignificantly with the spin disorder, the most significant variation is found in $V_{0.5}Mn_{1.5}CO_2$. The variations of C^T_{mean} in $V_{1.0}Mn_{1.0}CO_2$ is non-monotonic. The highest C^T_{mean} is obtained in the ground state of the Mn-rich compound.

In order to decide on the potential best choice for an electrode that has minimum fluctuation across the voltage window, we compute ΔC_T, the difference between the maximum and minimum values of C_T for each chemical and magnetic composition. The results are presented in Figure 6.21. The V-rich system has a low ΔC_T that is almost insensitive to the magnetic state. This means that it can be operated over a large range of temperatures. For the other two compounds, ΔC_T values lower than this is obtained. However, in order to exploit this trait, they have to be operated at specific spin-disordered states, that is at specific temperatures which can be considerably high. This poses a disadvantage in using $V_{1.0}Mn_{1.0}CO_2$ and $V_{0.5}Mn_{1.5}CO_2$ as electrodes in supercapacitors.

6.3.4 Anomalous electrochemical behaviour of $V_{0.5}Mn_{1.5}CO_2$

In order to understand the origin of the anomalous electrochemical behavior of $V_{0.5}Mn_{1.5}CO_2$, we perform a detailed analysis of the charge transfers through the two surfaces. The ground state surface magnetic structure of this compound is unique in the sense that, unlike the other two

Table 6.2: Charge on each element on the top surface of $V_{0.5}Mn_{1.5}CO_2$(Ground state) before and after hydrogenation. Transition metal - oxygen nearest neighbor bond distances (in Å) are also given.

Cluster color code(Figure 6.22(a))	Before hydrogenation Atom(charge (e))	After hydrogenation Atom(charge (e))	Atom pair (bond length)
orange	O_3(6.91)	O_3(7.31)	-
	Mn_3(11.58)	Mn_3(11.65)	O_3-Mn_3(1.95)
	Mn_7(11.60)	Mn_7(11.68)	O_3-Mn_7(1.92)
	Mn_9(11.60)	Mn_9(11.65)	O_3-Mn_9(1.92)
		H_3(0.45)	-
blue	O_7(6.94)	O_7(7.34)	-
	Mn_4(11.58)	Mn_4(11.65)	O_7-Mn_4(2.00)
	Mn_7(11.60)	Mn_7(11.68)	O_7-Mn_7(1.99)
	V_1(11.07)	V_1(11.42)	O_7-V_1(1.81)
	-	H_7(0.42)	-
black	O_9(6.94)	O_9(7.32)	-
	Mn_1(11.58)	Mn_1(11.65)	O_9-Mn_1(1.98)
	Mn_9(11.60)	Mn_9(11.65)	O_9-Mn_9(1.97)
	V_1(11.07)	V_1(11.42)	O_9-V_1(1.83)
	-	H_9(0.45)	-
red	O_{13}(6.88)	O_{13}(7.40)	-
	Mn_5(11.60)	Mn_5(11.68)	O_{13}-Mn_5(2.10)
	Mn_{10}(11.60)	Mn_{10}(11.65)	O_{13}-Mn_{10}(2.04)
	V_1(11.07)	V_1(11.07)	O_{13}-V_1(1.72)
	-	H_{13}(0.27)	-

compounds, in this case, the spin orientations of Mn atoms on the two surfaces are different. The charge transfers from the top and bottom surface of all compounds in any magnetic state, except this, are identical. While a charge of 7.05e -7.15e is transferred through the surfaces of all compounds, the numbers for this system are 9.648e and 6.352e for the top and bottom surfaces, respectively. This means that for the system in question, there is about 2.5e(1.5e) more(less) charge transfer from the top(bottom) surface in comparison to that for all other systems. To get more insight into this anomalous behavior, we have computed the Bader charges [140] on Mn,V and O atoms of both surfaces of $V_{0.5}Mn_{1.5}CO_2$ before (no-H) and after(full-H) hydrogenation and the results are shown in Tables 6.2(Top) and 6.3(Bottom). The results are shown for four non-equivalent atom clusters marked in Figure 6.22. Each cluster is denoted by a different colour.

From the computed Bader charges, we find that all V atoms had an identical charge of 11.07e before hydrogenation irrespective of which surface they occupy. After hydrogenation, there is a 0.09e charge more on the V atoms on the top surface. The Mn and C atoms are almost inert in the redox charge transfer through hydrogenation of the surfaces as the changes in the Mn (C) charges after hydrogenation are between 0.04e-0.07e (0.09e-0.12e) only. As expected the surface charge transfer happens through O atoms, and the largest changes in charge content happen for them. However, the results suggest that the amount of change depends on the location of the O atoms. The charge content on the O atoms on the top surface, due to hydrogenation, changes between 0.4e-0.52e, while for those on the bottom surface, it is between 0.2e-0.34e. The reason behind more charge transfer through the V atoms could be the rumpling structure of the surfaces in this compound. The rumpling pulls V surfaces closer to the O and thus the H atoms. This is clear from the V-O bond distances that vary between 1.72-1.83 Å whereas the Mn-O bond distances have a wider dispersion (1.92-2.11 Å). The substantially different charge transfer from two surfaces can be correlated with the magnetic environment around an atom on each surface in the ground state of $V_{0.5}Mn_{1.5}CO_2$. Among the O atoms in the bottom surface, O_{21}-O_{24} (brown block in Figure 6.22(b)) transfer only 0.17e upon hydrogenation. Each one of these four is networked with an Mn atom which has its spin aligned along -c-direction. The same is true for O_{25}-O_{28} (magenta block in Figure 6.22(b)) where only 0.19e electrons are transferred. On the other hand, O_{17}-O_{20} (green block in Figure 6.22(b)) are networked with 3 Mn out of which 2 have spins aligned along

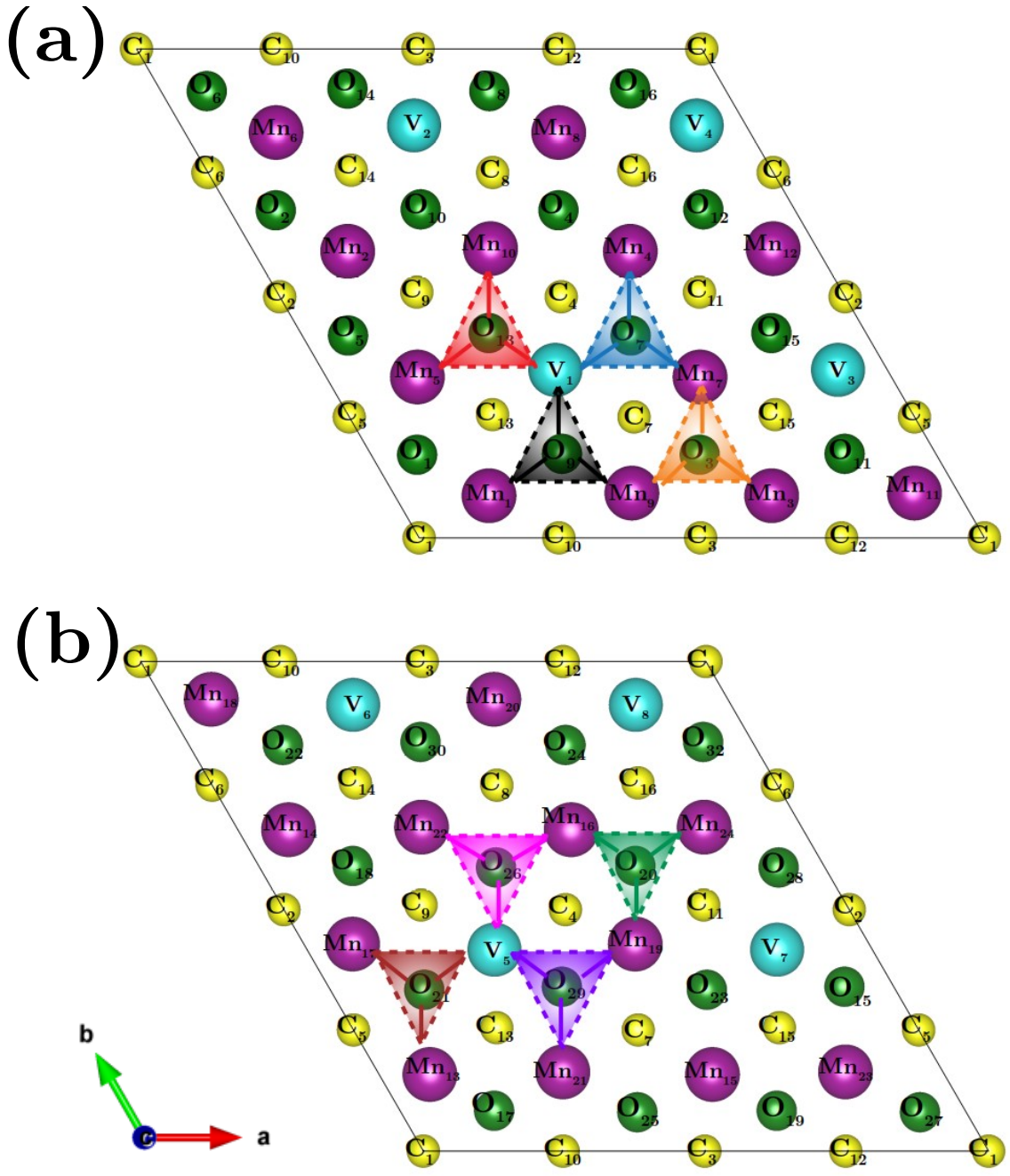

Figure 6.22: Top view of the atomic arrangements in (a)top and (b)bottom surfaces of $V_{0.5}Mn_{1.5}CO_2$. Non-equivalent clusters of atoms are highlighted with different colours

Table 6.3: Charge on each element on the bottom surface of $V_{0.5}Mn_{1.5}CO_2$(Ground state) before and after hydrogenation. Transition metal - oxygen nearest neighbor bond distances (in Å) are also given.

Cluster color code(Figure 6.22(b))	Before hydrogenation Atom(charge (e))	After hydrogenation Atom(charge (e))	Atom pair (bond length)
green	O_{20}(6.91)	O_{20}(7.24)	-
	Mn_{16}(11.68)	Mn_{16}(11.68)	O_{20}-Mn_{16}(1.93)
	Mn_{19}(11.60)	Mn_{19}(11.64)	O_{20}-Mn_{19}(1.92)
	Mn_{24}(11.58)	Mn_{24}(11.64)	O_{20}-Mn_{24}(1.92)
	-	H_{20}(0.51)	-
brown	O_{21}(6.93)	O_{21}(7.10)	-
	Mn_{13}(11.68)	Mn_{13}(11.68)	O_{21}-Mn_{13}(2.06)
	Mn_{17}(11.60)	Mn_{17}(11.64)	O_{21}-Mn_{17}(1.99)
	V_5(11.07)	V_1(11.31)	O_{21}-V_5(1.78)
	-	H_{21}(0.69)	-
magenta	O_{26}(6.91)	O_{26}(7.10)	-
	Mn_{16}(11.68)	Mn_{16}(11.68)	O_{26}-Mn_{16}(2.04)
	Mn_{22}(11.58)	Mn_{22}(11.64)	O_{26}-Mn_{22}(1.97)
	V_5(11.07)	V_5(11.31)	O_{26}-V_5(1.80)
	-	H_{26}(0.69)	-
violet	O_{29}(6.90)	O_{29}(7.20)	-
	Mn_{19}(11.60)	Mn_{19}(11.64)	O_{29}-Mn_{19}(2.05)
	Mn_{21}(11.58)	Mn_{21}(11.64)	O_{29}-Mn_{21}(2.04)
	V_5(11.07)	V_5(11.31)	O_{29}-V_5(1.75)
	-	H_{29}(0.51)	-

c-direction, the associated charge transfer is 0.33e. A charge transfer of 0.3e happens in case of O_{29}-O_{32} which are in a network with 2 Mn, both having spins aligned along c-direction. Therefore, the presence of at least two Mn having their spins aligned in the same direction enables more charge transfer through the O atoms. All Mn spins on the top surface are aligned in the same direction and the charge transfers associated with O atoms are more. The differences in the amounts of charge transfer for different groups of atoms can be explained through the variations in the transition metal neighborhood of the O atoms. A charge transfer of $0.4e$ occurs for atoms O_1-O_4 (orange block in Figure 6.22(a)). These O have three Mn atoms in their neighborhood. The numbers are 0.4-0.42e for O_5-O_{12}. Here the O are in a network of two Mn and one V atoms (blue and black blocks in Figure 6.22(a)) with Mn-O (V-O) bond distances of about 2.0 Å(1.8 Å). The largest charge transfer of $0.52e$ is associated with the remaining four oxygen (red block in Figure 6.22(a)) which have the same neighborhood of transition metals as O_5-O_{12} but the V-O distances are shorter (1.72 Å). The above analysis show that the substantially different charge transfer from different surfaces in the ground state of this system can be correlated with the magnetic environment around an atom. Since there is identical charge transfer from either surface in partial or fully disordered magnetic states for this compound, it appears that the non-uniformity in spin distribution on the chemically identical surfaces must be responsible for non-uniformity in the charge transfer. We have further examined this proposition by calculating the charge transfer from the surfaces by various combinations of magnetic configurations on the surfaces of $V_{0.5}Mn_{1.5}CO_2$. In Figure 6.23 the situations considered are shown schematically along with the charge transfer $\Delta Q_1(\Delta Q_2)$ from the top(bottom) surfaces. The ground state is shown in Figure 6.23(a) while two different situations with identical ordered configurations on both surfaces are shown in Figure 6.23 (b)-(c). In Figure 6.23(b), both surfaces are ferromagnetic, the replica of the top surface in the ground state. In Figure 6.23(c), both surfaces are replicas of the bottom surface in the ground state. In Figure 6.23(d), a completely different situation with the top surface having a complete spin disordered configuration ($\eta = 0$) and the bottom surface with a partial spin disordered configuration ($\eta = 0.33$) is depicted. It is to be noted that the number of spins aligned(anti-aligned) along(against) c-axis in $\eta = 0.33$ state is the same as that in the bottom surface in the ground state. When both surfaces are ferromagnetic, the charge transfer from both surfaces is identical and exactly the same as that from the top surface when the system is in the ground state (Figure 6.23). In situation (c), we find identical

charge transfer from both surfaces with a magnitude identical to that corresponding to the bottom surface in the ground state which has an identical spin configuration. From these results, two things appear to emerge. First, when the surfaces are identical in terms of the magnetic environment around an atom, the charge transfers are identical, and second, a ferromagnetic configuration promotes higher charge transfer while a ferrimagnetic ordered configuration promotes lower charge transfer in comparison with those in magnetically disordered states. The results obtained from the situation depicted in Figure 6.23(d), however, demonstrate that identical magnetic configuration on the surfaces is not a necessary condition for identical charge transfer from both surfaces. The charge transfer numbers in this configuration nevertheless confirm that when there is a mixture of aligned and anti-aligned spins (along c-direction), a random distribution leads to higher charge transfer. Since the chemical environment and structure around an atom are kept identical in all four situations discussed, the differences in charge transfer must be a consequence of different magnetic environments around an atom. In the ordered ferrimagnetic configuration considered here (Figure 6.23(c)), the environment around each atom follows a particular order but in the partially ordered situation denoted by $\eta = 0.33$, the order vanishes. That the ferromagnetic order promotes the highest charge transfer, is, however, seen only with this chemical composition. In the other two compounds, despite intra-surface order being ferromagnetic, we do not find charge transfer of this large amount. Therefore, the higher concentration of Mn should be the reason. The results, thus, imply the importance of both chemical and magnetic composition.

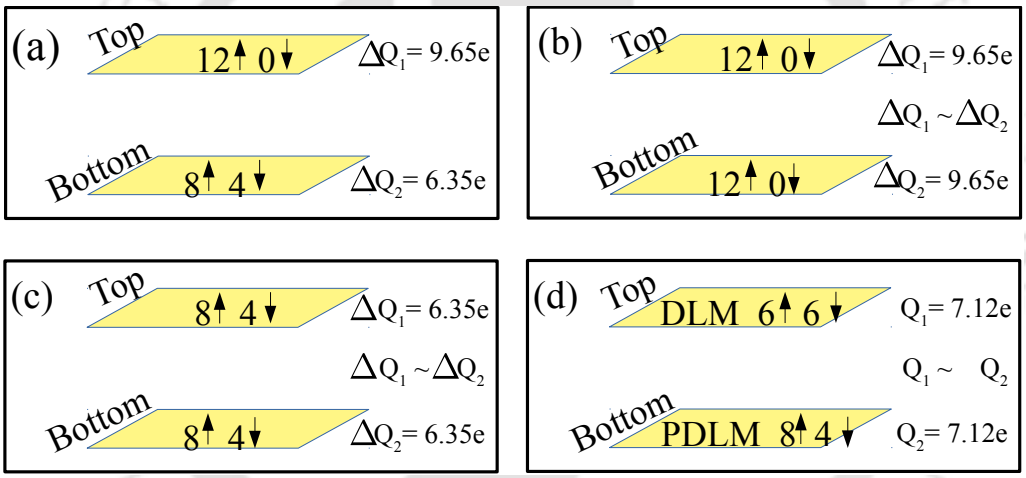

Figure 6.23: Schematic diagram showing various different magnetic structures on the top and bottom surface of $V_{0.5}Mn_{1.5}CO_2$ and corresponding charge transfer from them. (a) The ground state, (b) a situation where spins of all Mn atoms (top and bottom surface) are aligned along the c-axis, a replica of the top surface in the ground state, (c) a situation where spins of 8 Mn(4 Mn) atoms on both surfaces are aligned(anti-aligned) along the c-axis, a replica of the bottom surface in the magnetic ground state. (d) a situation where the top surface has a spin arrangement consistent with η=0.00 (complete spin disordered state) and the bottom surface spin arrangement is according to the partial magnetic disordered state denoted by η=0.33.

6.4 Conclusions

Using DFT based first-principles electronic structure calculations, we have explored in detail the effects of chemical and magnetic disorder on the capacitance of solid solution MXene $V_{2-x}Mn_xCO_2$ electrode in an electrode-acidic electrolyte supercapacitor setup. Although the material is yet to be exfoliated from its precursor MAX phase, we have considered this as a test case to address the yet unexplored issues of disorder effects on its charge storage capacity. We have systematically computed various contributions to the total capacitance with changes in the chemical composition and magnetic structure. We find that (a) the ground state magnetic structure is dependent upon the chemical composition (b) the total capacitance does not vary significantly with changes in chemical and magnetic order (c) the total capacitance of this material is comparable to the capacitance of $Ti_3C_2O_2$, the most extensively studied MXene for supercapacitor application and (d) the minimum

and constant variation in the total capacitance with the variation of spin disorder is obtained for $V_{1.5}Mn_{0.5}CO_2$, a trait that is most useful for operational purpose. In the course of our investigation, we have also found anomalous behavior in surface charge transfer. The asymmetric magnetic configurations on two surfaces lead to significantly different charge transfers from different surfaces affecting the redox capacitance. We find that the inhomogeneity in the magnetic structure across surfaces affects the charge transfer mutually. The most important finding is that in this composition only, ferromagnetic configuration promotes a significantly high charge transfer and thus a substantially large capacitance can be achieved by designing the system with both surfaces having ferromagnetic order. This is a new phenomenon hitherto not reported in the literature. This can have a profound effect on tuning the capacitance of the electrode by manipulating the magnetic structure of the MXene surfaces. However, a microscopic understanding of the phenomenon as well as the reason behind different magnetic ground states for different chemical compositions of (V-Mn)CO_2 MXene are beyond the scope of this work and remains a matter of future endeovour.

Chapter 7

Summary and Future Directions

7.1 Summary

In this dissertation, we have explored the electrochemical performances of MXenes as supercapacitor electrodes. The electrochemical performance is one of the primary applications of MXene, researched extensively. This thesis provides a systematic understanding of the charging mechanisms in MXenes based supercapacitors. The vital consideration in this thesis is the inclusion of quantum capacitance in computing the total capacitance of MXenes. We have shown that consideration of quantum capacitances gives a closer estimate of total capacitance to the experimental result. We have used two approaches to compute the electrical capacitance of considered MXenes, namely RBA and Solvation methods. The solvation method gives a more accurate estimation of electrical capacitance than RBA, as it implicitly considers the effect of the electrode/electrolyte interface. The Solvation method requires more computation power and is more time-consuming than the RBA method. On the other hand, RBA provides qualitative insights into the charge storage when the system contains a massive number of atoms.

In Chapter 3, we investigated the electrochemical performance of several M_2C and M_3C_2 MXene in pristine and -O functional forms. We explained the reasoning behind one order higher C_{redox} value of pristine MXene compared to -O functional ones. Our findings from this work are the following: first, all the considered compounds will display excellent capacitive behavior if used as negative electrodes; second, although the transition metal constituents in the compounds considered are chosen from both $3d$ and $4d$ series, there is hardly any noticeable difference or a trend in their relative behaviors as far as the capacitances are considered; third, we find $Nb_{n+1}C_n$ as another potential negative electrode that can be used in a supercapacitor.

In Chapter 4, we have compared the impact of doping and substitution in enhancing the electrochemical performance of $Ti_3C_2T_x$. We found that doping of N at the functional site is the most effective as it enhances the surface redox activity compared to the undoped and LS-doped ones. Our quantitative results suggest that the surface redox activity is primarily responsible for the electrochemical parameters of the pristine and doped systems, although the EDL mechanism competes with it. The two mechanisms act against each other and influence the capacitance's overall charge storage. With the increase in nitrogen content such that it substitutes 50% carbon from the lattice site, the capacitance value degrades. It further degrades upon substituting the surface Ti atoms with more electronegative Mo. These are yet to be verified through electrochemical measurements, although both compounds have been synthesized.

In Chapter 5, we introduced Janus-MM′C MXenes as promising supercapacitor electrodes. Enhanced charge storage capacity is observed for Janus MXene due to enhanced surface redox activity. The reason behind such enhancements lies in the rapid changes in the charge states of the transition metal constituents forming the Janus. The formation of Janus breaks the symmetry of M_2C MXenes and affects the electronic structures of the constituents substantially. This, in turn, affects the charge states. The degree of variation in the charge states decides the quantum of increment in redox capacitance. This work throws a reasonable amount of light on the role of surface engineering and the chemistry of materials in the context of energy storage devices.

In Chapter 6, we have studied the effect of chemical and magnetic disorders on the electrochemical performance of solid solution $V_{2-x}Mn_xCO_2$ MXene. We have systematically computed various contributions to the total capacitance with changes in the chemical composition and magnetic

structure. We find that (a) the ground state magnetic structure is dependent upon the chemical composition (b) the total capacitance does not vary significantly with changes in chemical and magnetic order (c) the total capacitance of this material is comparable to the capacitance of $Ti_3C_2O_2$, the most extensively studied MXene for supercapacitor application and (d) the minimum and constant variation in the total capacitance with the variation of spin disorder is obtained for $V_{1.5}Mn_{0.5}CO_2$, a trait that is useful for operational purpose. During our investigation, we have also found anomalous behavior of surface charge transfer in $V_{0.5}Mn_{1.5}CO_2$. The asymmetric magnetic configurations on two surfaces lead to significantly different charge transfers from other surfaces, affecting the redox capacitance. The inhomogeneity in the magnetic structure across surfaces affects the charge transfer mutually. The most important finding is that in this composition only, ferromagnetic configuration promotes a significantly high charge transfer, and thus, a substantially large capacitance can be achieved by designing the system with both surfaces having ferromagnetic order.
In Chapter 7, we have discussed the summary of this thesis, followed by the scope for further work.

7.2 Future Directions

This thesis provides several routes for more further research that can be taken up further. Following are some of the avenues that can be explored.

1. A more accurate effect of applied electrode potential on EDL and quantum capacitances can be simulated using classical molecular dynamics. The EDL and quantum capacitance vary during charging/discharging. The molecular dynamics simulation helps capture those changes with time.

2. The 'RBA method' and 'Solvation method' are specific to H_2SO_4 electrolyte. In reality, basic and organic electrolytes are used for experimental purposes. One can develop approaches to calculate electrical capacitance considering basic and organic electrolytes.

3. This thesis considers the homogeneous functionalization of -O and -OH groups. However, in reality, -F, -Cl, -O, and -OH groups get adsorbed over the MXene surfaces with varying compositions. One can model MXene structures such that all functional groups passivate the surfaces. Studying the effect of different compositions of functional groups on electrochemical performances would be interesting.

4. We have introduced Janus MXene as a potential electrode for supercapacitors. Those MXenes can also be explored as battery electrodes. We have constructed Janus MXene with different M metals. However, one can imagine building Janus with different functional elements on the two surfaces. As the redox activity is a surface effect, playing with other surface functional elements could give rise to exciting phenomena with regard to charge storage capacities.

5. The effects of chemical disorder can be explained in more details on a number of MXenes that are synthesized lately.

Bibliography

[1] Howard I Becker. Low voltage electrolytic capacitor, July 23 1957. US Patent 2,800,616.

[2] Anetta Platek-Mielczarek, Joanna Conder, Krzysztof Fic, and Camelia Matei Ghimbeu. Performance evaluation of electrochemical capacitors with activated carbon spheres as electrode material and aqueous electrolyte. *Journal of Power Sources*, 542:231714, 2022.

[3] L Fekri Aval, M Ghoranneviss, and G Behzadi Pour. High-performance supercapacitors based on the carbon nanotubes, graphene and graphite nanoparticles electrodes. *Heliyon*, 4(11), 2018.

[4] Sicong Tan, Jiajia Li, Lijie Zhou, Peng Chen, Jiangtao Shi, and Zhaoyang Xu. Modified carbon fiber paper-based electrodes wrapped by conducting polymers with enhanced electrochemical performance for supercapacitors. *Polymers*, 10(10):1072, 2018.

[5] Yoon Jae Lee, Gil-Pyo Kim, Yongju Bang, Jongheop Yi, Jeong Gil Seo, and In Kyu Song. Activated carbon aerogel containing graphene as electrode material for supercapacitor. *Materials Research Bulletin*, 50:240–245, 2014.

[6] Jen-Chun Chou, Yu-Liang Chen, Min-Han Yang, Yu-Ze Chen, Chih-Chung Lai, Hsin-Tien Chiu, Chi-Young Lee, Yu-Lun Chueh, and Jon-Yiew Gan. Ruo 2/mno 2 core–shell nanorods for supercapacitors. *Journal of Materials Chemistry A*, 1(31):8753–8758, 2013.

[7] Minghao Yu, Wang Wang, Cheng Li, Teng Zhai, Xihong Lu, and Yexiang Tong. Scalable self-growth of ni@ nio core-shell electrode with ultrahigh capacitance and super-long cyclic stability for supercapacitors. *NPG Asia materials*, 6(9):e129–e129, 2014.

[8] Xu Yu, Sul Ki Park, Sun-Hwa Yeon, and Ho Seok Park. Three-dimensional, sulfur-incorporated graphene aerogels for the enhanced performances of pseudocapacitive electrodes (vol 278, pg 484, 2015). *Journal of Power Sources*, 283:328–328, 2015.

[9] Qingqing Ke and John Wang. Graphene-based materials for supercapacitor electrodes–a review. *Journal of Materiomics*, 2(1):37–54, 2016.

[10] Michael Naguib, Murat Kurtoglu, Volker Presser, Jun Lu, Junjie Niu, Min Heon, Lars Hultman, Yury Gogotsi, and Michel W Barsoum. Two-dimensional nanocrystals produced by exfoliation of ti3alc2. *Advanced materials*, 23(37):4248–4253, 2011.

[11] Maria R Lukatskaya, Michael Ghidiu, Olha Mashtalir, Chang E Ren, Meng-Qiang Zhao, Yohan Dall'Agnese, Michel W Barsoum, and Yury Gogotsi. High volumetric capacitance and mechanisms of electrochemical charge storage in two-dimensional ti3c2-based mxene. In *Electrochemical Society Meeting Abstracts 227*, number 1, pages 202–202. The Electrochemical Society, Inc., 2015.

[12] Minmin Hu, Zhaojin Li, Tao Hu, Shihao Zhu, Chao Zhang, and Xiaohui Wang. High-capacitance mechanism for ti3c2 t x mxene by in situ electrochemical raman spectroscopy investigation. *ACS nano*, 10(12):11344–11350, 2016.

[13] Michel W Barsoum. The mn+ 1axn phases: A new class of solids: Thermodynamically stable nanolaminates. *Progress in solid state chemistry*, 28(1-4):201–281, 2000.

[14] Miladin Radovic and Michel W Barsoum. Max phases: bridging the gap between metals and ceramics. *American Ceramics Society Bulletin*, 92(3):20–27, 2013.

[15] Tamer El-Raghy and Michel W Barsoum. Diffusion kinetics of the carburization and silicidation of ti 3 sic 2. *Journal of Applied Physics*, 83(1):112–119, 1998.

[16] Michel W Barsoum, T El-Raghy, L Farber, M Amer, R Christini, and A Adams. The topotactic transformation of ti3sic2 into a partially ordered cubic ti (c 0.67 si0. 06) phase by the diffusion of si into molten cryolite. *Journal of the Electrochemical Society*, 146(10):3919, 1999.

[17] T El-Raghy, MW Barsoum, and M Sika. Reaction of al with ti3sic2 in the 800–1000 c temperature range. *Materials Science and Engineering: A*, 298(1-2):174–178, 2001.

[18] Michael Ghidiu, Maria R Lukatskaya, Meng-Qiang Zhao, Yury Gogotsi, and Michel W Barsoum. Conductive two-dimensional titanium carbide 'clay'with high volumetric capacitance. *Nature*, 516(7529):78–81, 2014.

[19] Valeria Nicolosi, Manish Chhowalla, Mercouri G Kanatzidis, Michael S Strano, and Jonathan N Coleman. Liquid exfoliation of layered materials. *Science*, 340(6139):1226419, 2013.

[20] Maxim Sokol, Varun Natu, Sankalp Kota, and Michel W Barsoum. On the chemical diversity of the max phases. *Trends in Chemistry*, 1(2):210–223, 2019.

[21] Michael Naguib, Michel W Barsoum, and Yury Gogotsi. Ten years of progress in the synthesis and development of mxenes. *Advanced Materials*, 33(39):2103393, 2021.

[22] Babak Anasori, Michael Naguib, and Guest Editors. Two-dimensional mxenes. *MRS Bulletin*, 48(3):238–244, 2023.

[23] Joseph Halim, Sankalp Kota, Maria R Lukatskaya, Michael Naguib, Meng-Qiang Zhao, Eun Ju Moon, Jeremy Pitock, Jagjit Nanda, Steven J May, Yury Gogotsi, et al. Synthesis and characterization of 2d molybdenum carbide (mxene). *Advanced Functional Materials*, 26(18):3118–3127, 2016.

[24] Jie Zhou, Xianhu Zha, Fan Y Chen, Qun Ye, Per Eklund, Shiyu Du, and Qing Huang. A two-dimensional zirconium carbide by selective etching of al3c3 from nanolaminated zr3al3c5. *Angewandte Chemie International Edition*, 55(16):5008–5013, 2016.

[25] Weichen Hong, Brian C Wyatt, Srinivasa Kartik Nemani, and Babak Anasori. Double transition-metal mxenes: Atomistic design of two-dimensional carbides and nitrides. *Mrs Bulletin*, 45(10):850–861, 2020.

[26] David Pinto, Babak Anasori, Hemesh Avireddy, Christopher E Shuck, Kanit Hantanasirisakul, Grayson Deysher, Joan Ramon Morante, William Porzio, Husam N Alshareef, and Yury Gogotsi. Synthesis and electrochemical properties of 2d molybdenum vanadium carbides–solid solution mxenes. *Journal of Materials Chemistry A*, 8(18):8957–8968, 2020.

[27] Grayson Deysher, Christopher Eugene Shuck, Kanit Hantanasirisakul, Nathan C Frey, Alexandre C Foucher, Kathleen Maleski, Asia Sarycheva, Vivek B Shenoy, Eric A Stach, Babak Anasori, et al. Synthesis of mo4valc4 max phase and two-dimensional mo4vc4 mxene with five atomic layers of transition metals. *ACS nano*, 14(1):204–217, 2019.

[28] Marley Downes, Christopher Shuck, Robert Lord, Mark Anayee, Mikhail Shekhirev, Ruocun Wang, Tetiana Hryhorchuk, Martin Dahlqvist, Johanna Rosen, and Yury Gogotsi. M5x4-a family of mxenes. 2023.

[29] Srinivasa Kartik Nemani, Bowen Zhang, Brian C Wyatt, Zachary D Hood, Sukriti Manna, Rasoul Khaledialidusti, Weichen Hong, Michael G Sternberg, Subramanian KRS Sankaranarayanan, and Babak Anasori. High-entropy 2d carbide mxenes: Tivnbmoc3 and tivcrmoc3. *ACS nano*, 15(8):12815–12825, 2021.

[30] Jie Zhou, Quanzheng Tao, Bilal Ahmed, Justinas Palisaitis, Ingemar Persson, Joseph Halim, Michel W Barsoum, Per OÅ Persson, and Johanna Rosen. High-entropy laminate metal carbide (max phase) and its two-dimensional derivative mxene. *Chemistry of Materials*, 34(5):2098–2106, 2022.

[31] Teng Zhang, Christopher E Shuck, Kateryna Shevchuk, Mark Anayee, and Yury Gogotsi. Synthesis of three families of titanium carbonitride mxenes. *Journal of the American Chemical Society*, 2023.

[32] Michael Naguib, Olha Mashtalir, Joshua Carle, Volker Presser, Jun Lu, Lars Hultman, Yury Gogotsi, and Michel W Barsoum. Two-dimensional transition metal carbides. *ACS nano*, 6(2):1322–1331, 2012.

[33] Murat Kurtoglu, Michael Naguib, Yury Gogotsi, and Michel W Barsoum. First principles study of two-dimensional early transition metal carbides. *Mrs Communications*, 2:133–137, 2012.

[34] Jeremy Come, Yu Xie, Michael Naguib, Stephen Jesse, Sergei V Kalinin, Yury Gogotsi, Paul RC Kent, and Nina Balke. Nanoscale elastic changes in 2d ti3c2tx (mxene) pseudocapacitive electrodes. *Advanced Energy Materials*, 6(9):1502290, 2016.

[35] Longhua Li. Lattice dynamics and electronic structures of ti3c2o2 and mo2tic2o2 (mxenes): The effect of mo substitution. *Computational Materials Science*, 124:8–14, 2016.

[36] Alexey Lipatov, Mohamed Alhabeb, Haidong Lu, Shuangshuang Zhao, Michael J Loes, Nataliia S Vorobeva, Yohan Dall'Agnese, Yu Gao, Alexei Gruverman, Yury Gogotsi, et al. Electrical and elastic properties of individual single-layer nb4c3tx mxene flakes. *Advanced Electronic Materials*, 6(4):1901382, 2020.

[37] Vadym N Borysiuk, Vadym N Mochalin, and Yury Gogotsi. Bending rigidity of two-dimensional titanium carbide (mxene) nanoribbons: A molecular dynamics study. *Computational Materials Science*, 143:418–424, 2018.

[38] Mohammad Khazaei, Ahmad Ranjbar, Masao Arai, Taizo Sasaki, and Seiji Yunoki. Electronic properties and applications of mxenes: a theoretical review. *Journal of Materials Chemistry C*, 5(10):2488–2503, 2017.

[39] Yu Xie and PRC Kent. Hybrid density functional study of structural and electronic properties of functionalized ti n+ 1 x n (x= c, n) monolayers. *Physical Review B*, 87(23):235441, 2013.

[40] Babak Anasori, Yu Xie, Majid Beidaghi, Jun Lu, Brian C Hosler, Lars Hultman, Paul RC Kent, Yury Gogotsi, and Michel W Barsoum. Two-dimensional, ordered, double transition metals carbides (mxenes). *ACS nano*, 9(10):9507–9516, 2015.

[41] Mohammad Khazaei, Masao Arai, Taizo Sasaki, Chan-Yeup Chung, Natarajan S Venkataramanan, Mehdi Estili, Yoshio Sakka, and Yoshiyuki Kawazoe. Novel electronic and magnetic properties of two-dimensional transition metal carbides and nitrides. *Advanced Functional Materials*, 23(17):2185–2192, 2013.

[42] Panpan Gao, Minhui Song, Xiaoxu Wang, Qing Liu, Shizhen He, Ye Su, and Ping Qian. Theoretical study on the electronic structure and magnetic properties regulation of janus structure of m'mco2 2d mxenes. *Nanomaterials*, 12(3):556, 2022.

[43] Xilin Zhang, Chang Xu, Yiying Zhang, Cheng Cheng, Zongxian Yang, and Kersti Hermansson. Regulation of co oxidation with pd additives on nb2co2 mxene. *International Journal of Hydrogen Energy*, 46(12):8477–8485, 2021.

[44] Dandan Sun, Qianku Hu, Jinfeng Chen, Xinyu Zhang, Libo Wang, Qinghua Wu, and Aiguo Zhou. Structural transformation of mxene (v2c, cr2c, and ta2c) with o groups during lithiation: a first-principles investigation. *ACS applied materials & interfaces*, 8(1):74–81, 2016.

[45] Hongming Weng, Ahmad Ranjbar, Yunye Liang, Zhida Song, Mohammad Khazaei, Seiji Yunoki, Masao Arai, Yoshiyuki Kawazoe, Zhong Fang, and Xi Dai. Large-gap two-dimensional topological insulator in oxygen functionalized mxene. *Physical Review B*, 92(7):075436, 2015.

[46] Mohammad Khazaei, Ahmad Ranjbar, Masao Arai, and Seiji Yunoki. Topological insulators in the ordered double transition metals m 2 m c 2 mxenes (m= mo, w; m = ti, zr, hf). *Physical Review B*, 94(12):125152, 2016.

[47] Chen Si, Kyung-Hwan Jin, Jian Zhou, Zhimei Sun, and Feng Liu. Large-gap quantum spin hall state in mxenes: d-band topological order in a triangular lattice. *Nano letters*, 16(10):6584–6591, 2016.

[48] Ali Shayesteh Zeraati, Seyyed Alireza Mirkhani, Pengcheng Sun, Michael Naguib, Paul V Braun, and Uttandaraman Sundararaj. Improved synthesis of ti 3 c 2 t x mxenes resulting in exceptional electrical conductivity, high synthesis yield, and enhanced capacitance. *Nanoscale*, 13(6):3572–3580, 2021.

[49] Yuanyue Liu, Hai Xiao, and William A Goddard III. Schottky-barrier-free contacts with two-dimensional semiconductors by surface-engineered mxenes. *Journal of the American Chemical Society*, 138(49):15853–15856, 2016.

[50] Qing Tang, Zhen Zhou, and Panwen Shen. Are mxenes promising anode materials for li ion batteries? computational studies on electronic properties and li storage capability of ti3c2 and ti3c2x2 (x= f, oh) monolayer. *Journal of the American Chemical Society*, 134(40):16909–16916, 2012.

[51] Yu Xie, Michael Naguib, Vadym N Mochalin, Michel W Barsoum, Yury Gogotsi, Xiqian Yu, Kyung-Wan Nam, Xiao-Qing Yang, Alexander I Kolesnikov, and Paul RC Kent. Role of surface structure on li-ion energy storage capacity of two-dimensional transition-metal carbides. *Journal of the American Chemical Society*, 136(17):6385–6394, 2014.

[52] Qianku Hu, Dandan Sun, Qinghua Wu, Haiyan Wang, Libo Wang, Baozhong Liu, Aiguo Zhou, and Julong He. Mxene: a new family of promising hydrogen storage medium. *The Journal of Physical Chemistry A*, 117(51):14253–14260, 2013.

[53] Angel Morales-Garcia, Federico Calle-Vallejo, and Francesc Illas. Mxenes: new horizons in catalysis. *ACS Catalysis*, 10(22):13487–13503, 2020.

[54] Hyunho Kim, Babak Anasori, Yury Gogotsi, and Husam N Alshareef. Thermoelectric properties of two-dimensional molybdenum-based mxenes. *Chemistry of Materials*, 29(15):6472–6479, 2017.

[55] Tahta Amrillah, Angga Hermawan, Yeremia Budi Cristian, Agustina Oktafiani, Diva Meisya Maulina, Darminto Darminto, Jenh Yih Juang, et al. Potential of mxenes as a novel material for spintronics device: A review. *Physical Chemistry Chemical Physics*, 2023.

[56] Hariprasad Vadakke Neelamana, Sreelakshmi Madhavanunni Rekha, and Sarpangala Venkataprasad Bhat. Ti3c2t x mxene: A new promising 2d material for optoelectronics. *Chemistry of Materials*, 2023.

[57] Neng Li, Jiahe Peng, Wee-Jun Ong, Tingting Ma, Peng Zhang, Jizhou Jiang, Xiaofang Yuan, Chuanfang John Zhang, et al. Mxenes: an emerging platform for wearable electronics and looking beyond. *Matter*, 4(2):377–407, 2021.

[58] Songtao Ling, Cheng Zhang, Chunlan Ma, Yang Li, and Qichun Zhang. Emerging mxene-based memristors for in-memory, neuromorphic computing, and logic operation. *Advanced Functional Materials*, 33(1):2208320, 2023.

[59] Meikang Han, Christopher Eugene Shuck, Roman Rakhmanov, David Parchment, Babak Anasori, Chong Min Koo, Gary Friedman, and Yury Gogotsi. Beyond ti3c2t x: Mxenes for electromagnetic interference shielding. *ACS nano*, 14(4):5008–5016, 2020.

[60] Xiaoxia Han, Ju Huang, Han Lin, Zhigang Wang, Pan Li, and Yu Chen. 2d ultrathin mxene-based drug-delivery nanoplatform for synergistic photothermal ablation and chemotherapy of cancer. *Advanced healthcare materials*, 7(9):1701394, 2018.

[61] Babak Anasori and Yury Gogotsi. Introduction to 2d transition metal carbides and nitrides (mxenes). *2D Metal Carbides and Nitrides (MXenes) Structure, Properties and Applications*, pages 3–12, 2019.

[62] Yue Zhang and Zexing Cao. Tuning the activity of molybdenum carbide mxenes for co2 electroreduction by embedding the single transition-metal atom. *The Journal of Physical Chemistry C*, 125(24):13331–13342, 2021.

[63] Hyunho Kim, Zhenwei Wang, and Husam N Alshareef. Mxetronics: Electronic and photonic applications of mxenes. *Nano Energy*, 60:179–197, 2019.

[64] Michael Naguib, Joseph Halim, Jun Lu, Kevin M Cook, Lars Hultman, Yury Gogotsi, and Michel W Barsoum. New two-dimensional niobium and vanadium carbides as promising materials for li-ion batteries. *Journal of the American Chemical Society*, 135(43):15966–15969, 2013.

[65] Olha Mashtalir, Michael Naguib, Vadym N Mochalin, Yohan Dall'Agnese, Min Heon, Michel W Barsoum, and Yury Gogotsi. Intercalation and delamination of layered carbides and carbonitrides. *Nature communications*, 4(1):1716, 2013.

[66] Xiao Tang, Xin Guo, Wenjian Wu, and Guoxiu Wang. 2d metal carbides and nitrides (mxenes) as high-performance electrode materials for lithium-based batteries. *Advanced Energy Materials*, 8(33):1801897, 2018.

[67] Min Xu, Shulai Lei, Jing Qi, Qingyun Dou, Lingyang Liu, Yulan Lu, Qing Huang, Siqi Shi, and Xingbin Yan. Opening magnesium storage capability of two-dimensional mxene by intercalation of cationic surfactant. *Acs Nano*, 12(4):3733–3740, 2018.

[68] Yu Xie, Yohan Dall'Agnese, Michael Naguib, Yury Gogotsi, Michel W Barsoum, Houlong L Zhuang, and Paul RC Kent. Prediction and characterization of mxene nanosheet anodes for non-lithium-ion batteries. *ACS nano*, 8(9):9606–9615, 2014.

[69] Chang E Ren, Meng-Qiang Zhao, Taron Makaryan, Joseph Halim, Muhammad Boota, Sankalp Kota, Babak Anasori, Michel W Barsoum, and Yury Gogotsi. Porous two-dimensional transition metal carbide (mxene) flakes for high-performance li-ion storage. *ChemElectroChem*, 3(5):689–693, 2016.

[70] Xianhong Wu, Zhiyu Wang, Mengzhou Yu, Luyang Xiu, and Jieshan Qiu. Stabilizing the mxenes by carbon nanoplating for developing hierarchical nanohybrids with efficient lithium storage and hydrogen evolution capability. *Advanced Materials*, 29(24):1607017, 2017.

[71] Mian Li, Xinliang Li, Guifang Qin, Kan Luo, Jun Lu, Youbing Li, Guojin Liang, Zhaodong Huang, Jie Zhou, Lars Hultman, et al. Halogenated ti3c2 mxenes with electrochemically active terminals for high-performance zinc ion batteries. *ACS nano*, 15(1):1077–1085, 2021.

[72] Maria R Lukatskaya, Olha Mashtalir, Chang E Ren, Yohan Dall'Agnese, Patrick Rozier, Pierre Louis Taberna, Michael Naguib, Patrice Simon, Michel W Barsoum, and Yury Gogotsi. Cation intercalation and high volumetric capacitance of two-dimensional titanium carbide. *Science*, 341(6153):1502–1505, 2013.

[73] Jeremy Come, Jennifer M Black, Maria R Lukatskaya, Michael Naguib, Majid Beidaghi, Adam J Rondinone, Sergei V Kalinin, David J Wesolowski, Yury Gogotsi, and Nina Balke. Controlling the actuation properties of mxene paper electrodes upon cation intercalation. *Nano Energy*, 17:27–35, 2015.

[74] Mikhael D Levi, Maria R Lukatskaya, Sergey Sigalov, Majid Beidaghi, Netanel Shpigel, Leonid Daikhin, Doron Aurbach, Michel W Barsoum, and Yury Gogotsi. Solving the capacitive paradox of 2d mxene using electrochemical quartz-crystal admittance and in situ electronic conductance measurements. *Advanced Energy Materials*, 5(1):1400815, 2015.

[75] Zheng Ling, Chang E Ren, Meng-Qiang Zhao, Jian Yang, James M Giammarco, Jieshan Qiu, Michel W Barsoum, and Yury Gogotsi. Flexible and conductive mxene films and nanocomposites with high capacitance. *Proceedings of the National Academy of Sciences*, 111(47):16676–16681, 2014.

[76] Muhammad Boota, Mariacecilia Pasini, Francesco Galeotti, William Porzio, Meng-Qiang Zhao, Joseph Halim, and Yury Gogotsi. Interaction of polar and nonpolar polyfluorenes with layers of two-dimensional titanium carbide (mxene): intercalation and pseudocapacitance. *Chemistry of Materials*, 29(7):2731–2738, 2017.

[77] Maria R Lukatskaya, Sankalp Kota, Zifeng Lin, Meng-Qiang Zhao, Netanel Shpigel, Mikhael D Levi, Joseph Halim, Pierre-Louis Taberna, Michel W Barsoum, Patrice Simon, et al. Ultra-high-rate pseudocapacitive energy storage in two-dimensional transition metal carbides. *Nature Energy*, 2(8):1–6, 2017.

[78] Qingmin Shan, Xinpeng Mu, Mohamed Alhabeb, Christopher E Shuck, Di Pang, Xin Zhao, Xue-Feng Chu, Yingjin Wei, Fei Du, Gang Chen, et al. Two-dimensional vanadium carbide (v2c) mxene as electrode for supercapacitors with aqueous electrolytes. *Electrochemistry Communications*, 96:103–107, 2018.

[79] Quanzheng Tao, Martin Dahlqvist, Jun Lu, Sankalp Kota, Rahele Meshkian, Joseph Halim, Justinas Palisaitis, Lars Hultman, Michel W Barsoum, Per OÅ Persson, et al. Two-dimensional mo1. 33c mxene with divacancy ordering prepared from parent 3d laminate with in-plane chemical ordering. *Nature communications*, 8(1):14949, 2017.

[80] Zhimin Fan, Youshan Wang, Zhimin Xie, Duola Wang, Yin Yuan, Hongjun Kang, Benlong Su, Zhongjun Cheng, and Yuyan Liu. Modified mxene/holey graphene films for advanced supercapacitor electrodes with superior energy storage. *Advanced Science*, 5(10):1800750, 2018.

[81] Yi Tang, JianFeng Zhu, ChenHui Yang, and Fen Wang. Enhanced supercapacitive performance of manganese oxides doped two-dimensional titanium carbide nanocomposite in alkaline electrolyte. *Journal of Alloys and Compounds*, 685:194–201, 2016.

[82] Hao Wang, Jianmin Li, Xiaoxiao Kuai, Liangmin Bu, Lijun Gao, Xu Xiao, and Yury Gogotsi. Enhanced rate capability of ion-accessible ti3c2tx-nbn hybrid electrodes. *Advanced Energy Materials*, 10(35):2001411, 2020.

[83] Yangyang Wen, Thomas E Rufford, Xingzhu Chen, Neng Li, Miaoqiang Lyu, Liming Dai, and Lianzhou Wang. Nitrogen-doped ti3c2tx mxene electrodes for high-performance supercapacitors. *Nano energy*, 38:368–376, 2017.

[84] Likui Wang, Meikang Han, Christopher E Shuck, Xuehang Wang, and Yury Gogotsi. Adjustable electrochemical properties of solid-solution mxenes. *Nano Energy*, 88:106308, 2021.

[85] Walter Kohn and Lu Jeu Sham. Self-consistent equations including exchange and correlation effects. *Physical review*, 140(4A):A1133, 1965.

[86] Kendra Letchworth-Weaver and TA Arias. Joint density functional theory of the electrode-electrolyte interface: Application to fixed electrode potentials, interfacial capacitances, and potentials of zero charge. *Physical Review B*, 86(7):075140, 2012.

[87] Lijing Wang, Jin Wang, Zhenzhou Zhang, Linxia Wang, Weihua Wang, Jieyu Liu, Zhanglian Hong, Kyeongjae Cho, and Weichao Wang. Origin of theoretical pseudocapacitance of two-dimensional supercapacitor electrodes ti 3 c 2 t 2 (t= bare, o, s). *Journal of Materials Chemistry A*, 7(27):16231–16238, 2019.

[88] Cheng Zhan, Michael Naguib, Maria Lukatskaya, Paul RC Kent, Yury Gogotsi, and De-en Jiang. Understanding the mxene pseudocapacitance. *The journal of physical chemistry letters*, 9(6):1223–1228, 2018.

[89] Mandira Das and Subhradip Ghosh. Theoretical investigation of capacitances in functionalised mxene supercapacitors m n+ 1c n o2, m= ti, v, nb, mo. *Journal of Physics D: Applied Physics*, 55(8):085502, 2021.

[90] Chengjie Lu, Li Yang, Bingzhen Yan, Liangbo Sun, Peigen Zhang, Wei Zhang, and Zheng-Ming Sun. Nitrogen-doped ti3c2 mxene: mechanism investigation and electrochemical analysis. *Advanced Functional Materials*, 30(47):2000852, 2020.

[91] Mandira Das and Subhradip Ghosh. Computational studies on the electrochemical performance of doped and substituted ti3c2tx (t= o, oh) mxene. *Journal of The Electrochemical Society*, 169(9):090525, 2022.

[92] Berna Akgenc. Intriguing of two-dimensional janus surface-functionalized mxenes: An ab initio calculation. *Computational Materials Science*, 171:109231, 2020.

[93] Mengjie Chen, Lulu Li, Zhiming Deng, Peng Min, Zhong-Zhen Yu, Chuanfang John Zhang, and Hao-Bin Zhang. Two-dimensional janus mxene inks for versatile functional coatings on arbitrary substrates. *ACS Applied Materials & Interfaces*, 15(3):4591–4600, 2023.

[94] Yinggan Zhang, Baisheng Sa, Naihua Miao, Jian Zhou, and Zhimei Sun. Computational mining of janus sc 2 c-based mxenes for spintronic, photocatalytic, and solar cell applications. *Journal of Materials Chemistry A*, 9(17):10882–10892, 2021.

[95] Edirisuriya M Dilanga Siriwardane and Jianjun Hu. First-principles investigation of ti2cso and ti2csse janus mxene structures for li and mg electrodes. *The Journal of Physical Chemistry C*, 125(23):12469–12477, 2021.

[96] Bhuvaneswari Soundiraraju and Benny Kattikkanal George. Two-dimensional titanium nitride (ti2n) mxene: synthesis, characterization, and potential application as surface-enhanced raman scattering substrate. *ACS nano*, 11(9):8892–8900, 2017.

[97] M Born and R Oppenheimer. Zur quantentheorie der molekeln annalen der physik, v. 84. 1927.

[98] D. R. Hartree. The wave mechanics of an atom with a non-coulomb central field. part i. theory and methods. *Mathematical Proceedings of the Cambridge Philosophical Society*, 24(1):89–110, 1928.

[99] Vladimir Fock. Näherungsmethode zur lösung des quantenmechanischen mehrkörperproblems. *Zeitschrift für Physik*, 61:126–148, 1930.

[100] P. Hohenberg and W. Kohn. Inhomogeneous electron gas. *Phys. Rev.*, 136:B864–B871, Nov 1964.

[101] W. Kohn and L. J. Sham. Self-consistent equations including exchange and correlation effects. *Phys. Rev.*, 140:A1133–A1138, Nov 1965.

[102] Matt Probert. Electronic structure: Basic theory and practical methods, by richard m. martin: Scope: graduate level textbook. level: theoretical materials scientists/condensed matter physicists/computational chemists, 2011.

[103] John P Perdew. Unified theory of exchange and correlation beyond the local density approximation. *Electronic structure of solids' 91*, 11, 1991.

[104] John P. Perdew and Wang Yue. Accurate and simple density functional for the electronic exchange energy: Generalized gradient approximation. *Phys. Rev. B*, 33:8800–8802, Jun 1986.

[105] John P. Perdew, Kieron Burke, and Matthias Ernzerhof. Generalized gradient approximation made simple. *Phys. Rev. Lett.*, 77:3865–3868, Oct 1996.

[106] P.J. Hasnip and C.J. Pickard. Electronic energy minimisation with ultrasoft pseudopotentials. *Computer Physics Communications*, 174(1):24–29, 2006.

[107] P. E. Blöchl. Projector augmented-wave method. *Phys. Rev. B*, 50:17953–17979, Dec 1994.

[108] G. Kresse and D. Joubert. From ultrasoft pseudopotentials to the projector augmented-wave method. *Phys. Rev. B*, 59:1758–1775, Jan 1999.

[109] Ravishankar Sundararaman, Kathleen A Schwarz, Kendra Letchworth-Weaver, and TA Arias. Spicing up continuum solvation models with salsa: The spherically averaged liquid susceptibility ansatz. *The Journal of Chemical Physics*, 142(5), 2015.

[110] Ravishankar Sundararaman and William A Goddard. The charge-asymmetric nonlocally determined local-electric (candle) solvation model. *The Journal of chemical physics*, 142(6), 2015.

[111] Michael Naguib, Murat Kurtoglu, Volker Presser, Jun Lu, Junjie Niu, Min Heon, Lars Hultman, Yury Gogotsi, and Michel W. Barsoum. Two-dimensional nanocrystals produced by exfoliation of ti3alc2. *Advanced Materials*, 23(37):4248–4253, 2011.

[112] Mohammad Khazaei, Masao Arai, Taizo Sasaki, Chan-Yeup Chung, Natarajan S. Venkataramanan, Mehdi Estili, Yoshio Sakka, and Yoshiyuki Kawazoe. Novel electronic and magnetic properties of two-dimensional transition metal carbides and nitrides. *Advanced Functional Materials*, 23(17):2185–2192, 2013.

[113] Wenqiang Zhang, Chuan Cheng, Peilin Fang, Bin Tang, Jindou Zhang, Guoming Huang, Xin Cong, Bao Zhang, Xiao Ji, and Ling Miao. The role of terminations and coordination atoms on the pseudocapacitance of titanium carbonitride monolayers. *Phys. Chem. Chem. Phys.*, 18:4376–4384, 2016.

[114] Joongoo Kang, Su-Huai Wei, Kai Zhu, and Yong-Hyun Kim. First-principles theory of electrochemical capacitance of nanostructured materials: Dipole-assisted subsurface intercalation of lithium in pseudocapacitive tio2 anatase nanosheets. *The Journal of Physical Chemistry C*, 115(11):4909–4915, 2011.

[115] Lijing Wang, Jin Wang, Zhenzhou Zhang, Linxia Wang, Weihua Wang, Jieyu Liu, Zhanglian Hong, Kyeongjae Cho, and Weichao Wang. Origin of theoretical pseudocapacitance of two-dimensional supercapacitor electrodes ti3c2t2 (t = bare, o, s). *J. Mater. Chem. A*, 7:16231–16238, 2019.

[116] Cheng Zhan, Michael Naguib, Maria Lukatskaya, Paul R. C. Kent, Yury Gogotsi, and De-en Jiang. Understanding the mxene pseudocapacitance. *The Journal of Physical Chemistry Letters*, 9(6):1223–1228, 2018. PMID: 29461062.

[117] Ruben-Simon Kuhnel, David Reber, and Corsin Battaglia. *Journal of the Electrochemical Society*, 167:070544, 2020.

[118] Mohammad Khazei, Masao Arai, Taizo Sasaki, Ahmad Ranjbar, Yunye Liang, and Seiji Yunoki. *Physical Review B*, 92:075411, 2015.

[119] T C Leung, C L Kao, W S Su, Y J Feng, and C T Chan. *Physical Review B*, 68:195408, 2003.

[120] R B Rakhi, B Ahmed, M N Hedhili, D H Anjum, and H N Alshareef. *Chemistry of Materials*, 27:5314, 2015.

[121] Yunfeng Guan, Song Jiang, Ye Cong, Jiapei Wang, Zhijun Dong, Qin Zhang, Guanming Yuan, Yanjun Li, and Xuanke Li. *2D Materials*, 7:025010, 2020.

[122] K Gopalkrishna, A Govindaraj, and C N R Rao. *Journal of Materials Chemistry A*, 1:7563, 2013.

[123] J Zhang, W Z Ma, Z Y Feng, F F Wu, D H Wei, B J Xi, and S L Xiong. *Journal of Energy Chemistry*, 39:54, 2019.

[124] Y Lei, K Fujisawa, F Zhang, N Briggs, A R Aref, Y T Yeh, Z Lin, J A Robinson, R Rajagopalan, and M Terrones. *ACS Applied Engineering Materials*, 2:8625, 2019.

[125] H M Jeong, J W Lee, W H Shin, Y J Choi, H J Shin, J K Kang, and J W Choi. *Nano Letters*, 11:2472, 2011.

[126] B Jiang, C Tian, L Wang, L Sun, C Chen, X Nong, Y Qiao, and H Fu. *Applied Surface Science*, 258:3438, 2012.

[127] L Sun, L Wang, C Tian, T Tan, Y Xie, K Shi, M Li, and H Fu. *RSC Advances*, 2:4498, 2012.

[128] M Kaur, M Kaur, and V K Sharma. *Advances in Colloid and Interface Science*, 259:44, 2018.

[129] Y Wen, T E Rufford, X Chen, N Li, M Lyu, L Dai, and L Wang. *Nano Energy*, 38:368, 2017.

[130] L Chengjie, L Yang, B Yan, L Sun, P Zhang, W Zhang, and Z Sun. *Advanced Functional Materials*, 30:2000852, 2020.

[131] W Zhang, C Cheng, P Fang, B Tang, J Zhang, G Huang, X Cong, B Zhang, X Ji, and L Miao. *Physical Chemistry Chemical Physics*, 18:4376, 2016.

[132] M R Lukatskaya, O Mashtalir, C E Ren, Y Dall'Agnese, P Rozier, P L Taberna, M Naguib, P Simon, M W Barsoum, and Y Gogotsoi. *Science*, 341:1502, 2013.

[133] H Shao, K Xu, Y C Wu, A Ladecola, L Liu, H Ma, L Qu, E Raymundo-Pinero, J Zhu, Z Lin, P L Taberna, and P Simon. *ACS Energy Letters*, 5:2873, 2020.

[134] Thomas B Sobyra, Tyler S Mathis, Yuri Gogotsoi, and Paul Fenter. Probing the in situ pseudocapacitative charge storage in ti3c2 mxene thin films with x-ray reflectivity. *Applied Materials and Interfaces*, 13:43597–43605, 2021.

[135] M Naguib, R R Unocic, B L Armstrong, and J Nanda. *Dalton Transactions*, 6:1322, 2012.

[136] P A Maughan, L Bouscarrat, V R Seymour, S Shao, S J Haigh, R Dawson, N Tapia-Ruiz, and N Bimbo. *Nanoscale Materials*, 3:3145, 2021.

[137] Ravishankar Sundararaman, Kendra Letchworth-Weaver, Kathleen A Schwarz, Deniz Gunceler, Yalcin Ozhabes, and TA Arias. Jdftx: Software for joint density-functional theory. *SoftwareX*, 6:278–284, 2017.

[138] JP Perdew, K Burke, and M Ernzerhof. Generalized gradient approximation made simple. 1996, 77, 3865-3868, erratum. *Phys. Rev. Lett*, 78:1396, 1996.

[139] Kevin F Garrity, Joseph W Bennett, Karin M Rabe, and David Vanderbilt. Pseudopotentials for high-throughput dft calculations. *Computational Materials Science*, 81:446–452, 2014.

[140] R F W Bader. *Atoms in Molecules - A Quantum Theory, Oxford University Press, New York*, 1990.

[141] Chan Wook Jang, Won Jun Lee, Jae Kuk Kim, Sang Minh Park, Sung Kim, and Suk-Ho Choi. Growth of two-dimensional janus mosse by a single in situ process without initial or follow-up treatments. *NPG Asia Materials*, 14(1):15, 2022.

[142] Sumner B Harris, Yu-Chuan Lin, Alexander A Puretzky, Liangbo Liang, Ondrej Dyck, Tom Berlijn, Gyula Eres, Christopher M Rouleau, Kai Xiao, and David B Geohegan. Real-time diagnostics of 2d crystal transformations by pulsed laser deposition: Controlled synthesis of janus wsse monolayers and alloys. *ACS nano*, 17(3):2472–2486, 2023.

[143] Ting Zheng, Yu-Chuan Lin, Yiling Yu, Pavel Valencia-Acuna, Alexander A Puretzky, Riccardo Torsi, Chenze Liu, Ilia N Ivanov, Gerd Duscher, David B Geohegan, et al. Excitonic dynamics in janus mosse and wsse monolayers. *Nano letters*, 21(2):931–937, 2021.

[144] Liang Dong, Jun Lou, and Vivek B Shenoy. Large in-plane and vertical piezoelectricity in janus transition metal dichalchogenides. *ACS nano*, 11(8):8242–8248, 2017.

[145] Haifang Cai, Yufeng Guo, Huajian Gao, and Wanlin Guo. Tribo-piezoelectricity in janus transition metal dichalcogenide bilayers: A first-principles study. *Nano Energy*, 56:33–39, 2019.

[146] Qun-Fang Yao, Jia Cai, Wen-Yi Tong, Shi-Jing Gong, Ji-Qing Wang, Xiangang Wan, Chun-Gang Duan, and JH Chu. Manipulation of the large rashba spin splitting in polar two-dimensional transition-metal dichalcogenides. *Physical review B*, 95(16):165401, 2017.

[147] Tao Hu, Fanhao Jia, Guodong Zhao, Jiongyao Wu, Alessandro Stroppa, and Wei Ren. Intrinsic and anisotropic rashba spin splitting in janus transition-metal dichalcogenide monolayers. *Physical Review B*, 97(23):235404, 2018.

[148] Jiajia Chen, Kai Wu, Huanhuan Ma, Wei Hu, and Jinlong Yang. Tunable rashba spin splitting in janus transition-metal dichalcogenide monolayers via charge doping. *RSC advances*, 10(11):6388–6394, 2020.

[149] YC Cheng, ZY Zhu, Muhammad Tahir, and Udo Schwingenschlögl. Spin-orbit–induced spin splittings in polar transition metal dichalcogenide monolayers. *Europhysics Letters*, 102(5):57001, 2013.

[150] Hoachi Wang, Qinyi Chen, Hui Li, Qian Duan, Dayong Jian, and Jianhua Hou. *Chemical Physics Letters*, 735:136777, 2019.

[151] Chanjuan Shang, Hueling Lei, Binpeng Hou, Masheng Wu, Bo Xu, Gang Liu, and Chuying Ouyang. *The Journal of Physical Chemistry C*, 122:23899, 2018.

[152] Fen Xiong and Yue Chen. *Nanotechnology*, 32:025702, 2020.

[153] Wei Jin, Shiyun Wu, and Zhiguo Wang. *Physica E: Low-dimensional Systems and Nanostructures*, 103:307, 2018.

[154] Nathan C Frey, Arkamita Bandyopadhyay, Hemant Kumar, Anasori Babak, Yuri Gogotsi, and Vivek B Shenoy. *ACS Nano*, 13:2831, 2019.

[155] Berna Akgenc. *Computational Materials Science*, 171:109231, 2020.

[156] Zicong Marvin Wong, Tianqi Deng, Wen Shi, Gang Wu, Teck Leong Tan, and Shuo-Wang Yang. High performance photocatalytic and thermoelectric two-dimensional asymmetrically ordered janus-like mxene alloys. *Materials Advances*, 1(5):1176–1185, 2020.

[157] Di Jin, Luke R Johnson, Abhinav S Raman, Xing Ming, Yu Gao, Fei Du, Yingjin Wei, Gang Chen, Aleksandra Vojvodic, Yuri Gogotsi, and Xing Meng. *The Journal of Physical Chemistry C*, 124:10584, 2020.

[158] Jens Jørgen Mortensen, Lars Bruno Hansen, and Karsten Wedel Jacobsen. Real-space grid implementation of the projector augmented wave method. *Physical review B*, 71(3):035109, 2005.

[159] Georg Kresse and Daniel Joubert. From ultrasoft pseudopotentials to the projector augmented-wave method. *Physical review b*, 59(3):1758, 1999.

[160] P E Blochl. *Physical Review B*, 50:17953, 1994.

[161] H J Monkhorst and J D Pack. *Physical Review B*, 13:5188, 1976.

[162] Stefano Baroni, Stefano De Gironcoli, Andrea Dal Corso, and Paolo Giannozzi. Phonons and related crystal properties from density-functional perturbation theory. *Reviews of modern Physics*, 73(2):515, 2001.

[163] Atsushi Togo and Isao Tanaka. First principles phonon calculations in materials science. *Scripta Materialia*, 108:1–5, 2015.

[164] Shuichi Nosé. A unified formulation of the constant temperature molecular dynamics methods. *The Journal of chemical physics*, 81(1):511–519, 1984.

[165] William G Hoover. Canonical dynamics: Equilibrium phase-space distributions. *Physical review A*, 31(3):1695, 1985.

[166] Zhengyang Shen, Zeyi Wang, Min Zhang, Mingxia Gao, Jianjiang Hu, Fang Du, Yongfeng Liu, and Hongge Pan. A novel solid-solution mxene (ti0. 5v0. 5) 3c2 with high catalytic activity for hydrogen storage in mgh2. *Materialia*, 1:114–120, 2018.

[167] Meikang Han, Kathleen Maleski, Christopher Eugene Shuck, Yizhou Yang, James T Glazar, Alexandre C Foucher, Kanit Hantanasirisakul, Asia Sarycheva, Nathan C Frey, Steven J May, et al. Tailoring electronic and optical properties of mxenes through forming solid solutions. *Journal of the American Chemical Society*, 142(45):19110–19118, 2020.

[168] Bevin Huang, Genevieve Clark, Efrén Navarro-Moratalla, Dahlia R Klein, Ran Cheng, Kyle L Seyler, Ding Zhong, Emma Schmidgall, Michael A McGuire, David H Cobden, et al. Layer-dependent ferromagnetism in a van der waals crystal down to the monolayer limit. *Nature*, 546(7657):270–273, 2017.

[169] Chao Wu, Chenhan Liu, Yi Tao, and Yunfei Chen. Effects of magnetic ordering on structural stability and phonon transport in monolayer td-vx2 (x= se, i). *Physics Letters A*, 469:128746, 2023.

[170] Changsheng Song, Xin Liu, Xiaoping Wu, Jingjing Wang, Jiaqi Pan, Tingyu Zhao, Chaorong Li, and Jiqing Wang. Surface-vacancy-induced metallicity and layer-dependent magnetic anisotropy energy in $cr_2ge_2te_6$. *Journal of Applied Physics*, 126(10):105111, 2019.

[171] Zaiyao Fei, Bevin Huang, Paul Malinowski, Wenbo Wang, Tiancheng Song, Joshua Sanchez, Wang Yao, Di Xiao, Xiaoyang Zhu, Andrew F May, et al. Two-dimensional itinerant ferromagnetism in atomically thin fe3gete2. *Nature materials*, 17(9):778–782, 2018.

[172] Chen Si, Jian Zhou, and Zhimei Sun. Half-metallic ferromagnetism and surface functionalization-induced metal–insulator transition in graphene-like two-dimensional cr2c crystals. *ACS applied materials & interfaces*, 7(31):17510–17515, 2015.

[173] Qian Sun, Jie Li, Yi Li, Zongxian Yang, and Ruqian Wu. Cr2nx2 mxene (x= o, f, oh): a 2d ferromagnetic half-metal. *Applied Physics Letters*, 119(6):062404, 2021.

[174] Yunliang Yue, Buwei Wang, Nanxi Miao, Chao Jiang, Hongwei Lu, Bowen Zhang, Yankai Wu, Jie Ren, and Min Wang. Tuning the magnetic properties of zr2n mxene by biaxial strain. *Ceramics International*, 47(2):2367–2373, 2021.

[175] Junjie He, Pengbo Lyu, and Petr Nachtigall. New two-dimensional mn-based mxenes with room-temperature ferromagnetism and half-metallicity. *Journal of Materials Chemistry C*, 4(47):11143–11149, 2016.

[176] Yinggan Zhang, Zhou Cui, Baisheng Sa, Naihua Miao, Jian Zhou, and Zhimei Sun. Computational design of double transition metal mxenes with intrinsic magnetic properties. *Nanoscale Horizons*, 7(3):276–287, 2022.

[177] W Kohn and L J Sham. *Physical Review A*, 140:1133, 1965.

[178] AJ Pindor, J Staunton, GM Stocks, and H Winter. Disordered local moment state of magnetic transition metals: A self-consistent kkr cpa calculation. *Journal of Physics F: Metal Physics*, 13(5):979, 1983.

[179] Julie Staunton, BL Gyorffy, AJ Pindor, GM Stocks, and H Winter. The "disordered local moment" picture of itinerant magnetism at finite temperatures. *Journal of magnetism and magnetic materials*, 45(1):15–22, 1984.

[180] V I Anisimov, J Zaanen, and O K Andersen. *Physical Review B*, 44:943, 1991.

List of Publications

1. **Mandira Das** and Subhradip Ghosh, *Theoretical investigation of capacitances in functionalised MXene supercapacitors $M_{n+1}C_nO_2$, M=Ti, V, Nb, Mo*, J. Phys. D: Appl. Phys. 55 (2022) 08502*
2. **Mandira Das** and Subhradip Ghosh, *Computational Studies of the Electrochemical Performance of Doped and Substituted $Ti_3C_2T_x$*, 2022 J. Electrochem. Soc. 169 090525*
3. **Mandira Das**, Himanshu Murari, Subhradip Ghosh and Biplab Sanyal, *Effects of Chemical and magnetic disorder on the electrochemical properties of $V_{2-x}Mn_xCO_2$ MXene electrodes*, arXiv:2305.17462*
4. **Mandira Das** and Subhradip Ghosh, *Improved charge storage capacity of supercapacitor electrodes by engineering surfaces: the case of Janus MXenes*, arXiv:2310.06334*
5. Md Tarik Hossain, **Mandira Das**, Subhradip Ghosh and P.K. Giri,*Understanding the interfacial charge transfer in the CVD grown $Bi_2O_2Se/CsPbBr_3$ nanocrystal heterostructure and its exploitation in superior photodetection: experiment vs. theory*, Nanoscale, 2021, 13, 14945-14959
6. Sumaiya Parveen, **Mandira Das**, Subhradip Ghosh and P.K. Giri, *Experimental and theoretical study of europium-doped organometal halide perovskite nanoplatelets for UV photodetection with high responsivity and fast response* Nanoscale, 2022, 14, 6402-6416
7. Sumana Paul, Sanju Nandi, **Mandira Das**, Abhilasha Bora, Md Tarik Hossain, Subhradip Ghosh And P.K. Giri,*Two-dimensional bismuth oxyselenide quantum dots as nanosensors for selective metal ion detection over a wide dynamic range: sensing mechanism and selectivity*, Nanoscale, 2023, 15, 12612
8. A book chapter has been accepted for ACS Symposium Series volume titled *"Age of MXenes, Volume 1. Fundamentals and Artificial Intelligence: Machine Learning Interventions"*,Chapter 6, pp 143-168. The authors are **Mandira Das**, Himangshu Sekhar Sarmah, Himanshu Murari, and Subhradip Ghosh.

Conferences attended

- Delivered a talk titled *"Density Functional Theory based investigation of Ti_2C and Nb_2C MXene for Supercapacitor Applications"* at **CTFM-2020: Current Trends in Functional Materials**, in National Institute of Technology Karnataka, Surathkal, Mangalore during January 15-17, 2020.
- Presented a poster titled *"Density Functinal Theory based investigation of MXene for Supercapacitor Applications"* at the **Evolution of Electronic Structure Theory and Experimental Realization (EESTER-2020)** jointly organized by SRM Institute of Science and Technology (INDIA), Indian Institute of Technology Madras (INDIA) and Uppsala University (SWEDEN) during December 14-18, 2020.
- Presented a poster titled *"Computational studies on electrochemical performances of doped and substituted $Ti_3C_2O_2$ MXene"* at **Workshop on Electrochemical Energy Storage: Theory, Experiments, and Applications** organized by ICTP (ITALY) during May 5-26, 2022.

[0]Publications marked with * are included in the thesis

- Delivered a talk titled *"Computational studies on electrochemical performances of doped and substituted $Ti_3C_2O_2$ MXene"* at **DPG Spring Meeeting,2023**, in Technical University, Dresden, Germany during March 26-31, 2023.
- Delivered a talk titled *"Manipulation of electrochemical properties of MXene electrodes for supercapacitor applications by chemical and magnetic disorder"* at **NAMMA, Psi-k, 2023**, in JNCASR and IISC, Bengaluru, India during July 24-28, 2023.